Mid-Infrared Supercontinuum Laser System and its Biomedical Applications

by

Chenan Xia

A dissertation submitted in partial fulfillment
of the requirements for the degree of
Doctor of Philosophy
(Electrical Engineering)
in The University of Michigan
2009

Doctoral Committee:

Professor Mohammed N. Islam, Chair
Professor Almantas Galvanauskas
Professor Fred L. Terry Jr.
Professor Michael J. Welsh

This dissertation is dedicated to my parents—*Xia Yongjiang* and *Xu Buning*.

ACKNOWLEDGEMENTS

First of all, I would like to gratefully and sincerely thank my advisor, Professor Mohammed N. Islam, for lending me the opportunity to pursue my doctoral study at Michigan. Dr. Islam has given me invaluable guidance on my research and spent tremendous amount of his time on a day-to-day basis on my project. His mentorship is paramount in providing me a full set of skills from which I can benefit for a lifetime.

I have to thank Dr. Almantas Galvanauskas, Dr. Fred L. Terry, Jr., and Dr. Michael J. Welsh, for their great insights and support on my work. I want to also thank my fellow students and coworkers, Vinay Alexander, Cheng Ming-Yuan, Michael Freeman, Kevin Ke, Ojas Kulkarni, Malay Kumar, Dong-Joon Lee, Ma Xiuquan, Jeremiah Mauricio, Xu Zhao, and Andy Zakel, for their wholehearted support and fruitful discussion. They are my greatest fortune and I truly enjoyed working with all of these wonderful people and wish everyone the best.

I would like to thank Department of Electrical Engineering and Computer Science and the University of Michigan for the world class facilities and financial support. I must acknowledge Army Research Office (ARO), BAE systems, the Defense Advanced Research Projects Agency (DARPA), Naval Air Command (NAVAIR), Omni Sciences Inc, STARS Foundation, and Vyalex Inc for funding my research project.

Last, but most importantly, I have to thank my family for their continual support of

my time in graduate school. My parents, Xia Yongjiang and Xu Buning, always have faith in me and unconditionally stood behind me. My uncle, Xia Weijiang, taught me to have ambition and courage since I was a kid. Also, I would like to thank my fiancée, Yang Bei, with whom I have had the best time in my life. I would not be where I am today without them.

TABLE OF CONTENTS

Chapter

LIST OF FIGURES

Figure

LIST OF TABLES

Table

ABSTRACT

A mid-infrared supercontinuum (SC) laser system is developed, which provides a continuous spectrum from ~0.8 to ~4.5 μm and is pumped by amplified nanosecond laser diode pulses. The SC laser uses ZBLAN (ZrF_4-BaF_2-LaF_3-AlF_3-NaF) fluoride fibers. The SC light source is all-fiber-integrated with no moving parts, operates at room temperature, and eliminates the need of mode-locked lasers. The time-averaged power of the SC is scalable up to 10.5 W by amplifying the pump pulses using cladding-pumped erbium/ytterbium co-doped fiber power amplifiers. SC has also been generated in silica fibers with spectrum extending to ~3 μm and an average power up to 5.3 W. The SC laser system comprises an all-fiber-spliced high power pump laser system followed by nonlinear optical generation fibers, i.e. ZBLAN and silica fibers. The SC generation is initiated by breaking up the nanosecond diode pulses into femtosecond pulses through modulation instability, and the spectrum is then broadened through the interplay of self-phase modulation, parametric four-wave mixing, and stimulated Raman scattering. Theoretical simulations have been carried out to study the SC generation mechanism by numerically solving the generalized nonlinear Schrödinger equation. The SC long wavelength edge is limited by the intrinsic fiber material absorption, i.e. ~3 μm in silica fibers and ~4.5 μm in ZBLAN fibers, respectively. Mid-infrared absorption spectroscopy of the constituents of normal artery, e.g. endothelial cells and smooth muscle cells, and atherosclerotic plaques, e.g. adipose tissue, macrophages and foam cells, and selective ablation of lipid-rich tissues have also been demonstrated using the SC laser system.

Chapter I

Introduction

1. Background of SC generation

Broadband light sources are widely used in almost every corner of the world. Electric incandescent lamps have been illuminating our houses since Thomas Edison lit his carbon filament light bulb in 1879. Blackbody radiators, which emit a continuous spectrum in the infrared wavelength window, also have applications in a wide array of areas. With the advent of lasers in 1960, a new generation of light source was introduced with many unprecedented characteristics. By comparison, lasers generate electromagnetic radiation with high brightness and intensity, can be focused into extremely small size or collimated over kilometers of distances, and typically emit light in a narrow bandwidth. So, is there a lighting device that can cover a continuous and broad spectrum while at the same time still retains the qualities of the laser?

Lasers based on supercontinuum (SC) generation could be the answer. The SC generation process, in which the output spectrum of a narrow bandwidth laser undergoes a substantial spectral broadening through the interplay of different nonlinear optical interactions, has been widely reported and studied since it was observed in 1969 [1-11]. Early SC experiments were primarily conducted in liquid and solid materials with limited spectral bandwidth and power [1]. In the past decade, broadband SC generation in optical fibers has been of particular interest because of the optical fibers' unique advantages in their long

optical interaction length, tight optical confinement and potential applications in optical telecommunication [12,13].

In optical fibers, two approaches of generating continuum are generally used - pumping a short length of highly non-linear fiber with femtosecond or picosecond pulses [14] or using continuous-wave (CW)/quasi-CW sources to pump long lengths (>100m) of fiber [15]. The broadening mechanism in the former can be attributed primarily to self phase modulation (SPM), while in the latter, spectral broadening is achieved due to the combined effect of parametric four-wave mixing (FWM) and stimulated Raman scattering (SRS) [16-18]. For example, a mode-locked femtosecond erbium fiber laser was used to generate 400 mW of SC output from 0.8-2.7 μm in just 12 cm of highly nonlinear (HiNL) fiber [14]. In contrast, Abeeluck et al demonstrated a continuum extending beyond 1.75 μm with ~5 W average power in 500 m of HiNL fiber pumped by a CW Raman fiber laser [15]. SC generation from ~0.8 to 1.7 μm in a dispersion-shifted fiber has also been demonstrated by using amplified laser diode (LD) pulses with 30 ps pulse width [19].

Recently, photonic crystal fibers, which utilize the unique physical properties of the photonic crystals and possess new degrees of freedom in fiber geometry, have been widely studied to generate SC extending to the visible wavelength regime [20-38]. For example, a soft-glass (Schott SF6) photonics crystal fiber (PCF) has been used to generate and extend the SC spectrum down to ~350 nm in the deep blue regime [39]. The time-averaged power of the SC generated in the photonics crystal fiber has also been increased to 50 W [40].

However, there are still several areas where major improvements can be made on the road towards developing a more powerful SC light source. First of all, mode-locked lasers with very short pulses and high peak powers are most commonly used to generate the SC

since the magnitude of optical nonlinear effects, e.g. SPM and SRS, strongly depends on the peak power of the pump pulses. However, mode-lock lasers are inflexible for scaling up the average power, expensive, and complicated. They also require routine maintenance for optimal operation, and the generated SC spectrum usually has large pulse-to-pulse spectral power fluctuations.

Secondly, the SC long wavelength edge generated in the fused silica fibers is limited to ~3 μm due to the strong material absorption. It will open windows for applications if the SC long wavelength edge can be extended to the mid-infrared (mid-IR) wavelength regime [41-44], i.e. 2-5 μm, which conventionally can only be accessed through optical parametric oscillators (OPO) [45], quantum cascaded lasers [46], and free electron lasers [47]. To generate SC extending beyond ~3 μm, optical fibers fabricated by infrared glass material systems need to be used.

As illustrated in Fig. 1.1, we can observe that ZBLAN (ZrF_4-BaF_2-LaF_3-AlF_3-NaF) fluoride fibers have an optical transmission window in 1-5 μm wavelength regime [48], which can serve as a potential candidate for mid-IR SC generation. In particular, a recent report of SC generation in ZBLAN fibers used a femtosecond laser to generate 1.8-3.4 μm continuum with 5 mW average power [43]. Several other infrared fibers, e.g. chalcogenide and tellurite fibers, also exhibit low material absorption in the mid-IR. For example, SC generation ranging from 2-3 μm has been demonstrated in sulfide and selenide fibers by a 2.5 μm OPA pump laser [41]. On the other hand, mode-locked femtosecond lasers have been used to generate SC spectrum beyond 3 μm in tellurite fibers [44] with modest average power (<0.1 W).

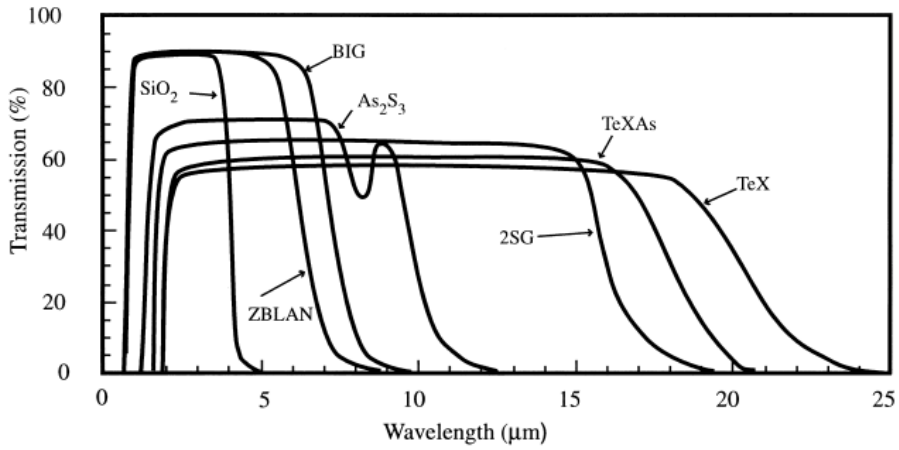

Fig. 1.1 Optical transmission of various infrared glasses compared to silica. The two glasses ZBLAN and BIG are multi-component fluoride glasses based on ZrF_4 and BaF_2 for the first one and BaF_2, InF_3, GaF_3 for the second. The glass 2SG is a selenium based material containing the elements: Se, Sb, Ge and Ga. The TeX glass is based on the combination of Te, Se and I_2 while the TeXAs is a similar glass with the addition of As. This figure and its description are excerpted from Ref [48].

Last, but not least, another challenge remains to be addressed before a SC source can be effectively and pragmatically used in a number of applications. High power fiber-based pump lasers usually comprise free space, bulk optical components. An all-fiber-integrated SC laser source with no moving parts will be extremely beneficial in terms of its robustness, compactness and operational convenience. On the other hand, the output spectrum of SC laser usually contains amplitude fluctuations in the range of ~0.1-10%. To implement a SC light source in optical absorption spectroscopy or chemical sensing applications, the signal fluctuations of the light source need to be dynamically compensated and reduced.

Overall, we can summarize the challenges in the existing SC laser systems and foresee some opportunities as illustrated in Fig. 1.2, which include:

1. Extending the SC spectrum into the mid-IR wavelength regime;
2. Increasing the time-averaged output power for remote or high power applications; and
3. Demonstrating meaningful applications by using the SC laser.

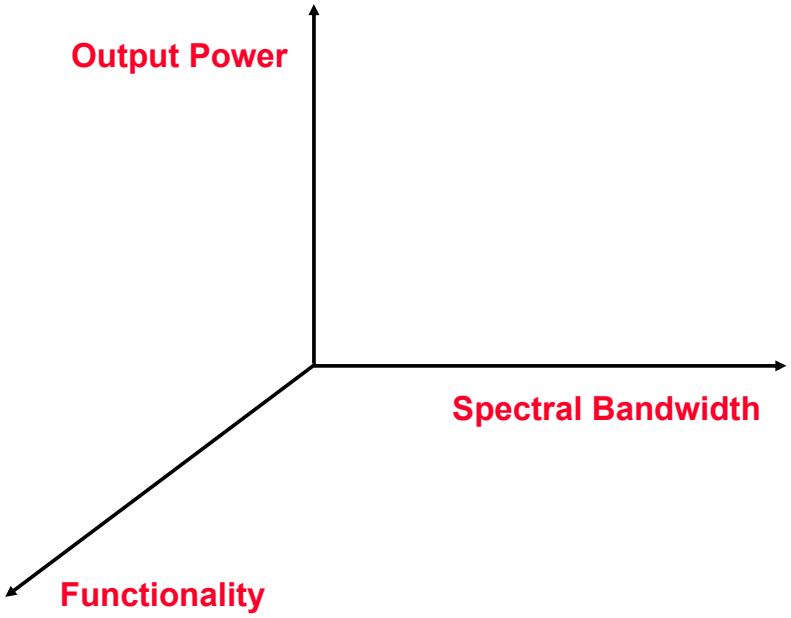

Fig. 1.2 Challenges and opportunities for SC laser.

2. Applications of SC laser sources

SC light sources have a wide variety of applications in numerous fields, including infrared countermeasures [46], remote chemical sensing [49], optical coherence tomography [50], real-time optical metrology [51], and optical tissue ablation [52]. In particular, our SC light source, due to the unique properties of mid-IR wavelength radiation, will find applications in many fields. Several reasons for the importance of mid-IR include:

1. Emulating black body radiation for hot metal objects that radiate under the influence of atmospheric transmission/absorption in the mid-IR;
2. Chemical sensing since many chemicals have their vibrational or rotational absorptions in the mid-IR;
3. High resolution cross section tomography imaging;
4. Low-cost high speed date communication network that uses only few nanometers of spectrum; and

5. Optical tissue ablation.

***Black body radiation emulation*:** Every object emits electromagnetic radiation, which can be determined by the object's temperature [53]. At room temperature, the emitted electromagnetic waves consist of mostly infrared light (Fig. 1.3). Traditionally, OPOs are used to provide near- and mid-IR light with sufficient power level. However, OPOs employ bulky, free space optics, which is expensive, hard to achieve single spatial mode operation and requires regular maintenance. In comparison, our SC light source is cost-effective as it uses commercially available off-the-shelf parts, maintenance-free due to the removal of bulk optical components, and portable and light-weight because of the all-fiber-integration design. In addition, because SC light is generated in a single mode optical fiber, the output can be easily collimated and transmitted over a very long distance. Hence, our SC light source can adequately substitute as a black body radiator for the conventional OPO.

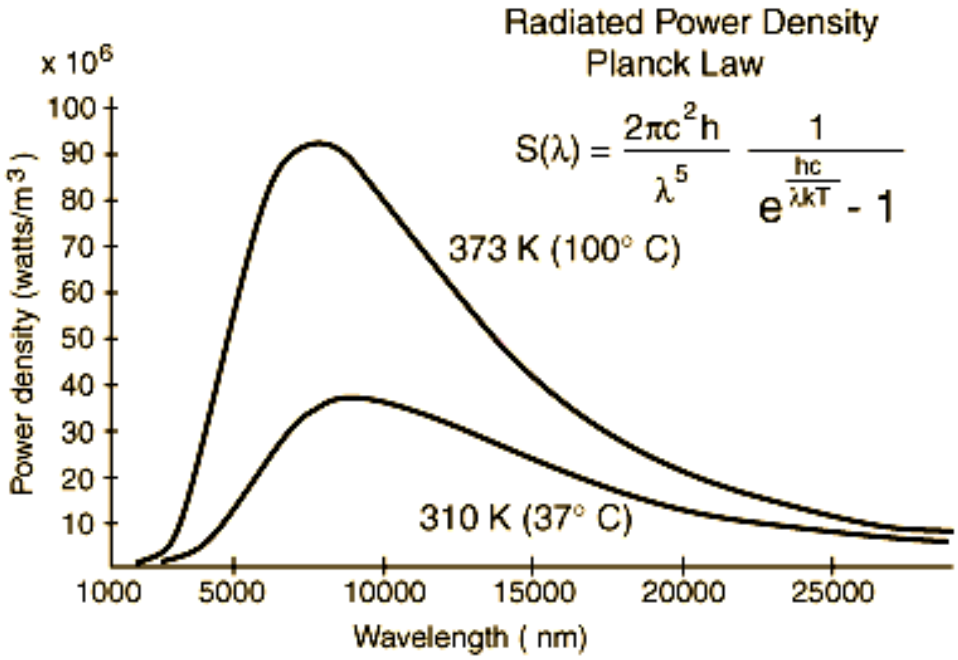

Fig. 1.3 Black body radiation curve at room temperature. This figure and its description are excerpted from Ref [53].

***Chemical sensing*:** SC light sources can provide chemical sensing via spectral fingerprinting. In essence, what the system does is to blanket a given area with a broad spectrum of light and then record those wavelengths of light that do not return to the base unit. Since chemicals have a distinct spectral signature, this approach can be used to compare unknown samples against known agents, providing the means to quickly and easily detect substances of interest. The key advantages offered by our SC laser for this application are high brightness and collimated light beam, both of which are necessary for deploying systems with long stand-off distances. Certain applications of interest include airborne partial sensing, explosives detection, and biological sample absorption spectroscopy.

Near- and Mid-IR optical window, i.e. 1-5 μm, is the host of vibrational absorption lines and bands of a wide variety of chemical species. For example, Fig. 1.4 illustrates the absorption lines of some typical chemicals in the 1-7 μm wavelength regime [54]. From this, we can draw several interesting conclusions. First of all, the absorption coefficient of a given chemical species in the mid-IR is much stronger, which can be sometimes as high as 100-1000x as manifested by the CO_2 absorption lines, compared to its near-IR counterpart. This is because almost all molecular species have their fundamental vibrational absorption lines lying in the mid-IR wavelength regime, whereas the corresponding overtone lines fall in the near-IR window.

Secondly, most chemicals have more than one distinctive absorption line in the near- and mid-IR optical window. Such absorption properties offer a unique opportunity for chemical sensing by using a broadband SC light source to identify not only a single absorption line, but the absorption "pattern". Both selectivity and sensitivity of the measurement can be drastically improved. Finally, water (H_2O) absorption is present in a wide portion of the near-

and mid-IR window. For applications that involve biological targets, special considerations may need to be made to filter out the impact of water absorption.

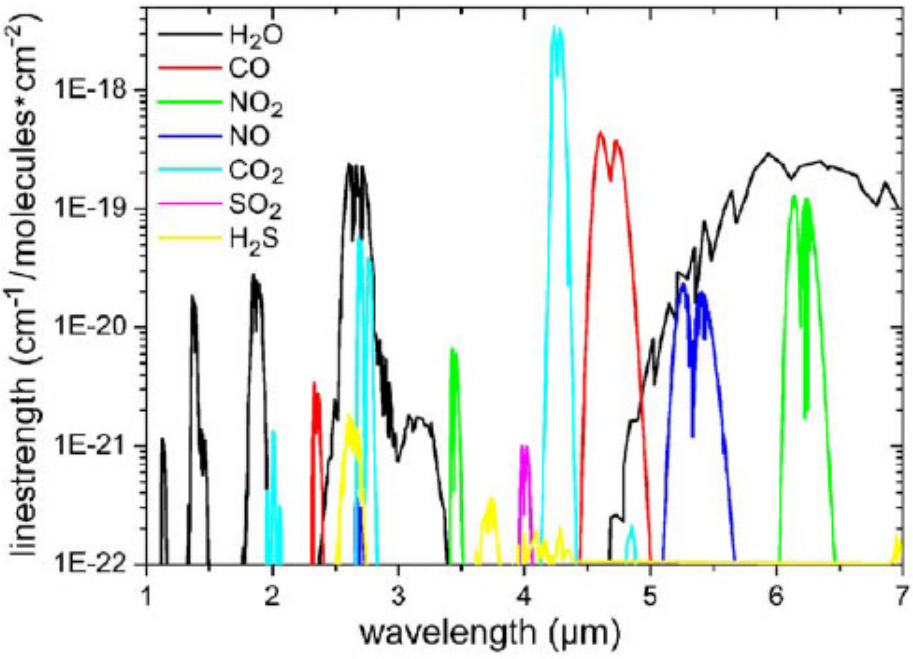

Fig. 1.4 Envelopes of absorption bands between 1 and 7 μm as calculated from the Hitran 2004 database. This figure and its description are excerpted from Ref [54].

***Optical coherence tomography*:** OCT is a novel technology that can provide high resolution cross section tomography images of internal tissues in a biological sample [55]. The optical cross-sectional imaging capability of OCT is enabled by the temporal coherence character of the light source coupled with interferometer measurement. So, broadband light sources are desirable because they give rise to short temporal coherence length and determine the minimum resolvable distance in the samples.

Figure 1.5 illustrates the emission spectra of various broadband light sources utilized for the ultrahigh resolution OCT [55]. Almost entire visible and near-infrared region has been covered. In the visible area, a femtosecond mode-locked solid state laser is usually employed to provide high peak power optical pulses. Nonlinear effects such as SPM, FWM and SRS in

optical fibers are triggered to broaden the spectral bandwidth of the laser pulse and generate broad SC spectrum. In the near-IR window, silica fiber-based SC laser are typically used as the light source for OCT measurement. Micron and sub-micron level axial resolutions have been demonstrated with light source emitting in both visible and near-IR optical windows.

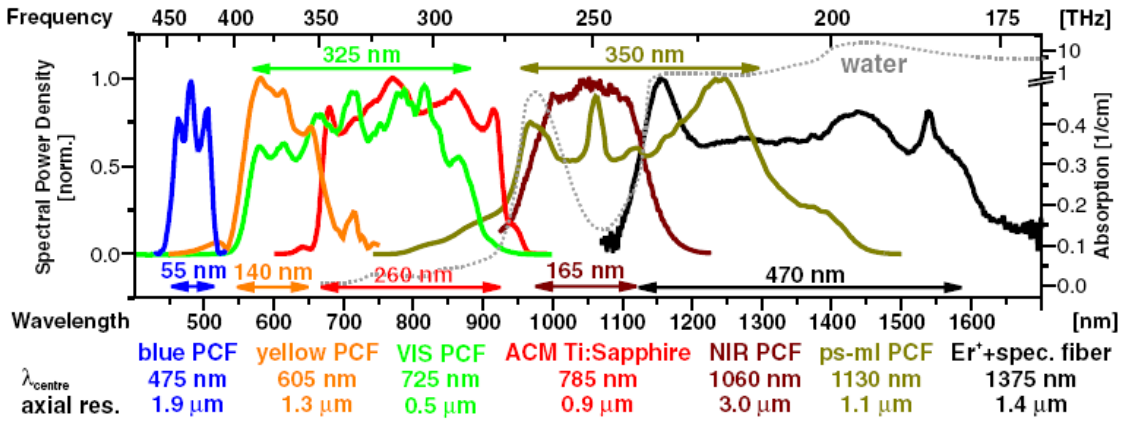

Fig. 1.5 Spectra of various light sources used in OCT system. This figure and its description are excerpted from Ref [55].

***High speed data communication network*:** Conventionally, one dedicated LD is used to provide one data channel (downstream or upstream data transmission) in the optical communication network. This means that to provide full data downloading capability for a large number of users, multiple LDs must be installed into the infrastructure of the telecommunication service provider. What a SC laser allows is to slice optical wavelengths into small spectral components (e.g., like slicing a pie into small pieces) [12,13]. Each of these sliced pieces can be used as a seed source or data channel for optical telecommunications. As illustrated in Fig. 1.6, instead of using one hundred individual LDs to serve one hundred users, we can use one SC light source and slice it into one hundred channels to provide the same service. The cost per channel will be dramatically reduced. Furthermore, by using a SC laser source to cater the communication needs of different users,

advanced network security features, such as channel scrambling, can also readily realized without adding extra physical devices in the system.

There are generally two approaches to encode data onto each SC spectrum slice/channel. Narrow band optical filters can be used to select a particular portion of the SC spectrum and the filtered out light can then be encoded by an optical modulator. To further lower the per channel system cost, one high speed modulator can also encode different spectral parts of the SC spectrum, i.e. different signal channels, in the time-division multiplexing mode, which maps different spectral units/channels into a series of consecutive time slots.

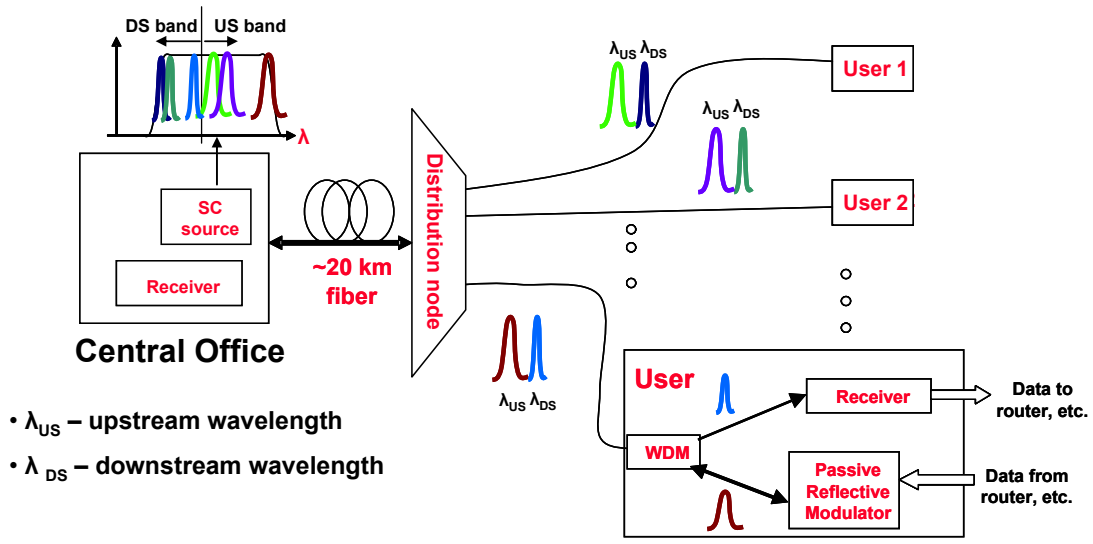

Fig. 1.6 SC based multiple-user optical communication network infrastructure.

***Optical tissue ablation*:** Many biological targets have their fundamental vibrational absorption bands and lines in the mid-IR wavelength regime [56]. More specifically, proteins show primary light absorption at 2.8-3.2 μm due to N-H and O-H bonds, while lipids exhibit absorptions in 3.2-3.6 μm associated with C-H stretching vibrations (Fig. 1.7). So, a SC laser with sufficient average power can heat up the biological samples by targeting the light in the

corresponding C-H, O-H, or N-H bands. While watts of laser power in near-IR (~1-2 μm) can sometimes only heat fatty samples above physiological temperature [52], only tens of milliwatts of laser power are required to ablate tissue in the 3.2-3.6 μm regime. In addition, SC lasers have a unique advantage in ablating biological tissues because different portion of the spectrum can be selected and utilized to work on different samples of interest.

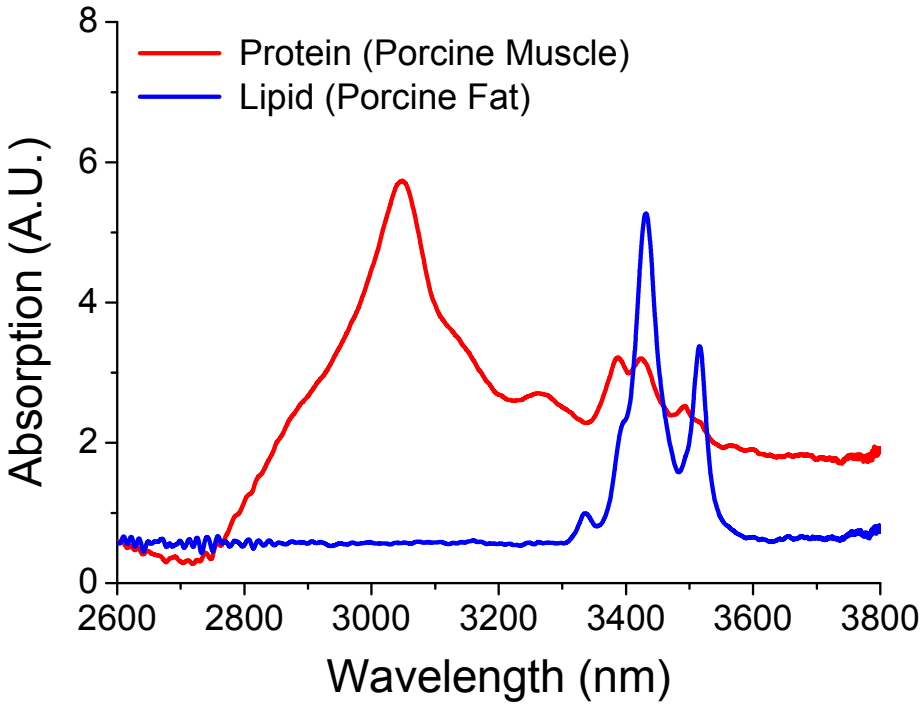

Fig. 1.7 Mid-IR absorption spectra of (a) porcine muscle, and (b) porcine fat.

3. My doctoral research work

In our research group led by Prof. Mohammed Islam, we started working on mid-IR SC generation in optical fibers from an accidental discovery. During the early work on cascaded Raman wavelength shifting, Dr. Mike Freeman and Dr. Amos Kuditcher observed drastic spectral broadening in silica fibers when the input pump light lies in the anomalous dispersion regime of the optical fiber. One hypothesis was that the modulation instability (MI) process in the fiber initiates and facilitates the broadband SC generation. This discovery

opened the possibility of producing SC lasers using commercial, off-the-shelf telecommunication technology. The results are a low cost, compact and robust SC light source with easily scalable average power. Our group has since been focused on optimizing this technology and applying it into a variety of applications.

In my doctoral research, I am focused on answering all of the previously analyzed challenges through developing a novel and uniquely designed mid-IR SC laser system. The SC system consists of two parts—the laser pump system and mid-IR SC generation fibers (Fig. 1.8). First, for the laser pump system, a high power, all-fiber-spliced system is designed and demonstrated with more than >20 W average power and >10 kW peak power output capability.

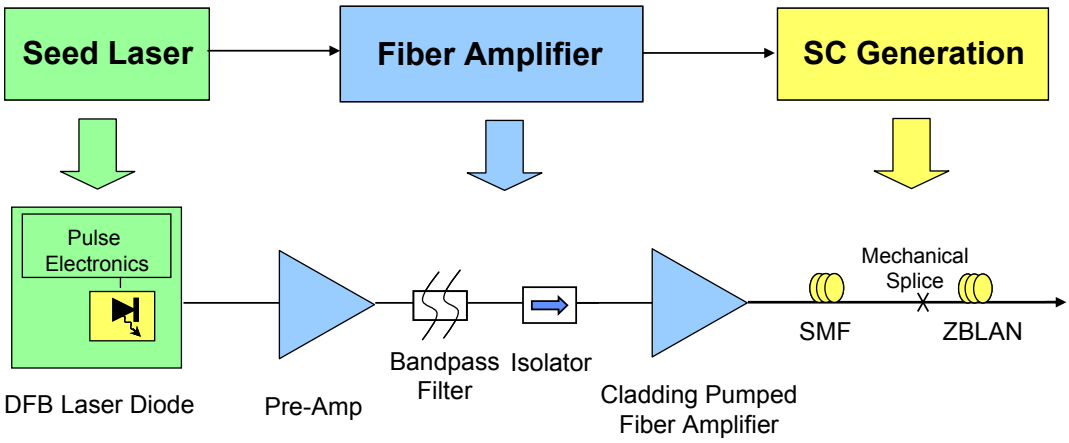

Fig. 1.8 Mid-IR SC laser system comprised of (a) laser pump system—seed laser followed by fiber amplifier, and (b) mid-IR SC generation fibers.

To eliminate the need of mode-lock lasers for SC generation, a semiconductor LD used in conjunction with high peak/average power laser amplifier system is an ideal candidate. By leveraging the mature telecommunication technology, LDs are cost-effective, compact, and have some unique advantages. LD can generate nanosecond and sub-nanosecond optical pulses by directly modulating the diode driving current. In a LD-based laser system, the

output pulse pattern, e.g. pulse repetition rate, pulse width, can be conveniently modified under different operational condition by changing the electrical driving current level. In contrast, mode-lock lasers typically have a fixed repetition rate, output power, and need external modulation.

In addition, a LD based laser system can generate fairly high peak power by amplifying the LD pulses in fiber amplifier systems. Thanks to recent advances in the development of high power fiber amplifiers, over 10 kW of peak power and over 10 W of time-averaged power can be achieved in a single strand of optical fibers. Nevertheless, it should be noted that, the performance of LD based fiber laser systems, such as peak power and pulse duration, is still not as superior as that of mode-locked lasers. More sophisticated design of the SC system and better utilization of the nonlinear processes in the optical fibers are required to generate an ultra-broadband SC spectrum.

We break up the nanosecond LD pulses into a train of ultra-short sub-picosecond pulses by using the physics of the fiber, i.e. MI. The MI process in the fiber significantly reduces the pulse duration and increases the pulse peak power. Broadband SC is then generated in the concatenated nonlinear fibers through these sub-picosecond, high peak power pulses.

Secondly, SC generation extending into the mid-IR with record spectral bandwidth and output power has been achieved and demonstrated. By choosing ZBLAN fluoride fibers with a optical transmission window in the mid-IR, SC is generated with the long wavelength edge extending to ~4.5 μm for the first time to our knowledge. Compared to other infrared fibers, ZBLAN fibers have more mature fabrication technology, which ensures high power operation and long-term reliability. Moreover, the material zero dispersion wavelength of ZBLAN glass is located at ~1.6 to 1.7 μm, which is closer to the conveniently accessible 1.5

μm telecommunication window.

Last, but not least, our SC laser, seeded by commercially available telecommunication LD, is all-fiber-integrated with no moving parts or bulk optical components, operates under room temperature, and is power scalable by varying the pulse repetition rate. The entire SC spectrum is emitted from the ZBLAN fiber simultaneously in the single spatial mode. Also, the time-averaged power of the SC has also been scaled up to 10.5 W, the highest SC power reported to date in mid-IR fibers.

More specifically, each following chapter of this dissertation is dedicated to address one particular challenge or present one major improvement we have achieved in developing the mid-IR SC light source.

In chapter II, I describe mid-IR SC generation in ZBLAN fluoride fibers pumped by amplified nanosecond LD pulses. As pointed out earlier, the SC long wavelength edge is limited to ~ 3 μm in fused silica fibers. We choose ZBLAN fluoride fibers to extend the SC generation into the mid-IR with a continuous spectrum from ~0.8 μm to beyond 4.5 μm, which is consistent with the intrinsic ZBLAN material absorption. The SC has an average power of ~23 mW, a pump-to-SC power conversion efficiency exceeding 50%, and a spectral power density of ~-20 dBm/nm over a large fraction of the spectrum.

It is worth noting that the geometric design of the optical fiber plays a critical role in the SC generation. Aside from material absorption loss, the light propagating in the optical fiber also experiences optical attenuation due to the fiber bend-induced loss, which is related to the wave-guiding capability of the fiber. In certain scenario, although the optical transmission window of the fiber material can be much wider, only certain portion of the spectrum can be confined or guided in the optical fiber. The bend-induced loss then becomes the limiting

factor of the SC generation. As a rule-of-thumb, the light that can propagate in the step-index fiber without suffering noticeable loss is up to ~1.5x the cut-off wavelength of the fiber. Hence, we choose to use a ZBLAN fiber with a cut-off wavelength at 2.75 μm to minimize the bend-induced loss and are able to push the SC long wavelength edge to the material absorption limit.

In chapter III, I demonstrate high power SC generation in ZBLAN fluoride fibers achieved by free space cladding-pumped erbium/ytterbium co-doped fiber amplifiers. Mid-IR SC extending to ~4.0 μm is generated with 1.3 W average power, the highest power to our knowledge at the time reported, in ZBLAN fluoride fibers. ZBLAN fibers with similar geometric design and length as described in chapter II are used in the experiments. It should be noted, to date, our mid-IR SC laser still provides the highest output power among all reported results.

To increase the time-averaged power of the SC, high power amplifier systems need to be used. Because we choose a LD-based fiber amplifier platform as the pump system for SC generation, we can relatively easily increase the output average power by upgrading the last stage power amplifier. Specifically, a free-space, multi-stage, cladding-pumped erbium/ytterbium fiber amplifier system is employed to amplify the LD pulses to a time-averaged power of ~7 W (peak power of ~12 kW). The high power SC experiments described in this chapter serve as a proof-of-concept for high power mid-IR SC generation and also illustrate the flexibility of our SC generation platform.

The scalability of the SC average power is also demonstrated by varying the pump pulse repetition rate while maintaining the similar peak power. The nanosecond LD pumping also simplifies the scaling up of the time-averaged power. Because SC generation is a nonlinear

optical process, which is affected by the peak power of the pump pulses, the spectral shape of the SC remains unchanged as long as the peak power of every pump pulse stays the same.

In chapter IV, I report SC generation in fused silica fibers and conduct a comprehensive theoretical study of the SC generation mechanism. SC with a continuous spectrum from ~0.8-3 μm is generated in a standard single mode fiber followed by high non-linearity (HiNL) fiber. The time-averaged power in the continuum is also scaled from 27 mW to 5.3 W by increasing the pulse repetition rate from 5 kHz to 1 MHz, while maintaining comparable peak power.

SC generation in optical fibers is a complex nonlinear optical process involving the interactions of SPM, FWM and SRS. To facilitate these nonlinear processes, high peak power and short optical pulses are preferred. For example, a state-of-the-art 1.5 μm mode-lock laser can provide optical pulses as short as ~10-100 fs with a peak power >50 kW. Our LD-based pump system, however, can only generate nanosecond-width optical pulse with a peak power in the range of ~10-20 kW.

To compensate the deficits of our pump system, we generate the SC generation in a two step process that separates pulse break-up and soliton formation from spectral broadening (Fig. 1.8). In the first stage, LD pulses are launched into a standard single mode fiber, where the interaction between nonlinearity and anomalous dispersion breaks the quasi-CW input into a train of solitons through MI [18], and significantly increases the peak power. The generated solitons will then undergo frequency down shift through soliton self frequency shifting (SSFS) [16]. In the second stage HiNL fiber, the SC spectrum is further broadened primarily through the SPM effect of the ultra-short solitons [1,16,17]. We attribute the generated SC spectrum to the ensemble average of multiple solitons and the superposition of

their corresponding spectra.

In chapter V, I demonstrate a high power all-fiber-integrated SC laser system that generates SC in ZBLAN fiber with 10.5 W time-averaged power. The SC laser system developed in this chapter combines all the novelties that are realized separately in our previous work. Most notably are the following features.

1. All-fiber-integrated configuration that has no moving parts. In particular, the SC pump system is all-fiber-spliced with its output coupled into a single mode silica fiber. The only non-fixed joint point in the SC system is the mechanical splice between silica and ZBLAN fibers.
2. Mid-IR SC generation extending beyond 4 μm with a time-averaged power scalable up to ~10.5 W, which is the highest power for mid-IR SC fiber laser reported to date. Near diffraction-limited beam qualities are maintained over the entire SC spectrum.
3. Linearly scalability of the SC average power by varying the input pump power and pulse repetition rate. We further investigate the theoretical limitations on the achievable average power handling and spectral width for the SC generation in ZBLAN fibers.

In chapter VI, I demonstrate two applications using our SC laser. The SC laser has been successfully implemented in biomedical applications for both mid-IR *in vitro* absorption spectroscopy and laser selective ablation. We measure mid-IR absorption spectra of biological samples, including the constituents of the normal artery and atherosclerotic vulnerable plaque in the 2.6-3.8 μm optical window. In addition, selective optical ablation of the lipid-rich tissues, e.g. adipose tissues, without damaging normal artery tissues has also

been demonstrated by targeting the laser light in the 3.2-3.6 μm C-H fatty acid and cholesterol esters absorption band.

To use the SC laser in practical applications, several issues need to be addressed. First, special measures are required to reduce the amplitude fluctuations of the SC spectrum, and therefore improve the accuracy of the spectroscopic measurements. We design and implement a dual-channel measurement technique to improve the signal-to-noise ratio of the SC system. Secondly, the long-term stability of the SC system plays a vital role. Real applications may often take hours or even days to finish. By using efficient thermal management and highly reliable mechanical stage design, our SC can operate without further manual tweaking for a much extended period of time. Finally, we propose a fiber-based catheter design to exploit the diagnostic and therapeutic potentials of our SC laser based spectroscopy and selective ablation system in the clinical environment.

This dissertation is organized as follows. In chapter II, I describe the SC in ZBLAN fluoride fibers pumped by amplified nanosecond LD pulses. In chapter III, I demonstrate the high power SC generation in ZBLAN fluoride fibers achieved by free space cladding-pumped erbium/ytterbium co-doped fiber amplifiers. In chapter IV, SC generation in fused silica fibers is reported. I, in chapter V, demonstrate a high power all-fiber-integrated SC laser system to generate SC in ZBLAN fiber with 10.5 W time-averaged power. I show the spectroscopy and selective ablation applications of the SC laser in chapter VI. Finally, I summarize my work and offer my thoughts on the future work in chapter VII.

References:

[1] R. R. Alfano, *The supercontinuum laser source: fundamentals with updated references*, 2nd ed. (Springer, New York, 2006).

[2] O. Fedatova, A. Husakou and J. Herrmann, "Supercontinuum generation in planar rib waveguides enabled by anomalous dispersion," Opt. Express **14**, 1512-1517 (2006).

[3] A. Mussot, T. Sylvestre, L. Provino, and H. Maillotte, "Generation of a broadband single-mode supercontinuum in a conventional dispersion-shifted fiber by use of a subnanosecond microchip laser," Opt. Lett. **28**, 1820-1822 (2003).

[4] J. H. Lee, Y. Takushima, and K. Kikuchi, "Continuous-wave supercontinuum laser based on an erbium-doped fiber ring cavity incorporating a highly nonlinear optical fiber," Opt. Lett. **30**, 2599-2601 (2005).

[5] A. Saliminia, S. L. Chin, and R. Vallée, "Ultra-broad and coherent white light generation in silica glass by focused femtosecond pulses at 1.5 μm," Opt. Express **13**, 5731-5738 (2005).

[6] Y. Takushima, "High average power, depolarized super-continuum generation using a 1.55-μm ASE noise source," Opt. Express **13**, 5871-5877 (2005).

[7] J. N. Kutz, C. Lyngå, and B. J. Eggleton, "Enhanced supercontinuum generation through disperion-management," Opt. Express **13**, 3989-3998 (2005).

[8] P. S. Westbrook, J. W. Nicholson, K. S. Feder, and A. D. Yablon, "Improved supercontinuum generation through UV processing of highly nonlinear fibers," J. Lightwave Tech. **23**, 13-18 (2005).

[9] A. Demircan and U. Bandelow, "Supercontinuum generation by the modulation instability," Opt. Comm. **244**, 181-185 (2005).

[10] G. A. Nowak, J. Kim, and M. N. Islam, "Stable supercontinuum generation in short lengths of conventional dispersion-shifted fiber," Appl. Opt. **38**, 7364-7369 (1999).

[11] M. N. Islam, G. Sucha, I. Bar-Joseph, M. Wegener, J. P. Gordon, and D. S. Chemla, "Broad bandwidths from frequency-shifting solitons in fibers," Opt. Lett. **14**, 370-372 (1989).

[12] T. Morioka, K. Mori, S. Kawanishi, and M. Saruwatari, "Multi-WDM-channel, GBit/s pulse generation from a single laser source utilizing LD-pumped supercontinuum in optical fibers," IEEE Photon. Technol. Lett. **6**, 365-368 (1994).

[13] H. Takara, "Multiple optical carrier generation from a supercontinuum source," Opt. Photon. News **13**, No. 3 48-51 (2002).

[14] J. W. Nicholson, A. D. Yablon, P. S. Westbrook, K. S. Feder, and M. F. Yan, "High power, single mode, all-fiber source of femtosecond pulses at 1550 nm and its use in supercontinuum generation," Opt. Express **12**, 3025-3034 (2004).

[15] A. K. Abeeluck and C. Headley, "Continuous-wave pumping in the anomalous- and normal-dispersion regimes of nonlinear fibers for supercontinuum generation," Opt. Lett. **30**, 61-63 (2005).

[16] T. Hori, N. Nishizawa, T. Goto, and M. Yoshida, "Experimental and numerical analysis of widely broadened supercontinuum generation in highly nonlinear dispersion-shifted fiber with a femtosecond pulse ," J. Opt. Soc. Am. B **21**, 1969-1980 (2004).

[17] S. Kobtsev and S. Smirnov, "Modelling of high-power supercontinuum generation in highly nonlinear, dispersion shifted fibers at CW pump," Opt. Express **13**, 6912-6918 (2005).

[18] G. P. Agrawal, *Nonlinear Fiber Optics,* 3rd edition, (Academic, San Diego, 2001).
[19] S. Moon and D. Y. Kim, "Generation of octave-spanning supercontinuum with 1550-nm amplified diode-laser pulses and a dispersion-shifted fiber," Opt. Express **14**, 270-278 (2006).
[20] J. M. Dudley, G. Genty, and S. Coen, "Supercontinuum generation in photonic crystal fiber," Rev. Mod. Phys. **78**, 1135-1184 (2006).
[21] J. K. Ranka, R. S. Windeler, and A. J. Stentz, "Visible continuum generation in air-silica microstructure optical fibers with anomalous dispersion at 800 nm," Opt. Lett. **25**, 25-27 (2000).
[22] J. C. Travers, S. V. Popov, and J. R. Taylor, "Extended blue supercontinuum generation in cascaded holey fibers," Opt. Lett. **30**, 3132-3134 (2005).
[23] T. Schreiber, T. V. Andersen, D. Schimpf, J. Limpert, and A. Tünnermann, "Supercontinuum generation by femtosecond single and dual wavelength pumping in photonic crystal fibers with two zero dispersion wavelengths," Opt. Express **13**, 9556-9569 (2005).
[24] G. Genty, T. Ritari, and H. Ludvigsen, "Supercontinuum generation in large mode-area microstructured fibers," Opt. Express **13**, 8625-8633 (2005).
[25] P. Falk, M. H. Frosz, and O. Bang, "Supercontinuum generation in a photonic crystal fiber with two zero-dispersion wavelengths tapered to normal dispersion at all wavelengths," Opt. Express **13**, 7535-7540 (2005).
[26] V. Tombelaine, C. Lesvigne, P. Leproux, L. Grossard, V. Couderc, J-L. Auguste, J-M. Blondy, G. Huss, and P-H. Pioger, "Ultra wide band supercontinuum generation in air-silica holey fibers by SHG-induced modulation instabilities," Opt. Express **13**, 7399-7404 (2005).
[27] J. C. Travers, R. E. Kennedy, S. V. Popov, J. R. Taylor, H. Sabert, and B. Mangan, "Extended continuous-wave supercontinuum generation in low-water-loss holey fibers," Opt. Lett. **30**, 1938-1940 (2005).
[28] P-A. Champert, V. Couderc, P. Leproux, S. Février, V. Tombelaine, L. Labonté, P. Roy, C. Froehly, and P. Nérin, "White-light supercontinuum generation in normally dispersive optical fiber using original multi-wavelength pumping system," Opt. Express **12**, 4366-4371 (2004).
[29] G. Genty, M. Lehtonen, H. Ludvigsen, and M. Kaivola, "Enhanced bandwidth of supercontinuum generated in microstructured fibers," Opt. Express **12**, 3471-3480 (2004).
[30] S. G. Leon-Saval, T. A. Birks, W. J. Wadsworth, P. St. J. Russell, and M. W. Mason, "Supercontinuum generation in submicron fibre waveguides," Opt. Express **12**, 2864-2869 (2004).
[31] K. M. Hilligsøe, T. V. Andersen, H. N. Paulsen, C. K. Nielsen, K. Mølmer, S. Keiding, R. Kristiansen, K. P. Hansen, and J. J. Larsen, "Supercontinuum generation in a photonic crystal fiber with two zero dispersion wavelengths," Opt. Express **12**, 1045-1054 (2004).
[32] W. J. Wadsworth, N. Joly, J. C. Knight, T. A. Birks, F. Biancalana, and P. St. J. Russell, "Supercontinuum and four-wave mixing with Q-switched pulses in endlessly single-mode photonic crystal fibres," Opt. Express **12**, 299-309 (2004).
[33] V. V. R. K. Kumar, A. K. George, W. H. Reeves, J. C. Knight, P. St. J. Russell, F. G. Omenetto, and A. J. Taylor, "Extruded soft glass photonic crystal fiber for ultrabroad supercontinuum generation," Opt. Express **10**, 1520-1525 (2002).

[34] A. V. Husakou and J. Herrmann, "Supercontinuum generation, four-wave mixing, and fission of higher-order solitons in photonic-crystal fibers," J. Opt. Soc. Am. B **19**, 2171-2182 (2002).
[35] S. Coen, A. H. L. Chau, R. Leonhardt, J. D. Harvey, J. C. Knight, W. J. Wadsworth, and P. S. J. Russell, "Supercontinuum generation by stimulated Raman scattering and parametric four-wave mixing in photonic crystal fibers," J. Opt. Soc. Am. B **19**, 753-764 (2002).
[36] J. M. Dudley, L. Provino, N. Grossard, H. Maillotte, R. S. Windeler, B. J. Eggleton, and S. Coen, "Supercontinuum generation in air–silica microstructured fibers with nanosecond and femtosecond pulse pumping," J. Opt. Soc. Am. B **19**, 765-771 (2002).
[37] W. J. Wadsworth, A. Ortigosa-Blanch, J. C. Knight, T. A. Birks, T. -. M. Man, and P. S. J. Russell, "Supercontinuum generation in photonic crystal fibers and optical fiber tapers: a novel light source," J. Opt. Soc. Am. B **19**, 2148-2155 (2002).
[38] A. V. Avdokhin, S. V. Popov, and J. R. Taylor, "Continuous-wave, high-power, Raman continuum generation in holey fiber," Opt. Lett. **28**, 1353-1355 (2003).
[39] F. G. Omenetto, N. A. Wolchover, M. R. Wehner, M. Ross, A. Efimov, A. J. Taylor, V. V. R .K. Kumar, A. K. George, J .C. Knight, N. Y. Joly, and P. St. J. Russell, "Spectrally smooth supercontinuum from 350 nm to 3 μm in sub-centimeter lengths of soft-glass photonic crystal fibers," Opt. Express **14**, 4928-4934 (2006).
[40] J. C. Travers, A. B. Rulkov, B. A. Cumberland, S. V. Popov, and J. R. Taylor, "Visible supercontinuum generation in photonic crystal fibers with a 400W continuous wave fiber laser," Opt. Express **16**, 14435-14447 (2008).
[41] J. S. Sanghera, L. B. Shaw, C. M. Florea, P. Pureza, V. Q. Nguyen, D. Gibson, F. Kung, and I. D. Aggarwal, "Non-linearity in chalcogenide glasses and fibers, and their applications," presented at Quantum Electronics and Laser Science Conference QELS 2008, San Jose, Calif., May 4-9, 2008, QTuL5.
[42] J. M. Parker, "Fluoride glasses," Annu. Rev. Mater. Sci. **19**, 21-41 (1989).
[43] C. L. Hagen, J. W. Walewski, and S. T. Sanders, "Generation of a continuum extending to the midinfrared by pumping ZBLAN fiber with an ultrafast 1550-nm source," IEEE Photon. Technol. Lett. **18**, 91-93 (2006).
[44] P. Domachuk, N. A. Wolchover, M. Cronin-Golomb, A. Wang, A. K. George, C. M. B. Cordeiro, J. C. Knight, and F. G. Omenetto, "Over 4000 nm bandwidth of mid-IR supercontinuum generation in sub-centimeter segments of highly nonlinear tellurite PCFs," Opt. Express **16**, 7161-7168 (2008).
[45] I. T. Sorokina and K. L. Vodopyanov, eds., *Solid-State Mid-Infrared Laser Sources*, (Springer-Verlag, Berlin Heidelberg, 2003).
[46] M. Razeghi, S. Slivken, Y. Bai, and S. R. Darvish, "The quantum cascade laser: a versatile and powerful tool," Opt. Photon. News **19**, No. 7 42-47 (2008).
[47] G. S. Edwards, R. H. Austin, F. E. Carroll, M. L. Copeland, M. E. Couprie, W. E. Gabella, R. F. Haglund, B. A. Hooper, M. S. Hutson, E. D. Jansen, K. M. Joos, D. P. Kiehart, I. Lindau, J. Miao, H. S. Pratisto, J. H. Shen, Y. Tokutake, A. F. G. van der Meer, and A. Xie, "Free-electron-laser-based biophysical and biomedical instrumentation," Rev. Sci. Instrum. **74**, 3207-3245 (2003).
[48] J. Lucas, "Infrared glasses," Curr. Opin. Solid State Mater. Sci. **4**, 181-187 (1999).
[49] J. Mandon, E. Sorokin, I. T. Sorokina, G. Guelachvili, and N. Picqué, "Supercontinua for high-resolution absorption multiplex infrared spectroscopy," Opt. Lett. **33**, 285-287 (2008).

[50] H. Lim, Y. Jiang, Y. Wang, Y. Huang, Z. Chen, and F. Wise, "Ultrahigh-resolution optical coherence tomography with a fiber laser source at 1 μm," Opt. Lett. **30**, 1171-1173 (2005).
[51] S. A. Diddams, D. J. Jones, J. Ye, S. T. Cundiff, J. L. Hall, J. K. Ranka, R. S. Windeler, R. Holzwarth, T. Udem, and T.W. Hänsch, "Direct link between microwave and optical frequencies with a 300 THz femtosecond laser comb," Phys. Rev. Lett. **84**, 5102–5104 (2000).
[52] R. R. Anderson, W. Farinelli, H. Laubach, D. Manstein, A. N. Yaroslavsky, J. Gubeli, K. Jordan, G. R. Neil, M. Shinn, W. Chandler, G. P. Williams, S. V. Benson, D. R. Douglas, H. F. Dylla, "Selective photothermolysis of lipid-rich tissues: A free electron laser study," Lasers Surg. Med. **38**, 913-919 (2006).
[53] "Blackbody radiation," http://hyperphysics.phy-astr.gsu.edu/Hbase/bbrc.html.
[54] U. Willer, M. Saraji, A. Khorsandi, P. Geiser, and W. Schade, "Near- and mid-infrared laser monitoring of industrial processes, environment and security applications," Opt. Lasers Eng. **44**, 699-710 (2006).
[55] A. Unterhuber, B. Povazay, K. Bizheva, B. Hermann, H. Sattmann, A. Stingl, T. Le, M. Seefeld, R. Menzel, M. Preusser, H. Budka, Ch. Schubert, H. Reitsamer, P. K. Ahnelt, J. E. Morgan, A. Cowey, and W. Drexler, "Advances in broad bandwidth light sources for ultrahigh resolution optical coherence tomography," Phys. Med. Biol. **49**, 1235-1246 (2004).
[56] C. Paluszkiewicz, W. M. Kwiatek, A. Banas, A. Kisiel, A. Marcelli, and A. Piccinini, "SR-FTIR spectroscopic preliminary findings of non-cancerous, cancerous, and hyperplastic human prostate tissues," Vib. Spectrosc. **43**, 237-242 (2007).

Chapter II

Supercontinuum Generation in ZBLAN Fluoride Fibers by Erbium-Doped Fiber Amplifiers

1. Introduction

We generate, for the first time to our knowledge, the broadest supercontinuum extending from ~0.8 μm (near-IR) to beyond 4.5 μm (mid-IR) in ZBLAN (ZrF_4-BaF_2-LaF_3-AlF_3-NaF…) fluoride fibers. Nanosecond laser diode pulses are amplified by multiple stages of erbium doped fiber amplifier (EDFA) and broken up into femtosecond pulses by modulation instability (MI) in ~1 m standard single mode fiber (SMF) [1,2]. The SC spectrum is broadened in the ZBLAN fiber primarily by self-phase modulation (SPM) and stimulated Raman scattering, and smoothed due to the range of intensities in the pump pulses [1-4]. The use of ZBLAN fibers with a long cut-off wavelength (2.75 μm) allows the SC edge to be extended to 4.5 μm, which is consistent with the intrinsic ZBLAN material absorption.

An all-fiber, mid-IR light source can provide significant advantages over existing IR laser light sources. Typically, mid-IR light is generated using optical parametric oscillators or quantum cascaded lasers [5]. In contrast, the fiber light source operates at room temperature with no moving parts, and the fibers have a high power damage threshold facilitating power scaling.

SC generation using various pump lasers has been widely studied in different types of

fibers. For example, SC ranging from ~0.8 μm to 2.6 μm has been generated in a highly nonlinear, silica fiber by a mode-locked femtosecond laser [6]. Amplified laser diode pulses have also been used to generate SC from 0.9 μm to 1.7 μm [7], and from ~0.8 μm to 3.0 μm in a highly nonlinear silica fiber [2]. To generate SC to mid-IR, fibers having lower loss in the mid-IR windows are required.

Fluoride fibers have the lowest loss coefficient of mid-IR fibers in the 2~5 μm region [8], and SC generation in ZBLAN fibers out to 3.4 μm was achieved with femtosecond laser pumping [9]. Our experiments, using ZBLAN fibers with a long cut-off wavelength and nanosecond pulses, lead to a simple system to generate SC out to 4.5 μm.

A two-stage approach is used to optimize the SC generation. The first stage is comprised of a 1~2 m length of SMF fiber, which is spliced to the output of the EDFA. By pumping the SMF fiber in the anomalous dispersion region, MI can be phase matched to break up the nanosecond pulses into femtosecond pulses [2], which eliminates the need for mode-locked lasers. The second stage consists of a ~2-7 m ZBLAN fiber in which the SC is broadened by fiber nonlinearities. A short length of ZBLAN fiber with long cut-off wavelength is used to achieve the broadest spectrum because the long wavelength edge is limited by the loss of the fiber.

2. Experimental setup

The experimental setup is illustrated in Fig. 2.1. The set-up emulates a Q-switched laser system. The system stores energy between pulses using the long, upper state, lifetime of EFDA, which allows a laser diode driven with a low duty cycle to produce a larger energy per pulse. A distributed feedback laser at 1553 nm is driven by a pulse generator to provide the seed light with ~2 ns pulse width at 5 kHz repetition rate. The light is amplified in a

low-noise EDFA pre-amplifier followed by an electro-optic modulator synchronized to the pulse generator to suppress the amplified spontaneous emission. The modulator loss is compensated by the mid-stage EDFA, and the output is bandpass filtered before launching into the final stage power amplifier. The light is boosted in the power amplifier to a peak power approaching ~4 kW and an average power of ~40 mW.

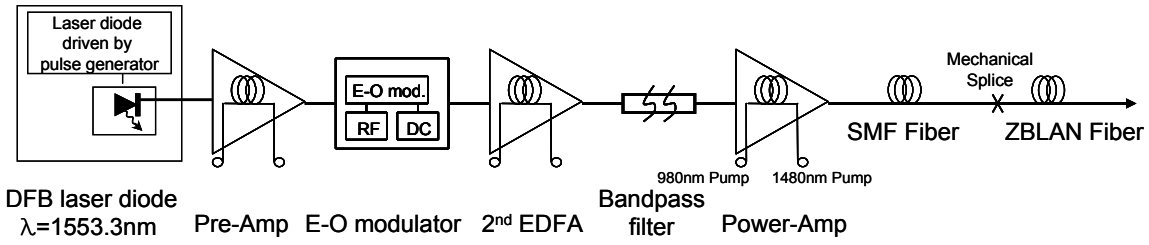

Fig. 2.1 Experimental setup for 2 ns laser diode pulses amplified in multiple stages of EDFAs.

Three fibers are used in the experiments with a cladding diameter of 125 μm and with the following characteristics (fiber name, core diameter, cut-off wavelength): (a) FL#1, 5.7 μm, 1.25 μm ; (b) FL#2, 8.5 μm, 1.75 μm; and (c) FL#3, 7 μm, 2.75 μm. According to Ref. [10], the material zero dispersion wavelength in ZBLAN is ~1.65 μm. The loss curve of FL#3 is shown in Fig. 2.2. The attenuation out to 4 μm is measured to be <1 dB/m. The loss in FL#1 and FL#2 is similar to FL#3 up to ~2.5 μm (<0.1 dB/m), but increases thereafter due to the bend-induced loss.

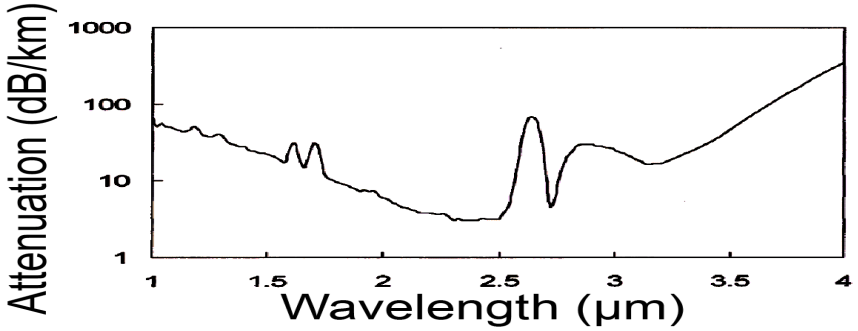

Fig. 2.2 Attenuation loss for the third ZBLAN fiber (FL#3) with a cut-off wavelength at 2.75 μm.

During the test, light from the SMF fiber is mechanically spliced to the ZBLAN fiber with a coupling loss of ~1.5 dB. Mechanical coupling also ensures single mode excitation in the ZBLAN fiber. Spectrum ranging from 700 nm to 1700 nm is measured by an optical spectrum analyzer, while the longer wavelengths are measured by a grating spectrometer using a cooled InSb detector. The interior of the spectrometer is purged by gaseous nitrogen to minimize the atmospheric water and CO_2 absorption.

3. Experimental results

Figure 2.3a shows the SC spectrum of ~7 m FL#3 following an approximately 1 m length of SMF at 4 kW peak input power. SC ranging from ~0.8 μm to more than 4.5 μm is observed with the time-averaged spectral power density of ~-20 dBm/nm over a large fraction of the spectrum. The SC average power is ~23 mW with the conversion efficiency exceeding 50% from the pump power. The peak at 1553 nm is the residual pump from the laser diode, and the features around 980 nm are due to the undepleted forward pump of the EDFA. The long wavelength edge 20 dB down is measured to be at ~4.3 μm, although the longest measured wavelength extends well beyond 4.5 μm.

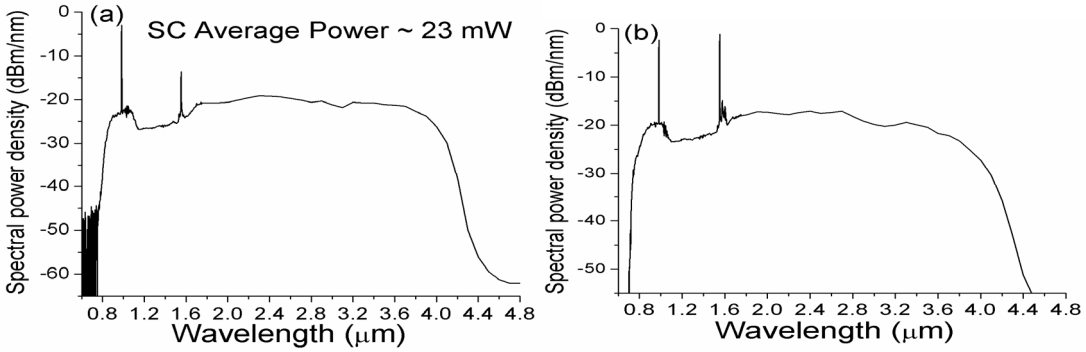

Fig. 2.3 SC Spectrum from ~1 m of SMF followed by (a) 7 m, and (b) 4.5 m of FL#3 fluoride fiber.

SC spectrum generated from ~4.5 m of FL#3 following a 1 m SMF is illustrated in Fig. 2.3b. The long wavelength edge of the spectrum is slightly shorter than the spectrum of Fig.

2.3a, but otherwise the two spectra are similar. Therefore, much of the SC spectrum is generated within the first ~4.5 m of ZBLAN fluoride fiber.

To obtain the broadest SC spectrum, the length of the each stage should be optimized. Figure 2.4a shows the spectrum for varying lengths of first stage SMF followed by 3 m length of FL#2. As can be seen, 1 m SMF leads to the broadest SC spectrum for a peak pump power in the range of 3-4 kW. Also, SC spectra generated from 1 m SMF followed by different lengths of FL#3 are illustrated in Fig. 2.4b. The SC spectrum after 4.5 m ZBLAN fiber already extends beyond 4.4 μm. Finally, Fig. 2.4c shows the SC spectra for different pump powers in 1 m SMF plus 2 m FL#3. The spectrum is generated by ~1.2 kW peak pump power and fills in as the power further increases.

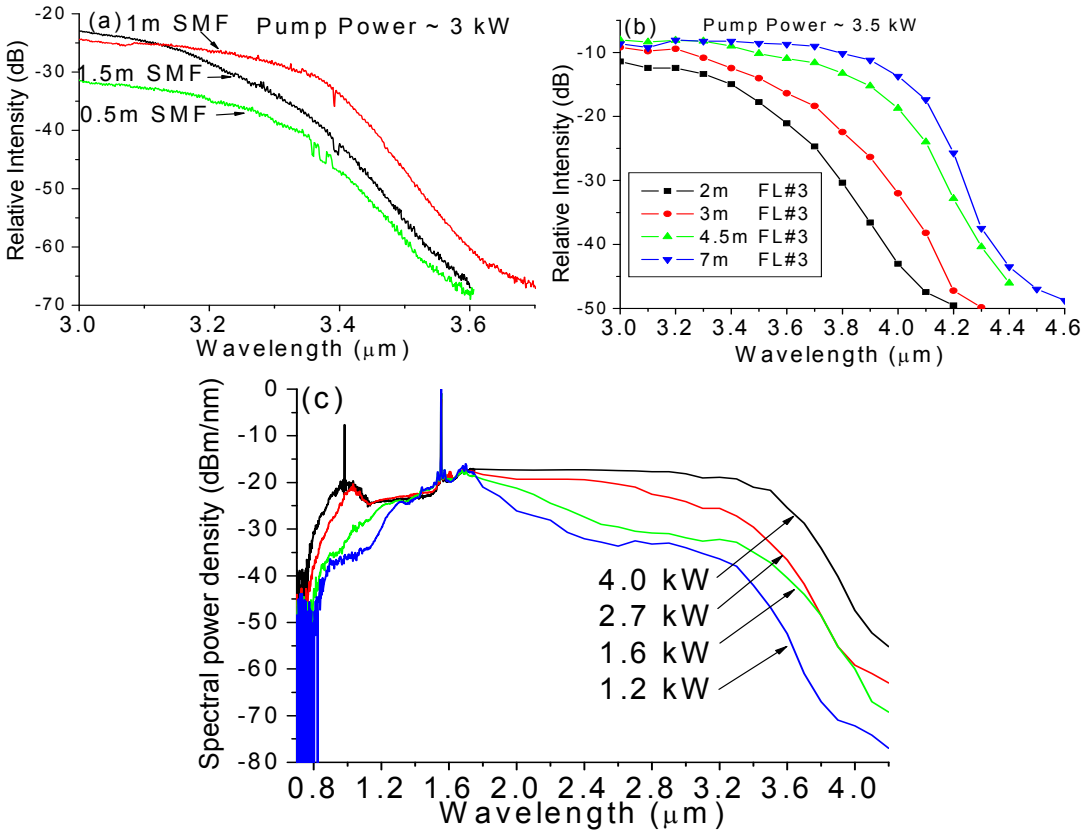

Fig. 2.4 Optimization of the SC generation by varying different parameters. (a) Different lengths of the first stage SMF fiber followed by 3 m FL#2, (b) different lengths of the second stage ZBLAN FL#3 fiber following 1 m SMF, and (c) different pump power levels in 1 m SMF plus 2 m FL#3 fiber.

4. Discussion

The spectral width observed in the ZBLAN fiber is consistent with MI-induced pulse breakup followed by SPM dominated broadening. Autocorrelation measurements and simulations show that the peak intensity of the pulses after the first stage increases approximately four-fold to ~15 kW with pulse width of ~150 fs. The spectrum broadening through SPM, ignoring fiber losses, can be approximated by $\delta f \approx n_2 P L_{eff} / A_{eff} \lambda \tau$, where n_2 is the nonlinear refractive index of fiber core, A_{eff} is the effective mode area and τ is the pump pulse width. The nonlinear refractive index n_2 is ~2.1×10^{-16} cm^2/W [11], with A_{eff} ~38 μm^2 for ZBLAN FL#3. So the SPM-generated frequency shift is ~1.4×10^{14} Hz in a 4 m length of FL#3, with the corresponding short wavelength side at ~0.9 μm, and long wavelength side at ~5.6 μm by 1.55 μm pumping. The measured edge at 4.5 μm may be due to the fiber loss, as described below. The smoothness of the SC spectrum may be due to the range of the intensities in the pulse, i.e. different temporal parts of the pulse contribute to different parts of the spectrum.

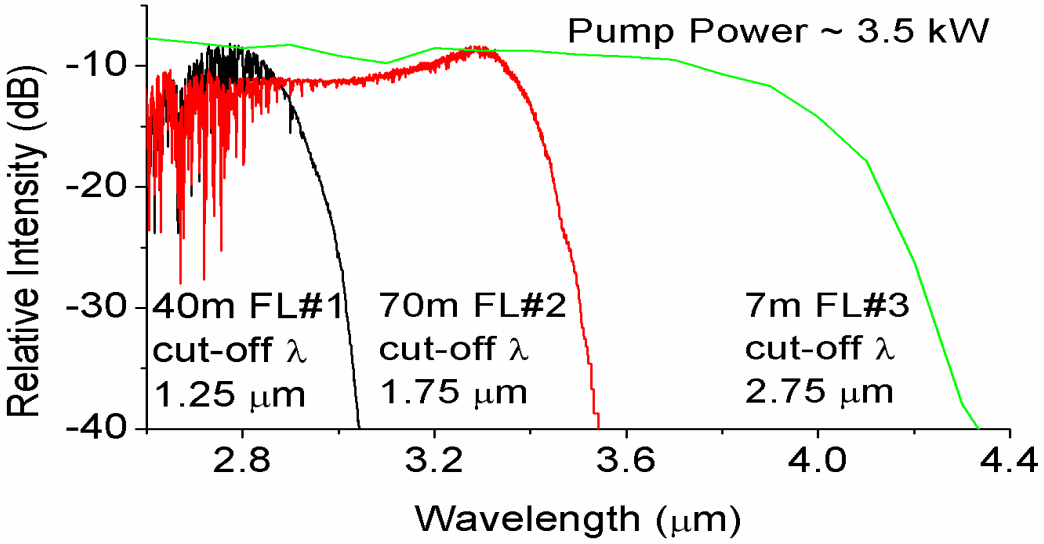

Fig. 2.5 Spectrum of the SC long wavelength side for three different ZBLAN fibers.

The long wavelength edge of the SC is limited by the loss in the ZBLAN fiber. For fibers with cut-off wavelength <~2 μm, the long wavelength loss is primarily due to the bend-induced loss. In particular, bend-induced loss is known to be wavelength dependent and increase rapidly with increasing wavelength [12]. The long wavelength spectra of the SC generated in three fibers with different cut-off wavelengths are shown in Fig. 2.5. As the cut-off wavelength increases from 1.25 μm to 2.75 μm, the long wavelength edge of the SC spectrum pushes out from ~3 μm to ~4.5 μm.

The SC long wavelength edge of FL#3 at ~4.5 μm (Fig. 2.3a) is consistent with the intrinsic ZBLAN material loss. For example, the attenuation is measured to be 1 dB/m at 4.3 μm, 2.25 dB/m at 4.5 μm and 8 dB/m at 4.8 μm in a multimode ZBLAN fiber with similar glass compositions. It should be noted that this edge is primarily due to the intrinsic loss associated with zirconium and aluminum. Therefore, fluoride glass compositions that avoid zirconium and aluminum could potentially generate SC out to 5 μm and beyond.

5. Conclusion

In summary, we have generated the broadest mid IR SC in ZBLAN fluoride fibers by laser diode pumping. The SC extended to 4.5 um with an average power in the SC of ~23 mW with power conversion efficiency over 50%. The SC is induced through MI in ~1 m of SMF fiber, and the long wavelength edge is limited by the ZBLAN fiber loss. The SC edge can be potentially extended beyond 5 μm with modified fluoride glass compositions. The SC average power can also be scaled up by increasing the pulse repetition rate while maintaining approximately the same peak power and pulse width.

Substantial contents in this chapter are published as: C. Xia, M. Kumar, O. P. Kulkarni, M. N. Islam, F. L. Terry, Jr., M. J. Freeman, M. Poulain, and G. Mazé, “Mid-infrared

supercontinuum generation to 4.5 μm in ZBLAN fluoride fibers by nanosecond diode pumping," Opt. Lett. **31**, 2553-2555 (2006).

References

[1] A. Abeeluck, C. Headley, and C. Jørgensen, "High-power supercontinuum generation in highly nonlinear, dispersion-shifted fibers by use of a continuous-wave Raman fiber laser," Opt. Lett. **29**, 2163-2165 (2004).

[2] C. Xia, M. Kumar, O. P. Kulkarni, M. N. Islam, F. L. Terry, Jr., D. A. Nolan, and W. A. Wood, "Super-continuum generation to 3 μm in fused silica fiber with nanosecond diode pumping," CLEO Conference 2006, Invited talk, CThV5.

[3] A. K. Abeeluck and C. Headley, "Continuous-wave pumping in the anomalous- and normal-dispersion regimes of nonlinear fibers for supercontinuum generation," Opt. Lett. **30**, 61-63 (2005).

[4] S. Coen, A. Chau, R. Leonhardt, J. Harvey, J. Knight, W. Wadsworth, and P. Russell, "Supercontinuum generation by stimulated Raman scattering and parametric four-wave mixing in photonic crystal fibers," J. Opt. Soc. Am. B **19**, 753-764 (2002).

[5] I. T. Sorokina and K. L. Vodopyanov, eds., *Solid-State Mid-Infrared Laser Sources*, (Springer-Verlag, Berlin Heidelberg, 2003).

[6] J. W. Nicholson, A. D. Yablon, P. S. Westbrook, K. S. Feder, and M. F. Yan, "High power, single mode, all-fiber source of femtosecond pulses at 1550 nm and its use in supercontinuum generation," Opt. Express **12**, 3025-3034 (2004).

[7] S. Moon and D. Y. Kim, "Generation of octave-spanning supercontinuum with 1550-nm amplified diode-laser pulses and a dispersion-shifted fiber," Opt. Express **14**, 270-278 (2006).

[8] J. A. Harrington, "Infrared Fibers," in *Handbook of Optics Vol. 3, Classical, Vision & X-ray Optics*, M. Bass, J. M. Enoch, E. W. Van Striland, and W. L. Wolfe, eds.(Optical Society of America, Washington DC, 2002), pp. 14.1 - 14.16.

[9] C. L. Hagen, J. W. Walewski, and S. T. Sanders, "Generation of a continuum extending to the midinfrared by pumping ZBLAN fiber with an ultrafast 1550-nm source," IEEE Photon. Technol. Lett. **18**, 91-93 (2006).

[10] M. Monerie, F. Alard, and G. Maze, "Fabrication and characterisation of fluoride-glass single-mode fibres," Electron. Lett. **21**, 1179-1181 (1985).

[11] J. M. Parker, "Fluoride glasses," Annu. Rev. Mater. Sci. **19**, 21-41 (1989).

[12] R. Morgan, J. S. Barton, P. G. Harper, and J. D. C. Jones, "Wavelength dependence of bending loss in monomode optical fibers: effect of the fiber buffer coating," Opt. Lett. **15**, 947-949 (1990).

Chapter III

High Power Supercontinuum Generation in ZBLAN Fluoride Fibers by Erbium/Ytterbium Co-Doped Fiber Amplifiers

1. Introduction

We demonstrate mid-infrared (mid-IR) supercontinuum (SC) generation in ZBLAN (ZrF_4-BaF_2-LaF_3-AlF_3-NaF) fluoride fibers with high time-averaged power. Using an erbium/ytterbium co-doped cladding-pumped fiber amplifier (EYFA) to amplify a modulated laser diode, SC ranging from 0.8 μm to ~4.0 μm with 1.3 W average power is generated in 13 m ZBLAN fibers following 3 m length of standard single mode fiber (SMF). The time-averaged power of the SC can be scaled by varying the pulse repetition rate, i.e. pulse duty cycle, while maintaining the similar peak power. The SC generation process is also simulated by solving the generalized nonlinear Schrödinger equation (NLSE) numerically [1]. By taking parameters of the different pump systems into consideration, simulations show that the spectral width of the SC is mainly determined by the pump peak power and matches with the experimental results. The average power of the SC is limited by the pump power coupled into the ZBLAN fiber.

The all-fiber SC light source provides a new platform in the mid-IR wavelength regime. Compared to the conventional mid-IR light source, such as optical parametric oscillators and quantum cascaded lasers [2], the ZBLAN SC produces the entire spectrum in the single

spatial mode and operates at room temperate. Therefore, the mid-IR light source could be a key-enabling technology for various applications such as spectral fingerprinting, semiconductor process control and combustion monitoring. For example, multiple absorption lines and spectral patterns of chemical samples under test may be simultaneously monitored to achieve higher sensitivity and selectivity. Moreover, the average power of the SC can be scaled up by increasing the pump pulse repetition rate and using higher power pump lasers.

SC generation in various optical fibers has been widely studied under different pumping sources. For example, SC ranging from 0.9 μm to 1.7 μm with 12 mW average power was generated in fused silica fibers by amplified nanosecond laser diode pulses [3]. Abeeluck et al also reported SC generation with ~550 nm bandwidth and 3.2 W average output power in highly nonlinear fibers pumped by continuous Raman fiber laser [4]. In ZBLAN fluoride fibers, SC extending out to 3.4 μm with 5 mW average power was generated by using femtosecond mode-locked laser [5]. We also generated SC to ~4.5 μm with ~23 mW average power by using amplified nanosecond laser diode pulses [6]. By using laser diode pulses and varying the pulse duty cycle, we demonstrate a mid-IR SC source of more than 3000 nm bandwidth with the average power scaled up to 1.3 W power in ZBLAN fibers.

For our experiments, the SC is generated in a two-stage process [6,7]. In the first stage SMF fiber, the nanosecond pulses are broken up into femtosecond pulses by modulation instability. The spectrum is then broadened through the interplay of self-phase modulation, parametric four-wave mixing and stimulated Raman scattering in the second stage ZBLAN fiber. Because the SC spectrum is broadened in the fiber through nonlinear phenomena, the generation process is related to the peak power of the pump pulses instead of the average power. Therefore, by changing the repetition rate of the pump pulses while maintaining a

similar pulse peak power, the average power of the SC can be scaled up or down with nearly identical spectrum.

2. Experimental setup and results

The pump laser is a fiber amplifier system, seeded with an electric-pulse-driven distributed Bragg reflector diode laser at 1548 nm (Fig. 3.1). To suppress the stimulated Brillouin scattering, the signal spectrum of the laser is broadened to ~1 nm bandwidth by chirping the phase segment of the diode. The system consists of three main amplification stages: a standard single mode core pre-amplifier, a 7 μm core double-clad fiber amplifier, and a 25 μm core double-clad fiber amplifier. The pre-amplifier stage is a 5.5 m long erbium-doped fiber amplifier (EDFA) pumped by a 320 mW 1480 nm pump diode. The second stage is an 8 m long single mode EYFA, which has a 7 μm NA=0.17 core, and a 130 μm NA=0.46 inner pump cladding. Up to 4 W pump power at 980 nm is coupled into the gain fiber. The amplified spontaneous emission of the first and second stage fiber amplifiers is suppressed by using an acousto-optic modulator and a band-pass filter. The last stage is a 5 m long large-mode-area EYFA, which has a 25 μm NA=0.1 core and a 300 μm NA=0.46 cladding. Large-mode-area fiber is used to avoid nonlinear effects in the fiber core and single mode output can be achieved by properly selecting coupling lens to match the mode of the input beam with the fundamental mode of the gain fiber. With ~30 W coupled pump power, the system outputs ~7 W amplified signal power, corresponding to pulse energy of ~23.3 μJ and pulse peak power of ~11.7 kW for 2 ns pulses at 300 kHz repetition rate.

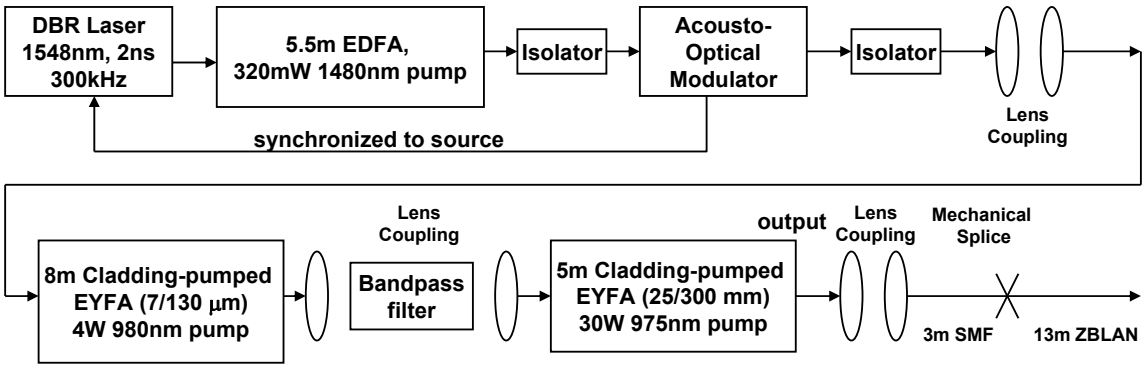

Fig. 3.1 Experimental setup comprising three-stage fiber amplifier followed by laser diode.

SC is generated in the SMF fiber followed by ZBLAN fiber. SMF fiber is used to breakup the nanosecond laser pulses, and the spectrum is then broadened in the ZBLAN fiber. The free space output light is first lens coupled into the SMF fiber with ~60% coupling efficiency. The output of the SMF fiber is then mechanically spliced to the ZBLAN fibers with ~3 dB coupling loss. Both ends of the SMF fiber and ZBLAN fiber are angle cleaved to minimize the feedback in the system. To avoid the thermal damage of the fiber under high power, the coating of the ZBLAN fiber input end is removed and the bare fiber is contacted with an air-cooled heat sink. We observe some optical damage spots in the ZBLAN fiber with coupled average power >2 W, which it is believed to be due to the contaminants in the fiber. Two ZBLAN fibers are used in the experiment, a) FL#1 has a core diameter of 7 μm, cladding diameter of 125 μm and cut-off wavelength of 2.75 μm, and b) FL#2 has a core diameter of 8.5 μm, cladding diameter of 125 μm and cut-off wavelength of 1.75 μm [6]. By using long-cut-off-wavelength fiber, the loss of the fiber on the long wavelength side can be reduced due to lower bend-induced loss. SC spectrum from 700 nm to 1750 nm is measured by using an optical spectrum analyzer, while the longer wavelength components are obtained by using a grating-based spectrometer with a liquid-nitrogen cooled InSb detector at 100 nm intervals.

SC with 1.3 W time-averaged power is generated from 3 m SMF fiber followed by 13 m FL#1 (Fig. 3.2). The SC spectrum extends from ~0.8 μm to beyond 4.0 μm by coupling ~3 kW (~1.9 W) peak (average) pump power into the ZBLAN fiber, which implies a SC power conversion efficiency from the pump of >60%, i.e. 1.3 W SC power divided by 1.9 W coupled pump power. The SC has a bandwidth of >1000 nm as the 3 dB drop and of >2700 nm as the 20 dB drop from the highest spectral power density of ~1.5 dBm/nm (1.4 mW/nm). The low power result, which is obtained in a multi-stage single-mode EDFA system [6], is also illustrated in Fig. 3.2. By pumping 1 m SMF fiber plus 7 m ZBLAN fiber at 4 kW peak power, SC with an average power of ~23 mW is generated from ~0.8 μm to more than 4.5 μm. Compared to the low power results, the SC average power is scaled up by ~65x times to ~1.3 W for the high power results. Also, we observe that the SC long wavelength edge of the high power results does not extend as far as that of the low power results. We attribute the difference to the different pump system setup, as explained below.

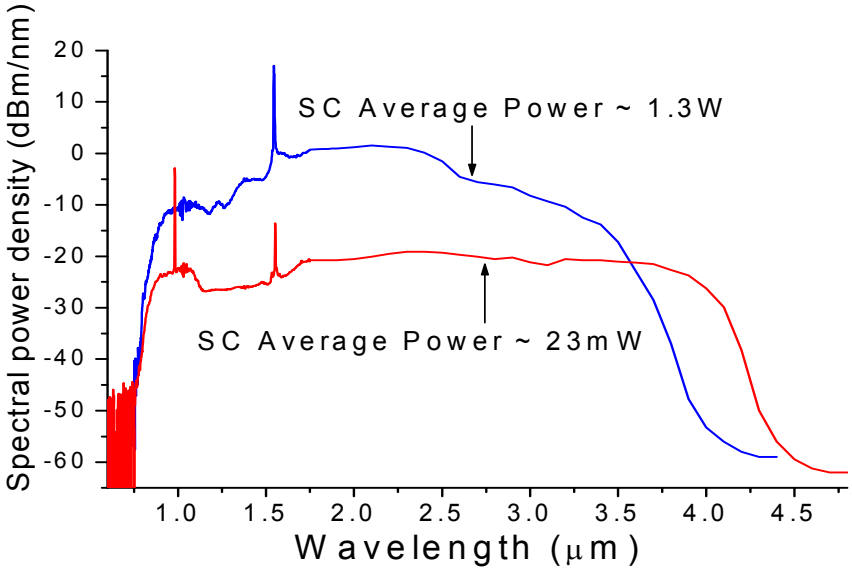

Fig. 3.2 SC spectrum from (a) 3 m SMF fiber followed by 13 m FL#1 in high power setup, and (b) 1 m SMF fiber followed by 8 m FL#1 in low power setup.

By replacing the second stage FL#1 with 10 m FL#2, SC extending from ~0.8 to 3.6 μm is generated with 1.2 W average power with ~3.5 kW coupled peak pump power (Fig. 3.3a). The SC spectrum has a bandwidth of ~2000 nm with only ~5 dB drop from the peak spectral power density and the SC conversion efficiency from the pump is >50%. Moreover, the long wavelength edge of the SC is similar to the low power results with the 3.6 μm edge, which is limited by the short cut-off wavelength and high bend-induced loss of the fiber [6]. Therefore, the SC generation is independent of the pump laser sources and amplifiers. By optimizing the length of the fiber in each stage, SC with comparable spectrum can be generated in different pump systems.

To compare the spectral shape of the SC pumped by similar pump power, similar lengths of FL#2 are tested in both low power and high power systems. By directly coupling ~1.5-2 kW peak pulse power into 60-80 m length of ZBLAN fibers, SC ranging from 0.8 μm to ~3.4 μm has been generated (Fig. 3.4b). For the 5 kHz repetition rate, SC has an average power of ~13 mW and spectral power density of ~-20 dBm/nm over the 2-3 μm wavelength range. By increasing the repetition rate to 500 kHz in the high power system, the average power of the SC is increased to 1.25 W with the spectral power density increased to ~0 dBm/nm in the same wavelength range. We observe that SCs with similar spectral shape are generated with the SC average power scaled up by a factor of 100, which is consistent with the 100x increase of the pulse repetition rate. As described above, the long wavelength edge is limited by the bend-induced loss of the ZBLAN fiber and low pump peak power [6,7]. Therefore, the SC system can scale the time-average power by varying the pulse repetition rate while maintaining the same spectral shape by keeping the similar peak pump power.

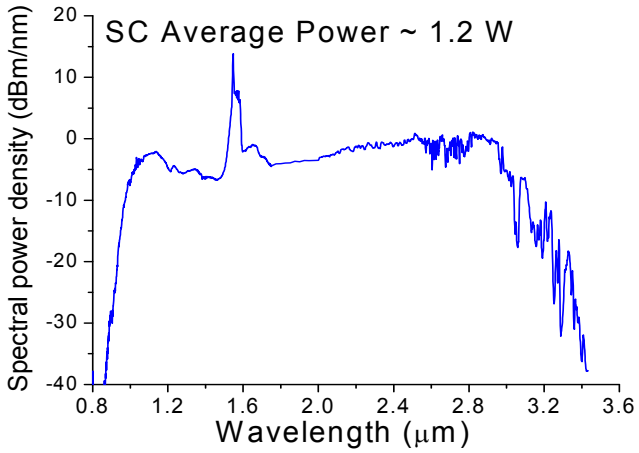

Fig. 3.3 SC spectrum from 3 m SMF fiber followed by 10 m FL#2.

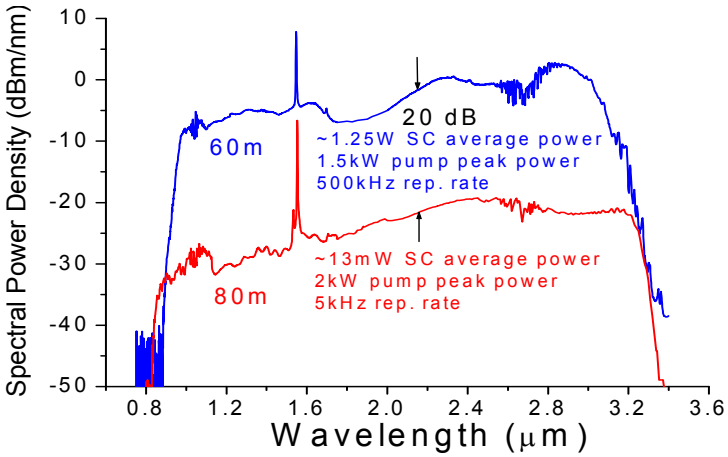

Fig. 3.4 SC spectrum from (a) 80 m FL#2 pumped by 2 kW peak power at 5 kHz repetition rate, and (b) 60 m FL#2 pumped by 1.5 kW peak power at 500 kHz repetition rate.

3. Computer simulation and comparison of experiments

To study the difference of the SC spectra generated from the low and high power pump systems, the generalized NLSE has been adopted and solved numerically. The complex envelope $A(z,\tau)$ of a pulse, under the slowly varying approximation satisfies the generalized NLSE given by [1],

$$\frac{\partial A}{\partial z} = (\hat{D} + \hat{N})A$$

$$\hat{D} = -\frac{i}{2}\beta_2 \frac{\partial^2 A}{\partial \tau^2} + \frac{1}{6}\beta_3 \frac{\partial^3 A}{\partial \tau^3} + \frac{i}{24}\beta_4 \frac{\partial^4 A}{\partial \tau^4} - \frac{\alpha}{2}$$

$$\hat{N} = i\gamma(1 + \frac{i}{\omega_0}\frac{\partial}{\partial t})\int_{-\infty}^{+\infty}[(1-f_R)\delta(t) + f_R h_R(t)]\,|\,A(z,t-t')\,|^2\,dt'$$

where the pulse moves along z in the retarded time frame $\tau = t - z/v_g$ with the center angular frequency of ω_0. The linear terms in the differential operator $\hat{D}$ account for the second (β_2), third (β_3) and the fourth order (β_4) dispersion as well as the loss (α) of the fiber. The terms in the operator $\hat{N}$ result from nonlinear interactions, which describe self-phase modulation, self-steepening and stimulated Raman scattering effects. In particular, the effective nonlinearity is defined as $\gamma = n_2\omega_0 / cA_{eff}$, where n_2 and A_{eff} are the nonlinear refractive index and effective mode area of the fiber respectively. In addition, $h_R(t)$ represents the Raman response function, and f_R is the fractional contribution of the Raman response to the nonlinear polarization.

The NLSE described above has been solved by adaptive split-step Fourier method with the initial pulse shape as the known boundary value [1,8]. The step size is determined and dynamically adjusted by the nonlinear gain in each section. Because of the large bandwidth of the SC compared to the Raman gain spectrum of the silica and ZBLAN glasses, approximation of the Raman gain as a linear function of frequency is not valid any more. Therefore, the actual Raman gain spectrum of the specific fiber in the simulator has been taken in account [1,9]. Also, material dispersion of the fiber glass is used for both SMF and ZBLAN fiber. For the SMF fiber, the effective nonlinearity γ is 1.6 $W^{-1}km^{-1}$ and Raman gain peak g_R equals to 6.4×10^{-14} m/W [1]. For the ZBLAN fiber, the effective nonlinearity γ and

the Raman gain peak g_R are assumed to be same as that of silica glass [10,11]. The simulated spectrum is averaged by every 100 nm to match the data acquisition interval of the experiment.

Figure 3.5a illustrates the simulation results compared with the experimental data in the low average power setup. In both the experiment and simulation, the generated SC has a spectrum ranging from ~0.8 μm to ~4.5 μm. The peak and features around 980 nm in the experiments are due to the undepleted pump from the amplifier, which is not included in the simulation. Also, the long wavelength side of the SC spectrum is higher and has distinct peak features in the simulation compared to the experimental results. Because the long wavelength side of the SC is mainly generated through stimulated Raman scattering, we believe that the differences between the simulation and experiment come from the approximation of the Raman gain spectrum in the simulation. Super-Gaussian pulses of 100 ps pulse width are used in the simulation to emulate the 2 ns pulses in the experiment. We observe that the soliton collision process stops for the pulses walking off from the main 100 ps pulse, which is due to the delayed response of the Raman scattering in the time domain and the anomalous dispersion of the ZBLAN fibers in the mid-infrared wavelength regime. Therefore, intra-pulse cascaded Raman wavelength shifting will be the dominant nonlinear process in these pulses, which could give rise to the peaks in the long wavelength side. The long wavelength edge of the spectrum around 4.5 μm is loss limited by the glass absorption of the ZBLAN materials [6].

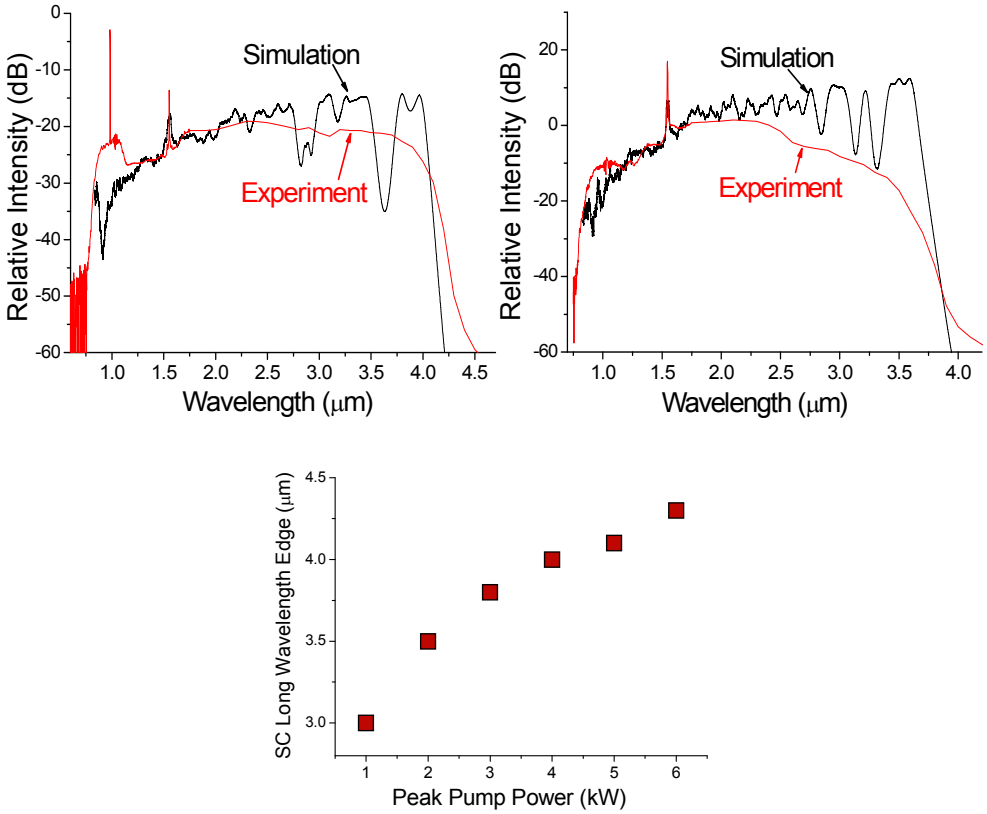

Fig. 3.5 Simulations and experiments comparison. (a) SC spectrum after 1.25 m SMF followed by 8 m FL#1 at 4 kW peak power in the low average power setup, (b) SC spectrum after 3 m SMF followed by 11 m FL#2 at 3 kW peak power in the high average power setup, and (c) SC spectrum after 3 m SMF followed by 11 m FL#2 as a function of peak pump power in the high average power setup.

For the high average power case (Fig. 3.5b), we observe that the SC long wavelength edge is limited to ~4 μm in both the experiments and simulations. The SC spectrum does not extend as far as that of low average power results. Because the peak power in the high average power case is only ~3 kW, which is lower than the 4 kW peak power in the low average power result, the nonlinear spectrum broadening effect is less and the long wavelength edge is limited. Figure 3.5c illustrates the long wavelength edge of the simulated SC, which is measured as 40 dB drop from the continuum level, under different pump powers. We can observe that the long wavelength edge extends further to beyond 4 μm when the peak pump power is larger than 3~4 kW. Therefore, SC extending to ~4.5 μm can be

generated by increasing the peak power in the ZBLAN fiber. In addition, there are not any sharp features around 1 μm in the SC compared to the low power results since the pump system is backward pumped and the light from the pump is lens-coupled into the SMF fiber. On the other hand, the disagreement between the experiment and simulation in the long wavelength edge is because of the approximation of the Raman effects and pulse width in the simulation as described above, as well as the diminished wave-guiding capability of the fiber in the long wavelength side. For the ZBLAN glass fiber, the refractive index change of the core and cladding is inversely proportional to the temperature [10]. One possible reason is that the loss of the fiber in the long wavelength side increases with the rising temperature difference between the core and cladding under high average power condition.

4. Discussion

We scale up the SC average power by increasing the pulse repetition rate of the pump system and using EYFAs. The time-averaged power of the SC is increased by a factor of 60, i.e. from ~23 mW at 5 kHz repetition rate to 1.3 W at 300 kHz repetition rate, which is consistent with the change of the pulse repetition rate. EYFAs are used to replace the EDFAs in the low power case to provide higher average power while keeping the similar pulse peak power, which ensures the same nonlinear process.

The average power and the spectral width of the SC in the high power setup are limited by the average and peak power coupled into the ZBLAN fiber from the pump system. The spectral width is limited to ~4 μm because of the relatively low peak power (3 kW). Simulation shows the spectral width of the SC can be further extended to ~4.5 μm by increasing the pump peak power to more than 4 kW. Therefore, by substituting the current pump system with higher power system, both the average power and the spectral width of the

SC can be further scaled up. It should be noted that as the average power is increased, better thermal management of the fiber is required. The air-cooled heat sink needs to be replaced by the water cooled heat sink and the ZBLAN fiber can be coated with metal-based coating to facilitate the thermal conduction.

5. Conclusion

In conclusion, we demonstrated SC generation in ZBLAN fluoride fibers of 1.3 W average power with more than 3000 nm bandwidth. The SC average power is scaled by changing the pulse repetition rate of the pump system and using EYFAs, while maintaining the same peak power and pulse width. Simulation results are obtained by solving the generalized NLSE numerically and agree with the experiments. The average power of the SC can be further scaled up by using higher power pump systems and implementing better purification process during the fabrication of the ZBLAN fibers.

Substantial contents in this chapter are published as: C. Xia, M. Kumar, M. -Y. Cheng, R. S. Hegde, M. N. Islam, A. Galvanauskas, H. G. Winful, F. L. Terry, Jr., M. J. Freeman, M. Poulain, and G. Mazé, "Power scalable mid-infrared supercontinuum generation in ZBLAN fluoride fibers with up to 1.3 watts time-averaged power," Opt. Express **15**, 865-871 (2007).

References

[1] G. P. Agrawal, *Nonlinear Fiber Optics,* 3rd edition, (Academic, San Diego, 2001).

[2] I. T. Sorokina and K. L. Vodopyanov, eds., *Solid-State Mid-Infrared Laser Sources*, (Springer-Verlag, Berlin Heidelberg, 2003).

[3] S. Moon and D. Y. Kim, "Generation of octave-spanning supercontinuum with 1550-nm amplified diode-laser pulses and a dispersion-shifted fiber," Opt. Express **14**, 270-278 (2006).

[4] A. K. Abeeluck and C. Headley, "Continuous-wave pumping in the anomalous- and normal-dispersion regimes of nonlinear fibers for supercontinuum generation," Opt. Lett. **30**, 61-63 (2005).

[5] C. L. Hagen, J. W. Walewski, and S. T. Sanders, "Generation of a continuum extending to the midinfrared by pumping ZBLAN fiber with an ultrafast 1550-nm source," IEEE Photon. Technol. Lett. **18**, 91-93 (2006).

[6] C. Xia, M. Kumar, O. P. Kulkarni, M. N. Islam, F. L. Terry, Jr., M. J. Freeman, M. Poulain, and G. Mazé, "Mid-infrared supercontinuum generation to 4.5 μm in ZBLAN fluoride fibers by nanosecond diode pumping," Opt. Lett. **31**, 2553-2555 (2006).

[7] C. Xia, M. Kumar, M.-Y. Cheng, O. P. Kulkarni, V. V. Alexander, M. N. Islam, A. Galvanauskas, F. L. Terry, Jr., M. J. Freeman, M. Poulain, and G. Mazé, "0.8-4.5 microns supercontinuum generation in ZBLAN fluoride fibers scaled up to 1.25 W power," presented at Conference on Lasers and Electro-Optics CLEO 2006, Long Beach, Calif., May 21–26, 2006, postdeadline paper, CPDA10.

[8] T. Hohage and F. Schmidt, "On the numerical solution of nonlinear Schrödinger equations in fiber optics," ZIB-report 02-04, (2002), ftp://ftp.zib.de/pub/zib-publications/reports/ZR-02-04.pdf.

[9] A. Saissy, J. Botineau, L. Macon, and G. Maze, "Raman scattering in a fluorozirconate glass optical fiber," J. De Physique Lettres **46**, 289–294 (1985).

[10] J. M. Parker, "Fluoride glasses," Annu. Rev. Mater. Sci. **19**, 21-41 (1989).

[11] Y. Dureste, "Raman amplification in fluoride glass fibres," Electron. Lett. **21**, 723-724 (1985).

Chapter IV

Supercontinuum Generation in Fused Silica Fibers

1. Introduction

Broadband supercontinuum (SC) generation in fused silica fibers has been reported using a variety of pump sources in recent years [1]. Two approaches of generating continuum are widely used - pumping a short length of highly non-linear fiber with femtosecond or picosecond pulses [2] or using continuous-wave (CW)/quasi-CW sources to pump long lengths (>100m) of fiber [3]. The broadening mechanism in the former can be attributed primarily to self phase modulation (SPM), while in the latter, spectral broadening is achieved due to the combined effects of parametric four-wave mixing and stimulated Raman scattering (SRS) [4-6]. For example, a mode-locked femtosecond erbium fiber laser was used to generate 400 mW of SC output from 0.8-2.7 μm in just 12 cm of highly nonlinear (HiNL) fiber [2]. In contrast, Abeeluck et al demonstrated a continuum extending beyond 1.75 m with ~5 W average power in 500 m of HiNL fiber pumped by a CW Raman fiber laser [3]. Recently, SC generation from ~0.8 to 1.7 m in a dispersion-shifted fiber has also been demonstrated by using amplified laser diode (LD) pulses with 30 ps pulse width [7].

We demonstrate a fused silica fiber based SC light source extending to ~3 μm with time-averaged power scaled up to 5.3 W. By using modulation instability (MI) in the fiber, the pump requirements are simplified, and the broad spectrum is obtained with nanosecond pulses and a few meters of fused silica fiber [6]. The pump consists of 2 ns LD pulses, which

are amplified to ~ 4 kW peak power in a multi-stage fiber amplifier. The pulses are launched into 2-3 m of standard single mode fiber to initiate MI induced pulse breakup, and then spectrally broadened in <1 m length of highly nonlinear fiber to obtain a continuum ranging from ~0.8-3 μm. The average power of the SC is scalable from ~27 mW to 5.3 W by varying the pulse repetition rate and using a cladding-pumped fiber amplifier. In addition, simulations have been carried out by solving the generalized nonlinear Schrödinger equation (NLSE) and agree well with the experiments. The potential applications of the demonstrated high power wideband light source include spectroscopy, chemical sensing and optical coherence tomography [8].

We generate a broad continuum by implementing the SC generation as a two step process (Fig. 4.1). In the first stage, 1.55 μm LD pulses are launched into single mode fiber, where the interaction between nonlinearity and anomalous dispersion breaks the quasi-CW input into a train of solitons through MI [5-7,9,10], and significantly increases the peak power. Thus, while many SC generation experiments use mode-locked femtosecond lasers to achieve high peak powers, MI enables the use of broad pulses from compact sources such as laser diodes and facilitates the SC generation. The generated solitons will then undergo frequency down shift through soliton self frequency shifting (SSFS) [5,11]. In the second stage HiNL fiber, the SC spectrum is further broadened primarily through the SPM effects of the ultra-short solitons [10,12]. By choosing the HiNL fiber with a zero dispersion wavelength close to the pump wavelength, the SC generation also benefits from parametric four wave mixing effects due to the reduced dispersion of the non-linear fiber [6]. The ensemble average of these solitons, which spread over the entire nanosecond wide pulse, gives rise to the broad, smooth SC spectrum [5,11,13]. Simulations show that similar spectra

can be generated by using both femtosecond and nanosecond pump lasers. The nanosecond LD pumping also simplifies the scaling up of the time-averaged power. Since the nonlinear phenomena responsible for SC generation are related to the peak power of the pump pulses, the average power in the continuum can be increased simply by increasing the pulse duty cycle while keeping the peak power approximately constant. To further concentrate majority of energy of the generated SC, we simulate and propose to generate the entire SC spectrum in a single soliton pulse by tailoring the temporal profile of the amplified LD pulses.

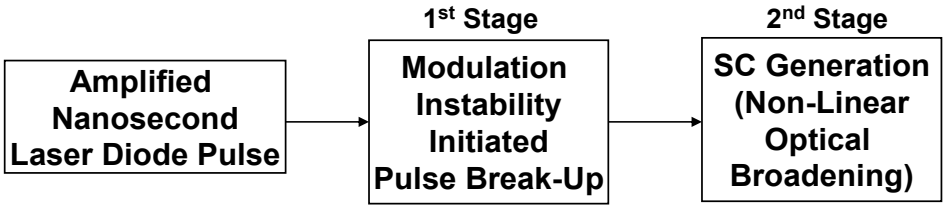

Fig. 4.1 Two step SC generation process. Pulse break up in single mode fiber followed by spectral broadening in HiNL fiber.

2. Experimental setup and results

Supercontinuum generation experiments are performed at two different repetition rates – 5 kHz and 1 MHz. The experimental setup for the low average power system (5 kHz) is illustrated in Fig. 4.2. A distributed feedback (DFB) LD at 1553 nm is driven by a pulse generator to provide 2 ns signal pulses at a 5 kHz repetition rate, corresponding to a duty cycle of 100,000:1 [10]. The pulses are amplified to ~ 4.7 kW peak power in three stages of single mode erbium doped fiber amplifiers (EDFA). We use an electro-optic modulator to suppress the in-band ASE, while a 200 GHz optical add/drop multiplexer (OADM) removes the out of band ASE. The setup is made entirely of telecommunication components and fusion spliced together with no free space elements. To generate a wide SC, the output of the power-amp is spliced to the 1st stage single mode fiber to breakup the amplified 2 ns pulses into ultra-short soliton pulses. The single mode fiber output is then spliced to the 2nd stage

HiNL fiber to achieve the desired spectral broadening. The HiNL fiber used in the experiment has a zero dispersion wavelength of 1544 nm and a dispersion slope of 0.044 ps/(km·nm^2) at the pump wavelength. The HiNL fiber is extra water-dried to minimize the water composition in the fiber. With an effective mode area of ~10 μm^2, the HiNL fiber has a non-linearity coefficient of ~9.6 W^{-1}km^{-1}. An optical spectrum analyzer is used to measure the lower end of the SC spectrum (800-1750 nm), while the long wavelength spectrum is acquired by a nitrogen purged grating spectrometer. A low noise TE cooled InAs detector connected to a lock-in amplifier is used to reliably measure the long wavelength spectrum with more than 40 dB of dynamic range.

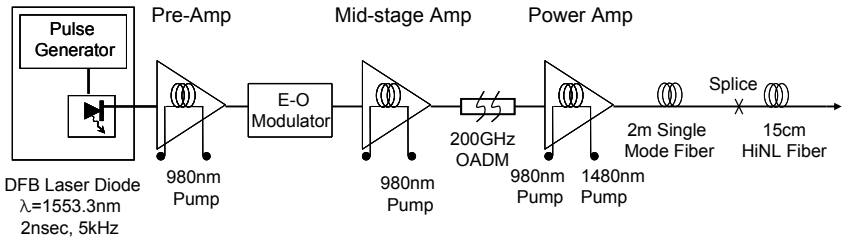

Fig. 4.2 Low average power experimental setup. LD pulses amplified by single mode EDFAs.

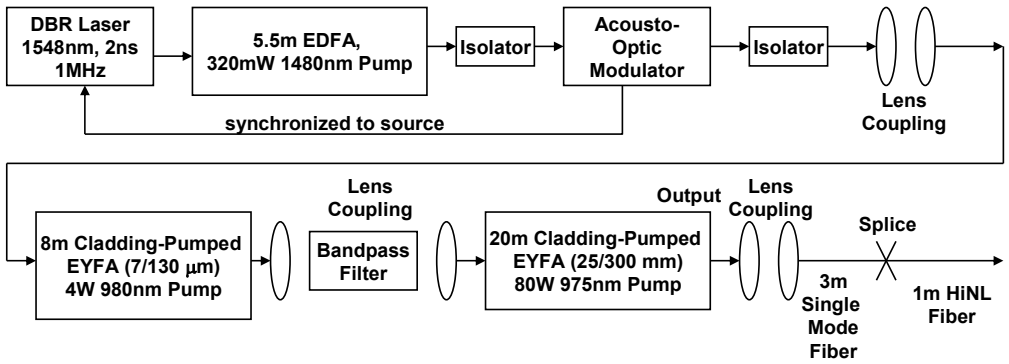

Fig. 4.3 High average power experimental setup. LD pulses amplified by cladding pumped erbium/ytterbium co-doped fiber amplifiers.

To scale up the average power in the SC, the pulse repetition rate of the pump is increased from 5 kHz to 1 MHz, while keeping the peak pump power almost constant. The high power system (Fig. 4.3) at 1 MHz (duty cycle of 500:1) has a similar experimental setup

as the 5 kHz system, with a distributed Bragg reflector (DBR) LD producing 2 ns pulses that are amplified through three stages of fiber amplifiers [14]. To suppress the stimulated Brillouin scattering, the signal spectrum of the laser is broadened to ~1 nm bandwidth by chirping the phase segment of the diode. The system consists of three main amplification stages: a standard single mode core pre-amplifier, a 7 μm core double-clad fiber amplifier, and a 25 μm core double-clad fiber amplifier. The pre-amplifier stage is a 5.5 m long EDFA pumped by a 320 mW 1480 nm pump diode. The second stage is an 8 m long single-mode erbium/ytterbium co-doped fiber amplifier (EYFA), which has a 7 μm NA=0.17 core, and a 130 μm NA=0.46 inner pump cladding. The amplified spontaneous emission of the first and second stage fiber amplifiers is suppressed by using an acousto-optic modulator and a band-pass filter. The last stage is a 20 m long large-mode-area EYFA, which has a 25 μm NA=0.1 core and a 300 μm NA=0.46 cladding. Large-mode-area fiber is used to avoid nonlinear effect in the fiber core and single-mode output can be achieved by properly matching the mode of the input beam with the fundamental mode of the gain fiber. The power-amp of this system provides a free space output with 8.8 kW peak (17.6 W average) power with ~80 W pump power, of which 3.8 kW (7.6 W) is coupled into the first stage single mode fiber.

A broad continuum extending from ~0.8 to ~3 μm is obtained with the 5 kHz system for 2 m single mode fiber followed by 15 cm length of HiNL fiber. The resulting spectrum after the single mode fiber for 4.7 kW peak (47 mW average) input power is shown in Fig. 4.4. The red-shifted spectrum after the single mode fiber extends from 1.4 – 2.5 μm and is primarily attributed to the SSFS effect. After the HiNL fiber stage, there is SPM induced spectral broadening, which further pushes out the spectrum to ~3μm on the long wavelength

side and ~800nm on the short wavelength side. The resulting supercontinuum is shown in Fig. 4.5. Both spectra have been calibrated by including the wavelength response of the grating and InAs detector. We measure the average power in the continuum to be ~27 mW, thus achieving a ~60% power conversion efficiency from pump to continuum. The spectral peak around 1550 nm is due to the LD pump while the peak at 980 nm is due to the undepleted counter-propagating pump of the power-amp. We also observe multiple absorption lines between 2.5-2.8 μm, and attribute these to the water absorption in the spectrometer.

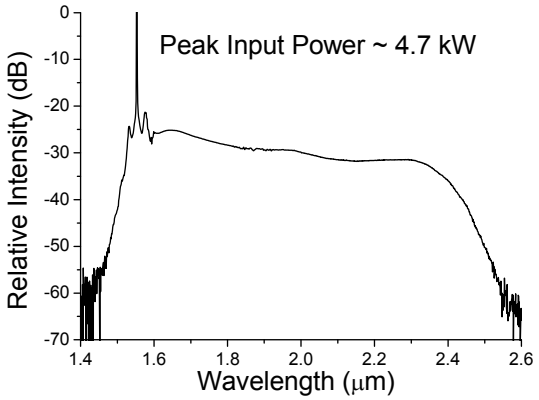

Fig. 4.4 Spectrum after 2 m single mode fiber for 4.7 kW peak input power in the low power setup.

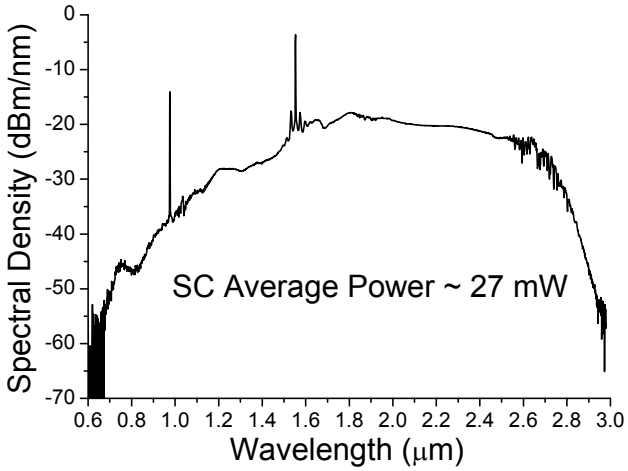

Fig. 4.5 27 mW average power SC Spectrum after 2 m single mode fiber plus 15 cm HiNL fiber in the low power setup.

To confirm that the SC is initiated by MI, we measure the temporal autocorrelation and spectrum after the 1st stage single mode fiber. The results after propagation through 3 m single mode fiber at 1 kW peak input power are shown in Fig. 4.6. The autocorrelation (Fig. 4.6a) shows the formation of short pulses with pulse envelop of ~500 fs, and the background level is due to the lower intensity pulse wings. The spectrum shows two sets of characteristic MI sidebands, with the first order sidebands separated by ~18 nm from the pump at 1553 nm. The frequency shift of the 1st order MI gain peaks from the pump is given by $\Delta\omega = (2\gamma P_0 / |\beta_2|)^{1/2}$, where γ is the non-linearity coefficient, P_0 is the peak power of the pump and β_2 is the group velocity dispersion parameter of the fiber at the pump wavelength. For single mode fiber pumped by 1 kW pulses at 1.55 μm, $\gamma = 1.6\ W^{-1}km^{-1}$, $\beta_2 = -18\ ps^2/km$ and the calculated frequency shift $\Delta\nu = 2.12$ THz. The corresponding wavelength separation is ~17 nm, which is close to the experimentally observed value in Fig. 4.6b. We observe that the 1530 nm MI gain peak coincides with the ASE peak from the EDFA, and thus the pulse break-up process is seeded by the ASE.

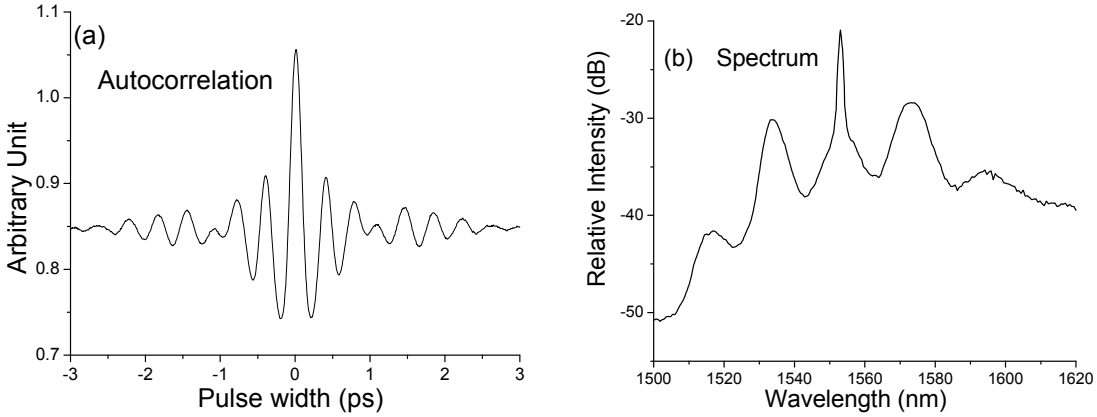

Fig. 4.6 MI induced pulse break-up in single mode fiber (a) autocorrelation, and (b) spectrum. The results are shown for 3 m of single mode fiber at 1 kW peak input power.

To optimize the 2nd stage, we studied the spectral evolution of the SC as a function of HiNL fiber length for a fixed length of single mode fiber. Fig. 4.7 shows the long wavelength spectrum for a 2 m length of single mode fiber followed by varying lengths of HiNL fiber, with each plot being on the same scale relative to the others. As the HiNL fiber length is cut back from 20 m down to 15 cm, the long wavelength edge of the SC increases from 2.6 μm to ~3 μm along with an increase in the overall spectral density. These results indicate that the nonlinear processes responsible for the wide spectrum generation occur within the first few centimeters of the HiNL fiber, and propagation through longer lengths merely attenuates the spectrum due to the high loss associated with the silica glass absorption around 3 μm. Thus, obtaining the broadest spectrum requires the shortest fiber length where nonlinearity dominates over loss.

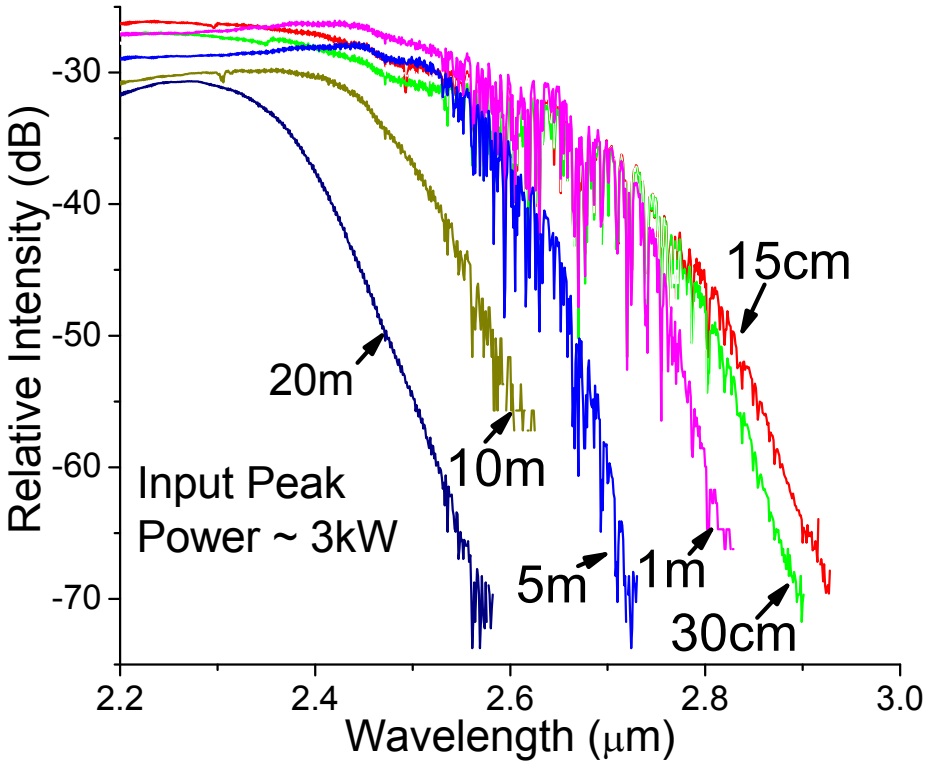

Fig. 4.7 Optimization of HiNL fiber length to achieve the longest SC edge. Spectrum after 2 m single mode fiber followed by varying lengths of HiNL fiber.

Furthermore, we measure the transmission loss of the HiNL fiber as a function of wavelength. The loss curve is shown in Fig. 4.8. It is found that the loss increases rapidly beyond 2.7 μm and is as high as 40 dB/m at ~2.9-3 μm. The loss can be possibly attributed to the water absorption, bend-induced loss and intrinsic silica glass absorption. By comparing the SC from non-dried fibers with dried fibers of 3~5 m lengths, the edge only extends ~100 nm and still does not go beyond 2.8 μm, which suggests that water absorption plays a role but is not the dominant limitation. Fibers with different core sizes and a similar index profile also give comparable edges to the SC spectrum, which downplays the significance of the bend-induced loss. Finally, the measured loss curve is in good agreement with previously published results [15], and thus, shows that the intrinsic silica loss due to vibrational absorption limits the long wavelength edge of the SC.

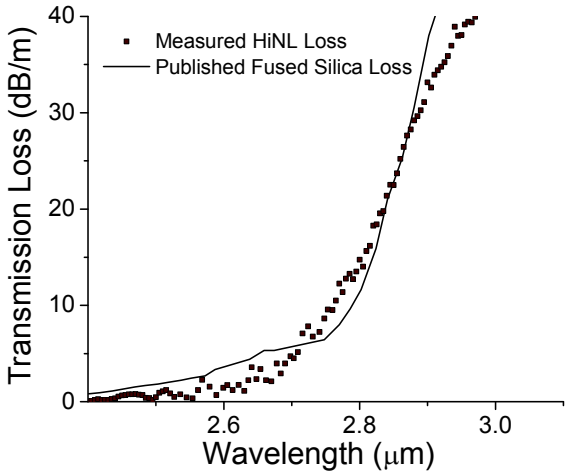

Fig. 4.8 Transmission loss in HiNL fiber. Dotted curve shows experimental results while solid curve shows previously published data.

The time-averaged power in the continuum is scaled up to 5.3 W by increasing the repetition rate of the system from 5 kHz to 1 MHz and the use of cladding pumped fiber amplifiers. The spectrum after 3 m single mode fiber followed by 1 m HiNL fiber for 3.8 kW

peak (7.6 W average) input power is shown in Fig. 4.9 and extends from 0.8-2.8 μm. For the 5 kHz system, the power in the continuum is ~27 mW, while for the 1 MHz system, it is ~5.3 W. Thus, the power is scaled up by a factor of ~195 and is consistent with the 200x increase in the repetition rate.

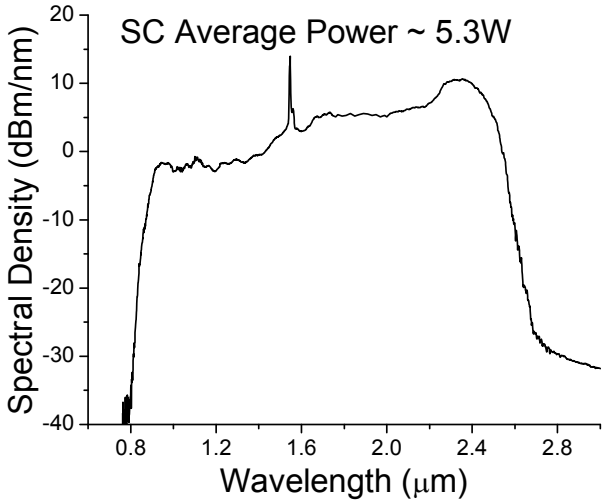

Fig. 4.9 5.3 W average power SC. Spectrum after 3 m of single mode fiber plus 1 m HiNL fiber for ~ 3.8 kW peak input power.

The difference in the single mode fiber lengths is attributed to the different fiber amplifiers used in the two systems. We notice that the broadest SC requires 3 m single mode fiber at 1 MHz but only 2 m at 5 kHz. For the 5 kHz system, the pulse break-up is enhanced by the EDFA ASE and the nonlinear effects start within the power-amp itself. But the large mode area EYFA in the 1 MHz system is designed for minimal nonlinear broadening, and thus longer lengths of single mode fiber are required to achieve a similar pulse breakup. In addition, the high average power system has about 20% lower peak power (3.8 kW) compared to the low average power system (4.7 kW). Furthermore, the difference in spectral shape of the SC in Fig. 4.9 compared to Fig. 4.3 may be attributed to the lower peak power and longer HiNL fiber length in the 1 MHz system.

3. Simulations

To further investigate and understand the SC generation mechanism under different pump systems, we numerically solve the generalized NLSE. The complex envelope $A(z,\tau)$ of a pulse, under slowly varying approximation satisfies the generalized NLSE given by [6],

$$\frac{\partial A}{\partial z} = (\hat{D} + \hat{N})A$$

$$\hat{D} = -\frac{i}{2}\beta_2 \frac{\partial^2 A}{\partial \tau^2} + \frac{1}{6}\beta_3 \frac{\partial^3 A}{\partial \tau^3} + \frac{i}{24}\beta_4 \frac{\partial^4 A}{\partial \tau^4} - \frac{\alpha}{2}$$

$$\hat{N} = i\gamma(1 + \frac{i}{\omega_0}\frac{\partial}{\partial t})\int_{-\infty}^{+\infty}[(1-f_R)\delta(t) + f_R h_R(t)]$$
$$*|A(z,t-t')|^2\, dt'$$

where the pulse moves along z in the retarded time frame $\tau = t - z/v_g$ with the center angular frequency of ω_0. The linear terms in the differential operator $\hat{D}$ account for the second (β_2), third (β_3) and the fourth order (β_4) dispersion as well as the loss (α) of the fiber. The terms in the operator $\hat{N}$ result from nonlinear interactions, which describe self-phase modulation, self-steepening and stimulated Raman scattering effects. In particular, the effective nonlinearity is defined as $\gamma = n_2\omega_0 / cA_{eff}$, where n_2 is the nonlinear refractive index and A_{eff} is the effective mode area of the fiber respectively. In addition, $h_R(t)$ represents the Raman response function, and f_R is the fractional contribution of the Raman response to the nonlinear polarization.

The NLSE described above has been solved by an adaptive split-step Fourier method with the initial pulse shape as the known boundary value [5,16]. To reduce the computation

time, we assume a 100 ps super-Gaussian pulse at 1553 nm as the input to our simulator. Simulations with pulse widths ranging 30-200 ps have also been conducted and show the same results. Furthermore, the step size is determined and dynamically adjusted by the non-linear gain in each section. Because of the large bandwidth of the SC compared to the Raman gain spectrum of the silica glass, approximation of the Raman gain as a linear function of frequency is not valid any more. Therefore, we take into account the actual Raman gain spectrum of the specific fiber in the simulator. For the single mode fiber, the effective nonlinearity γ is 1.6 $W^{-1}km^{-1}$ and Raman gain peak g_R is 6.4×10^{-14} m/W [6]. The HiNL fiber used in the experiment has a zero dispersion wavelength at 1544 nm with the effective nonlinearity coefficient assumed to be 9.6 $W^{-1}km^{-1}$.

The simulation is performed in three distinct stages in the low average power setup. The first stage simulates the output after the amplifier, i.e. before the single mode fiber, by including the non-linearity in the gain fiber. Due to large peak powers developed in the last stage amplifier and same core size of the gain fiber, we observe some spectral broadening at this stage itself, which is primarily attributed to the modulation instability seeded by the 1530 nm ASE from the amplifier.

The output from the amplifier stage is then coupled into a 2.5 m length of single mode fiber. The spectrum is red shifted to ~2.5 μm in the simulation as shown in Fig. 4.10. In the corresponding time domain, we observe the 100 ps super-Gaussian pulse breaks up into a series of short pulses. To further clarify the evolution of the pulse breakup process, Fig. 4.11 illustrates both the pulse profile and spectrum of the 100 ps input pulse. The quasi-CW input pulse from the amplifier first breaks up into a train of solitons through the MI in the fiber. In the spectrum domain, multiple side bands can be observed with the band separation inversely

proportional to the temporal separation of the soliton pulses. The generated solitons then experience frequency down shifting due to the SSFS, with the wavelength red-shifting in the corresponding spectrum.

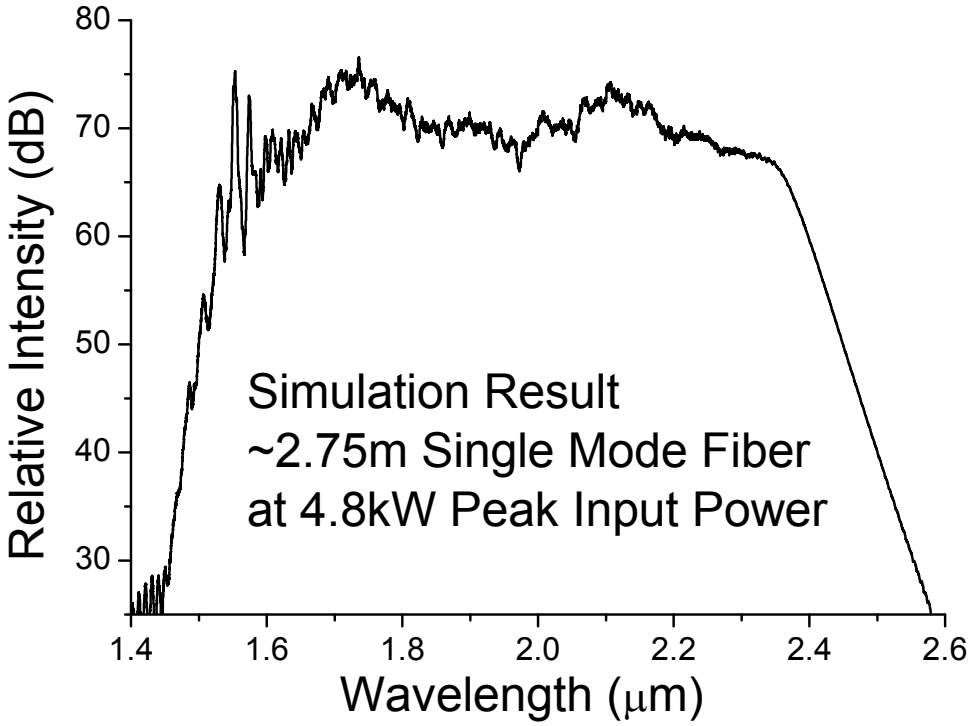

Fig. 4.10 Simulation results of low average power continuum after 2.5 m single mode fiber at 4.8 kW peak power.

The SC spectrum is further broadened in the following HiNL fiber with the simulated spectrum and pulse profile shown in Fig. 4.12. By using a short piece of highly nonlinear fiber, i.e. 15 cm, the spectrum is primarily broadened through SPM, combined with the contribution from other nonlinear effects, e.g. the generation of non-solitonic dispersive wave and cross-phase modulation [4]. The SC spectrum is smooth and flat from ~1.8-2.8 μm, whose power density is ~20 dB higher than the short wavelength side and is consistent with the experimental results.

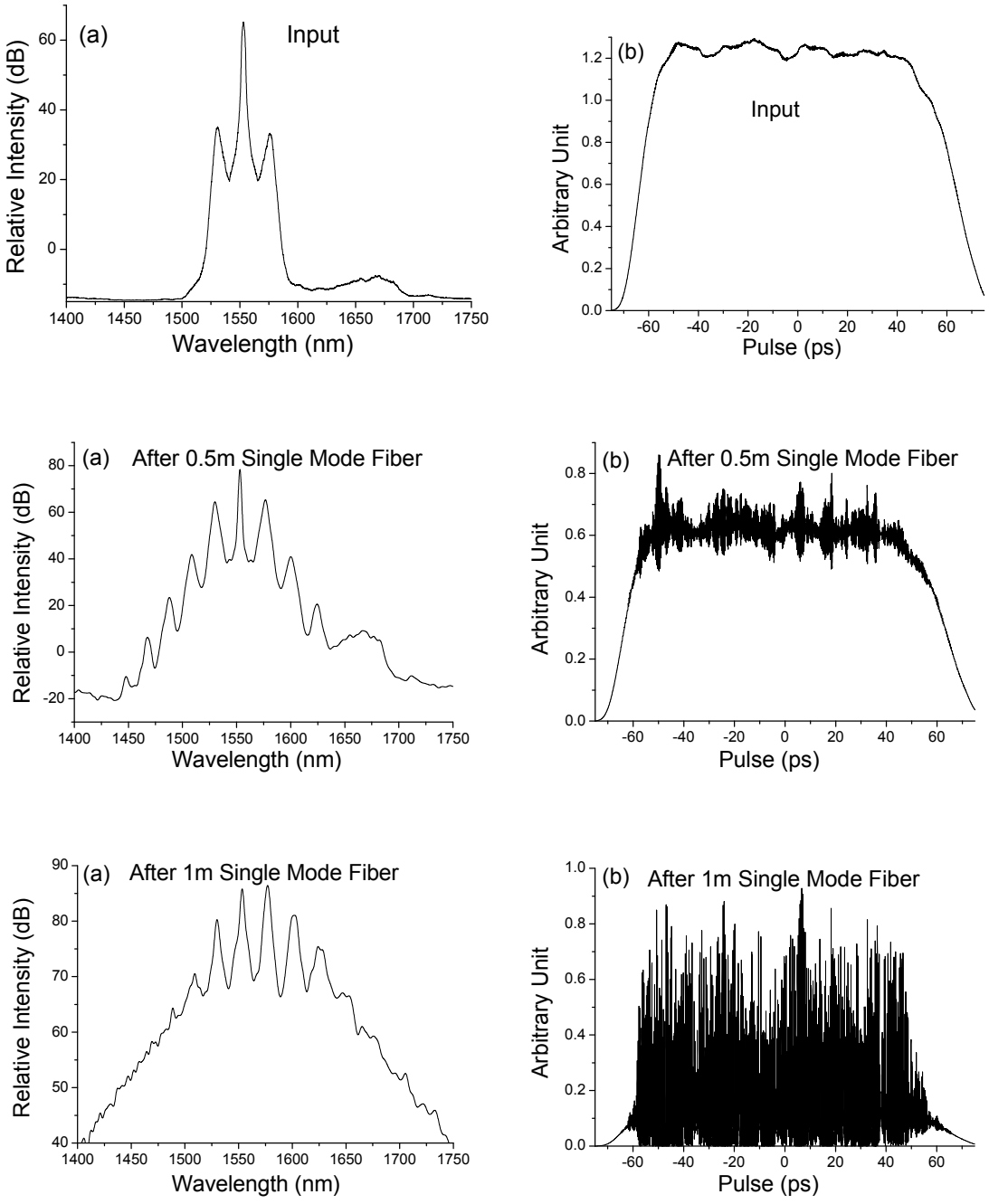

Fig. 4.11 (a) Spectrum, and (b) pulse evolution in 1 m single mode fiber as a function of propagation distance at 4.8 kW peak power.

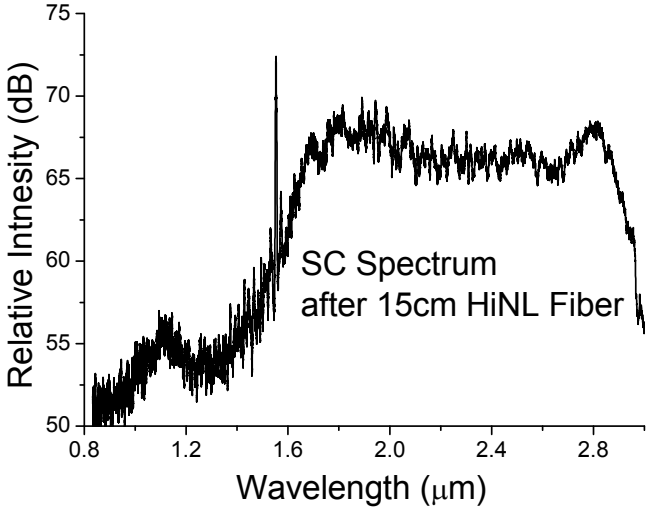

Fig. 4.12 Simulation results of low average power continuum after 2.75 m single mode fiber plus 15 cm HiNL fiber.

Compared to the SC generation by using femtosecond laser pumping [4], we generate the SC spectrum through the ensemble average of a series of independent solitons spread in the nanosecond scale. Fig. 4.13 shows spectra of three sub-pulses sliced from the different parts of the 100 ps simulated pulse. Sub-pulses in the middle and trailing edge of the pulse are composed of multiple solitons and contain the entire SC spectrum. The spectrum of the sub-pulse from the leading edge is slightly shorter in the long wavelength side. Because the red-shifted solitons travel slower than the blue-shifted spectral components in the anomalous dispersion environment, fewer red-shifted solitons remain in the leading edge of the pulse. Nevertheless, all three sub-pulses contain most of the SC spectra with comparable spectral power intensity. Therefore, the entire spectrum is a superposition of the spectra from these sub-pulses. Although each soliton may have a different nonlinear wavelength shift, the ensemble average of these solitons gives rise to a stable and smooth SC spectrum.

To further confirm our hypothesis, Fig. 4.14 simulates the SC spectrum and the corresponding pulse profile generated in 1 m length of HiNL fiber by using a femtosecond

laser with pulse width of ~150 fs at 15 kW peak power. The femtosecond pulse breaks up into multiple solitons and dispersive waves in the time domain [4] and generates a similar SC spectrum as using nanosecond pulses. Hence, by using MI to break up the nanosecond pulses into femtosecond soliton trains, LD pulses can be used to generate SC in a similar way as femtosecond lasers. Furthermore, compared to the relatively high fluctuation and instability associated with the SC spectrum generated by using femtosecond pump laser [17], we estimate the amplitude fluctuation over the entire spectrum from pulse to pulse to be less than 1% in our system.

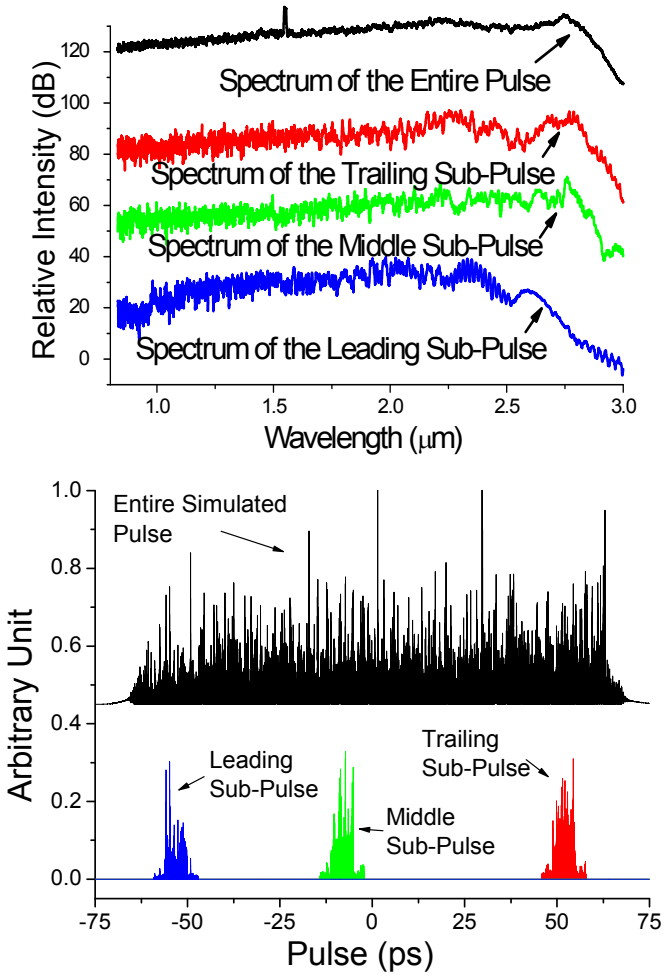

Fig. 4.13 Simulation results of the SC spectrum from different locations of the 100 ps pulse. The spectra of the sub-pulses have the similar spectral intensity and are plotted with vertical shifts for the clarification purpose.

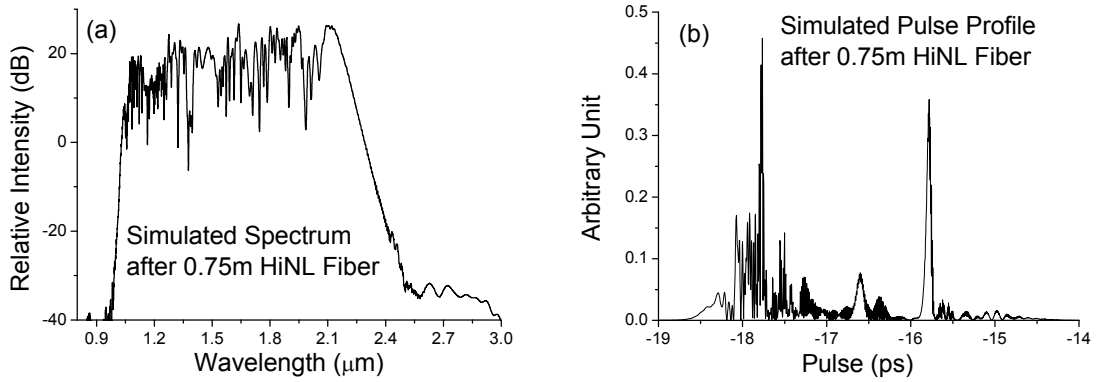

Fig. 4.14 Simulated SC. (a) Spectrum, and (b) pulse profile from 1 m HiNL fiber pumped by 150 fs pulse with 15 kW peak power.

4. SC generation in single soliton pulse

Simulations are carried out to concentrate the majority of the SC energy into one single pulse under nanosecond pulse pumping. As we analyzed above, the SC spectrum generated by amplified nanosecond pulses results from the ensemble average of a series of solitons spread in the nanosecond scale. Therefore, the entire SC spectrum is not generated in one single short pulse, which limits its potential applications such as ultra-fast time-resolved spectroscopy.

By tailoring the shape of the amplified LD pulses, we can generate one single soliton out of the entire pulse in our simulations. The proposed setup is illustrated in Fig. 4.15, with Fig. 4.16 showing the simulated temporal and spectral evolution of the pulse in the single mode fiber. The input pulse has a rising time of ~10 ps and a falling time of ~25 ps with a peak power of ~500 W. By coupling the pulse into the single mode fiber, MI phase matches and breaks up the pulse into solitons. The pulse breakup starts in the vicinity of the pulse peak because it has the highest intensity. As the pulse continues to propagate in the fiber, more solitons are generated, which are predominantly in the trailing side of the pulse due to the

asymmetric pulse shape. As the solitons compress further, the one with the highest peak power undergoes frequency down shifting by SSFS, and moves towards the trailing edge of the pulse because of the anomalous dispersion. When the dominant soliton catches up with the rest of the solitons in the trailing side of the pump, the solitons collide with each other and the red-shifted components in the dominant soliton are amplified by the Raman effect [11]. Therefore, the collision process contributes to a single soliton with narrow pulse width and high peak power. We can also observe a spectral peak around 1650 nm, which is red shifted by ~100 nm from the pump due to the SSFS. By putting a 1600 nm long pass filter to filter out the residual spectrum near the pumps, we confirm that the entire red-shift spectral peak is generated in one single dominant soliton with the pulse width of ~100 fs (full width at half maximum).

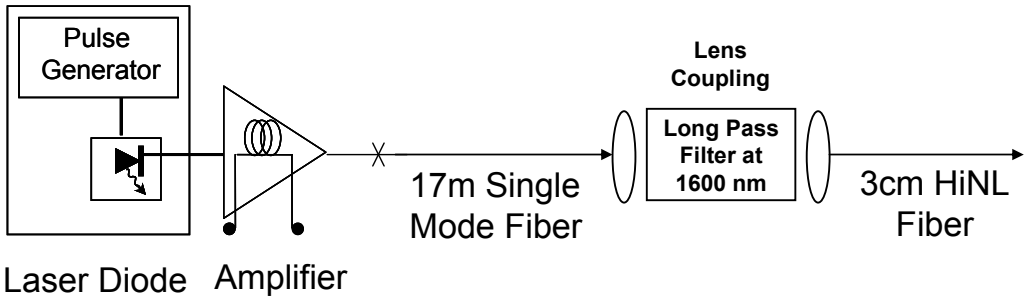

Fig. 4.15 Proposed experimental setup for the single soliton SC generation.

The generated single soliton is then launched into a short piece of HiNL fiber to generate a smooth SC. For example, SC with a continuous spectrum ranging over ~500 nm can be generated in a 3 cm length of HiNL with an effective nonlinearity ~9.6 $W^{-1}km^{-1}$ and a zero dispersion wavelength of 1544 nm. The spectrum is broadened in the HiNL fiber primarily through SPM nonlinearity. As shown in Fig. 4.17, the soliton remains compressed with the pulse envelop distorted due to the contribution of self-steepening, which will eventually break up the pulse due to the group velocity difference. Therefore, without using a

femtosecond laser pulse [4], we confine the entire SC spectrum in a single soliton pulse from an amplified quasi-CW pulse.

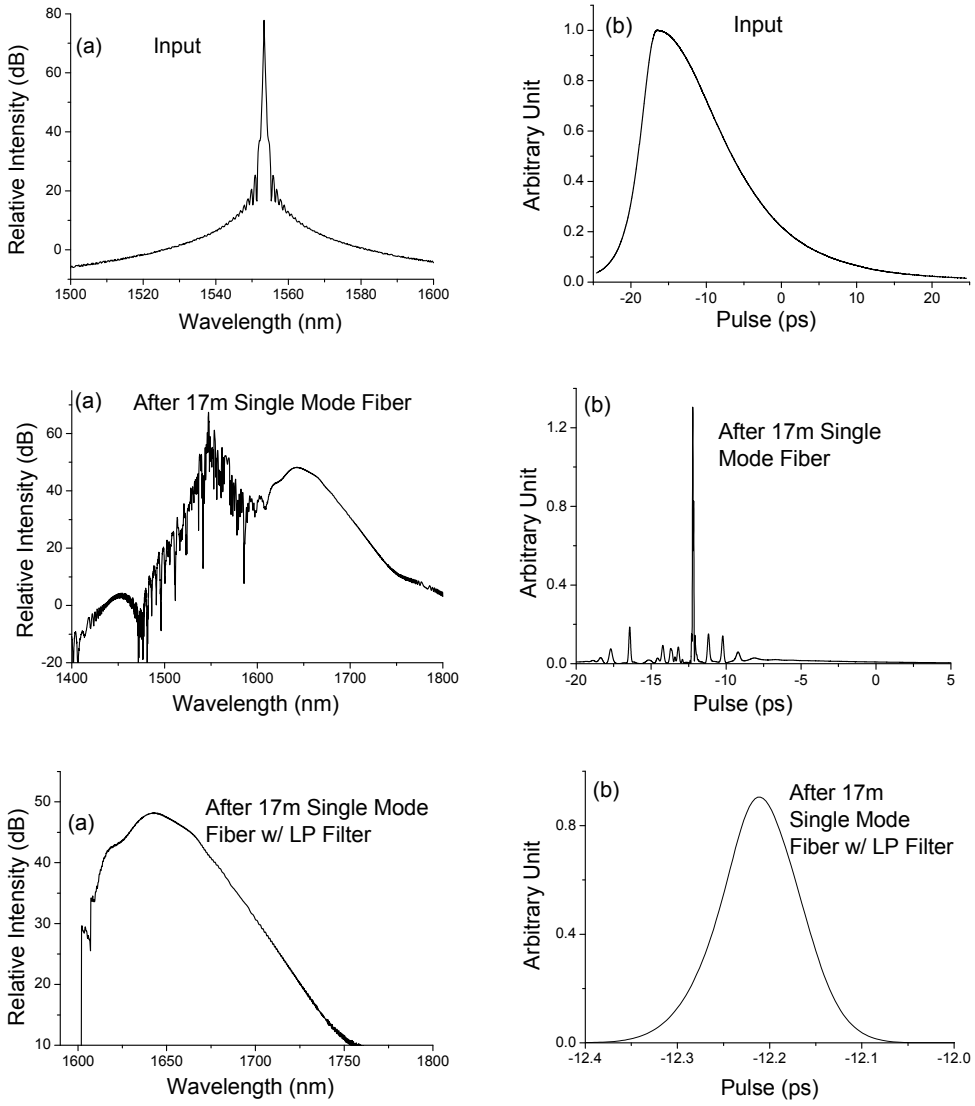

Fig. 4.16 (a) Spectrum, and (b) pulse evolution in single mode fiber as a function of distance.

It should be noted that the pulse width of input pulse does not need to be exactly as we used in the above case. For example, we obtain a similar result by using an input pulse with ~15 ps rising time and ~50 ps falling time with ~400 W peak power. In practice, such pulse can be generated through a well-designed driving circuit or with the help of a high bandwidth modulator.

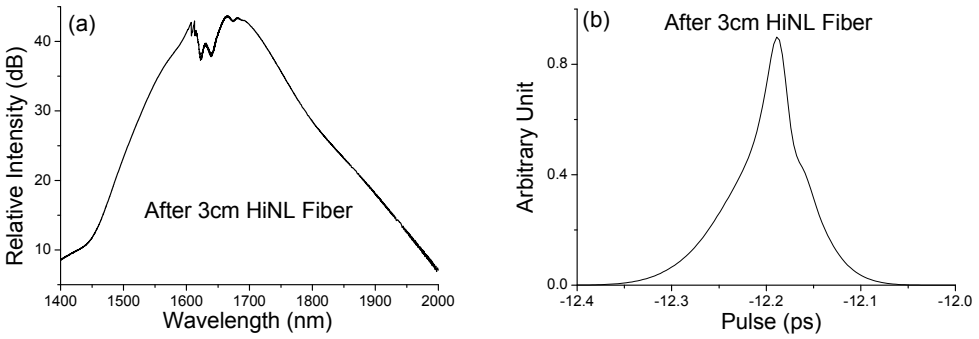

Fig. 4.17 (a) Spectrum, and (b) pulse after 17 m single mode fiber followed by 3 cm HiNL fiber.

5. Conclusion

We use nanosecond laser diode pulses amplified by multi-stage fiber amplifiers to generate SC from 0.8–3 μm in less than 4 m of fused silica fiber. A two step model based on pulse break-up in single mode fiber followed by spectral broadening in HiNL fiber is used to optimize the SC generation process, and the average power in the continuum is scaled up to 5.3 W by increasing the pulse repetition rate. We attribute the generated SC spectrum to the ensemble average of multiple solitons and non-solitonic dispersive waves. SC spectra generated through amplified nanosecond pulses are shown to be similar to the continuum generated by using femtosecond lasers. We also present a new method to generate the entire SC spectrum in one single soliton pulse by tailoring the input pulse shape.

Substantial contents in this chapter are published as: C. Xia, M. Kumar, M. -Y. Cheng, O. P. Kulkarni, M. N. Islam, A. Galvanauskas, F. L. Terry, Jr., M. J. Freeman, D. A. Nolan, and W. A. Wood, "Supercontinuum generation in silica fibers by amplified nanosecond laser diode pulses," IEEE J. Sel. Top. Quantum Electron. **13**, 789-797 (2007).

References

[1] R. R. Alfano, The supercontinuum laser source: fundamentals with updated references, 2nd ed. (Springer, New York, 2006).

[2] J. W. Nicholson, A. D. Yablon, P. S. Westbrook, K. S. Feder, and M. F. Yan, "High power, single mode, all-fiber source of femtosecond pulses at 1550 nm and its use in supercontinuum generation," Opt. Exp. **12**, 3025-3034 (2004).

[3] A. K. Abeeluck and C. Headley, "Continuous-wave pumping in the anomalous- and normal-dispersion regimes of nonlinear fibers for supercontinuum generation," Opt. Lett. **30**, 61-63 (2005).

[4] T. Hori, N. Nishizawa, T. Goto, and M. Yoshida, "Experimental and numerical analysis of widely broadened supercontinuum generation in highly nonlinear dispersion-shifted fiber with a femtosecond pulse ," J. Opt. Soc. Am. B **21**, 1969-1980 (2004).

[5] S. Kobtsev and S. Smirnov, "Modelling of high-power supercontinuum generation in highly nonlinear, dispersion shifted fibers at CW pump," Opt. Express **13**, 6912-6918 (2005).

[6] G. P. Agrawal, *Nonlinear Fiber Optics,* 3rd edition, (Academic, San Diego, 2001).

[7] S. Moon and D. Y. Kim, "Generation of octave-spanning supercontinuum with 1550-nm amplified diode-laser pulses and a dispersion-shifted fiber," Opt. Express **14**, 270-278 (2006).

[8] H. Lim, Y. Jiang, Y. Wang, Y. Huang, Z. Chen, and F. Wise, "Ultrahigh-resolution optical coherence tomography with a fiber laser source at 1 μm," Opt. Lett. **30**, 1171-1173 (2005).

[9] J. N. Kutz, C. Lyngå, and B. Eggleton, "Enhanced Supercontinuum Generation through Dispersion-Management," Opt. Express **13**, 3989-3998 (2005).

[10] C. Xia, M. Kumar, O. P. Kulkarni, M. N. Islam, F. L. Terry, Jr., M. J. Freeman, M. Poulain, and G. Mazé, "Mid-infrared supercontinuum generation to 4.5 μm in ZBLAN fluoride fibers by nanosecond diode pumping," Opt. Lett. **31**, 2553-2555 (2006).

[11] M. N. Islam, G. Sucha, I. Bar-Joseph, M. Wegener, J. P. Gordon, and D. S. Chemla, "Femtosecond distributed soliton spectrum in fibers," J. Opt. Soc. Am. B **6**, 1149-1158 (1989).

[12] C. Xia, M. Kumar, O. P. Kulkarni, M. N. Islam, F. L. Terry, Jr., D. A. Nolan, and W. A. Wood, presented at Conference on Lasers and Electro-Optics CLEO 2006, Long Beach, Calif., May 21–26, 2006, invited talk, CThV5.

[13] M. N. Islam, G. Sucha, I. Bar-Joseph, M. Wegener, J. P. Gordon, and D. S. Chemla, "Broad bandwidths from frequency-shifting solitons in fibers," Opt. Lett. **14**, 370-372 (1989).

[14] C. Xia, M. Kumar, M. -Y. Cheng, R. S. Hegde, M. N. Islam, A. Galvanauskas, H. G. Winful, F. L. Terry, Jr., M. J. Freeman, M. Poulain, and G. Mazé, " Power scalable mid-infrared supercontinuum generation in ZBLAN fluoride fibers with up to 1.3 watts time-averaged power," Opt. Express **15**, 865-871 (2007).

[15] T. Izawa, N. Shibata, and A. Takeda, "Optical attenuation in pure and doped fused silica in their wavelength region," Appl. Phys. Lett. **31**, 33-35 (1977).

[16] T. Hohage and F. Schmidt, "On the numerical solution of nonlinear Schrödinger equations in fiber optics," ZIB-report 02-04, (2002), ftp://ftp.zib.de/pub/zib-publications/reports/ZR-02-04.pdf.

[17] K. L. Corwin, N. R. Newbury, J. M. Dudley, S. Coen, S. A. Diddams, B. R. Washburn, K. Weber, and R. S. Windeler, "Fundamental amplitude noise limitations to supercontinuum spectra generated in a microstructured fiber," Appl. Phys. B **77**, 269-277 (2003).

Chapter V

All-Fiber-Integrated High Power Mid-Infrared Supercontinuum Laser System

1. Introduction

Supercontinuum (SC) generation process, in which the spectrum of a narrow bandwidth laser undergoes a substantial spectral broadening through the interplay of different nonlinear optical interactions, has been widely reported and studied since it was observed in 1969 [1]. Recently, broadband SC generation in optical fibers is of particular interest because of the optical fibers' unique advantages in their long optical interaction length, high nonlinearity, and potential applications in the optical telecommunication [2,3]. For example, a soft-glass (Schott SF6) photonics crystal fiber (PCF) has been used to generate and extend the SC spectrum down to ~350 nm in the deep blue regime [4]. Also, various techniques have been used to demonstrate SC generation with the long wavelength edge reaching as far as ~3 μm [4,5], which is then limited by the soaring material absorption of the silica glass [6]. Recently, the time-averaged power of the SC in the PCF fiber has also been increased to 50 W [7].

A high power all-fiber-integrated mid-IR SC light source has applications in a variety of areas. Conventional mid-IR laser sources, including optical parametric amplifiers (OPA) [8], quantum cascaded lasers [9], synchrotron lasers [10], and free electron lasers [11], are used in infrared countermeasures [9], free-space communications [9], and optical tissue ablation [12]. In comparison, SC lasers have no moving parts, output in single spatial mode and operate at

room temperature. In addition, fiber-based SC source can generate a broad spectrum covering the entire near- and mid-IR regime simultaneously, which can improve both the sensitivity and selectivity of remote chemical sensing [13], and real-time optical metrology [14]. Finally, direct signal modulation functionality is also desirable for SC laser sources to eliminate the need for external signal modulation or chopping equipments, which is difficult to implement in the mode-locked lasers based systems [15,16].

To generate SC spectrum in the mid-infrared (mid-IR), optical fibers with low loss in the mid-IR windows, such as chalcogenide, fluoride, and tellurite, are required. For example, spectrum shifting from 1.55 μm to ~1.9 μm is reported in the chalcogenide fibers, where further wavelength red-shifting is limited due to the low optical damage threshold of ~1 GW/cm^2 and high normal dispersion [17]. SC generation ranging from 2-3 μm has also been demonstrated in sulfide and selenide fibers by a 2.5 μm OPA pump laser [18]. On the other hand, mode-locked femtosecond lasers have been used to generate SC spectrum beyond 3 μm in both fluoride [15] and tellurite fibers [16] with modest average power (<0.1 W). We have also developed a ZBLAN (ZrF_4-BaF_2-LaF_3-AlF_3-NaF) fluoride fiber based laser source to provide a SC spectrum ranging from ~0.8 μm to ~4.5 μm [19], and we have scaled up the time-averaged output power to 1.3 W by using cladding-pumped fiber amplifiers in a table-top system [20].

We describe an all-fiber-integrated SC laser that can provide a time-averaged output power scalable up to 10.5 W in the mid-IR with direct pulse pattern modulation capability. The SC extends beyond 4 μm in ZBLAN fibers with an average output power of 10.5 W—the highest SC power reported to date in the mid-IR fibers. In addition, the average output power of the SC laser is linearly scalable with respect to the total pump power by

varying the pulse duty cycle while maintaining the similar spectral shape. For the first time to our knowledge, we also demonstrate pulse pattern modulation of the SC by directly modulating the seed laser diode and controlling the amplifier gain with signal feedback technique. Our SC laser can output a modulated pulse pattern with the duty cycle adjustable from nominally 0% to 100%. Therefore, our SC laser has no moving parts, covers the near- and mid-IR spectrum, and eliminates the need for mode-locked lasers.

The pump system of the SC laser comprises a 1542 nm laser diode generating 1 ns pulses, followed by a single mode erbium doped fiber amplifier (EDFA) and multi-stage cladding-pumped erbium/ytterbium co-doped fiber amplifiers (EYFA). Optical spectrum of the amplified nanosecond pulses is then broadened in a combination of 2 m length of standard single mode fiber (SMF) followed by 7 m length of ZBLAN fiber. Numerical simulations are also carried out to investigate the power and spectral bandwidth limit of the SC generation in ZBLAN fluoride fibers. We show that the maximum SC average power to be handled in a given fiber is constrained by thermal effects. Up to ~15 W SC can be generated in standard ZBLAN fibers, while ~40 W SC is achievable by applying a thermal coating onto the fiber to dissipate the heat. The long wavelength edge of the SC is limited by the combination of fiber bend-induced loss, fluoride material loss, and ZBLAN fiber nonlinearities. By designing a ZBLAN fiber a core size of 7 μm and a numerical aperture (NA) of 0.3, the SC long wavelength edge can be extended to ~4.5 μm, which is then limited by the material absorption loss.

2. Experimental setup

The experimental setup is illustrated in Fig. 5.1. A 10 mW distributed feedback (DFB) laser diode emitting at 1542 nm is driven by electronic circuits to provide 400 ps to 2 ns

pulses at variable repetition rate. The electronic circuits can also drive the laser diode to output a pre-programmed pulse pattern instead of fixed repetitive pulses. Details of the pulse pattern modulation will be described in Section 4. The optical pulses are amplified by three stages of fiber amplifiers—an EDFA pre-amplifier followed by EYFA mid-stage and power amplifiers. The pre-amplifier uses a 1 meter length of 4/125 μm (core/cladding diameter) single mode erbium doped gain fiber, and the mid-stage amplifier employs a 1.5 meter length of 7/125 (core/cladding diameter) cladding-pumped gain fiber. In a multi-stage amplifier, the noise performance, i.e. amplified spontaneous emission (ASE), is determined by the upstream stages before the power amplifier. To lower the ASE, we separate the amplifier into one pre-amplifier and one mid-stage amplifier. Therefore, the ASE after the first stage can be filtered by a 100 GHz bandpass filter, and the signal gain in each amplifier stage can be reduced. Optical isolators are also placed between the stages to protect the system from back-reflection damage as well as reduce the noise figure and improve the efficiency of the combined amplifier system. Under typical operating conditions, we obtain ~20 dB gain in both the pre- and mid-amplifier for the optical signal while the ASE-to-signal ratio is measured to be less than 1%. The nonlinear broadening of the optical pulses before the power amplifier is also negligible. In addition, a 1% optical tap is used to sample the output power of the pre-amplifier and to enable the signal feedback control, which is described in detail in Section 4.

The power from the mid-amplifier is boosted in an all-fiber-spliced, cladding-pumped, EYFA before coupling into the SC fiber. A cladding-pumped fiber amplifier is required to increase the gain volume and enable the coupling of multiple pump diodes. In addition, to minimize the nonlinear effects in the amplifier, a short length of gain fiber with a large core

diameter and a high doping concentration is used. For the 10 W SC generation experiment, we have designed a gain fiber with a core diameter of 15 μm and an effective NA of 0.15, whose mode field is close to that of the SMF fiber. The EYFA has a ~5 m length of gain fiber with a 15/200 μm core/cladding diameter and a 2 dB/m absorption at 915 nm. Ten 8 W 976 nm and two 8 W 940 nm uncooled multimode pump diodes are coupled into the gain fiber through an 18×1 pump combiner. Single spatial mode operation is maintained in the EYFA by carefully splicing the gain fiber to the signal-input SMF fiber and the pump combiner. By pumping the system with ~75 W average power in the counter-propagation configuration, the EYFA can provide ~20.2 W average power output after a 2 m length of SMF fiber that is spliced to the output of the gain fiber. This corresponds to ~6.1 kW peak power (~15 dB signal gain) for 1 ns pulses at a 3.33 MHz repetition rate and ~27% pump-to-signal conversion efficiency. The output spectrum after the SMF fiber is broadened and red-shifted to ~2.2 μm primarily due to the break-up of the nanosecond pulses through modulation instability (MI) followed by soliton self-frequency shifting [5]. The pump-to-signal conversion efficiency is slightly lower than the usual 30-35% figure because of the high peak power induced nonlinear wavelength generation in both the fiber amplifier and single mode fiber.

For the SC modulation experiment, we use a 12/130 μm core/cladding diameter erbium/ytterbium co-doped fiber with a 0.20 NA as the gain fiber in the final stage power amplifier. We reduce the length of the gain fiber to ~4 m because the 940 nm pump cladding absorption is increased to ~3.3 dB/m. Four 6 W, 940 nm pump diodes are coupled into the gain fiber through a 6×1 pump combiner. We generate ~6 W (~10 kW) average(peak) output power after ~2 m length SMF fiber when the seed laser is operated at 1.54 MHz repetition

rate with ~400 ps pulse duration.

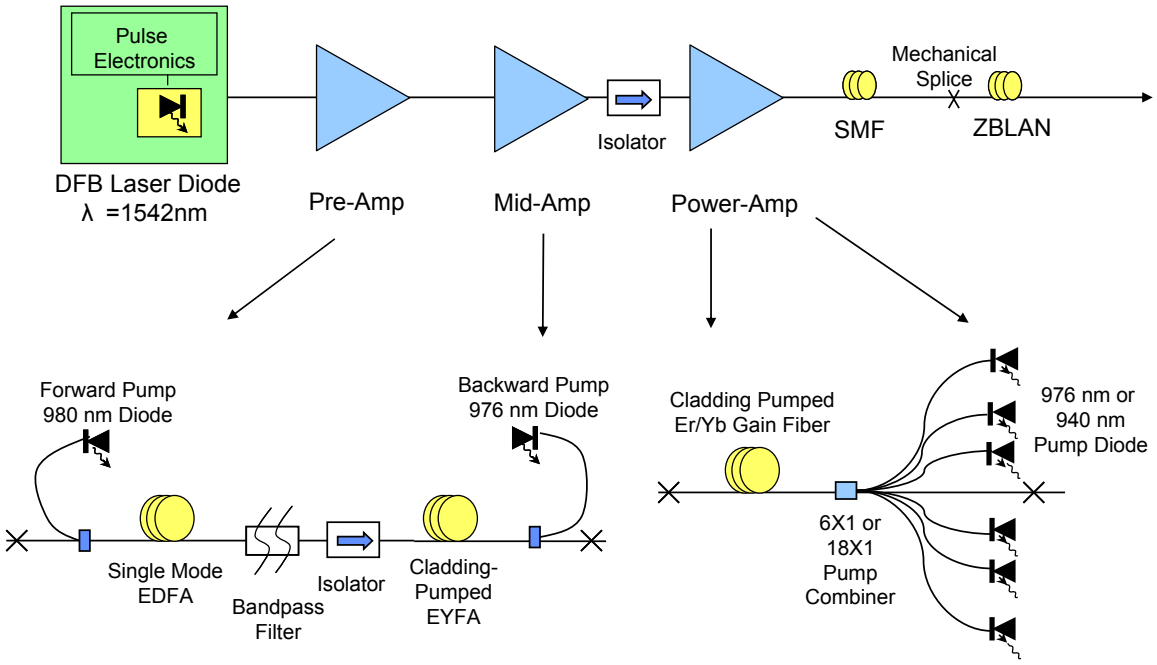

Fig. 5.1 High power all-fiber-integrated SC laser setup.

We generate the SC in a two-stage process. In the first stage SMF fiber, we utilize modulation instability (MI) to break up the nanosecond pulses into femtosecond pulse trains to enhance the nonlinear optical effects and red-shift the optical spectrum to beyond 2 μm [5]. The SC spectrum is then broadened in the following ZBLAN fiber through the interplay of self-phase modulation, Raman scattering and parametric four-wave mixing [5,20].

SC is generated by butt coupling the light from the 2 m length of SMF fiber after the EYFA into a piece of ZBLAN fluoride fiber. Two ZBLAN fluoride fibers are used in the experiments. In the 10.5 W high power SC experiment, the ZBLAN fiber we designate as FL#1 is 7 m long and has a core diameter of 8.9 μm, a cladding diameter of 125 μm and an

NA of 0.21. The ZBLAN fiber we call as FL#2 is used in the SC modulation experiment has a length of ~15 m with a core diameter of 10.6 μm, a cladding diameter of 125 μm and an NA of 0.2. All ends of SMF and ZBLAN fibers are angle-cleaved to avoid light back reflected into the pump system. To improve the coupling stability and heat dissipation capacity, each end of the butt-coupling fibers, i.e. SMF and ZBLAN fibers, is mechanically clamped onto an aluminum v-groove and the fiber claddings are covered with a high refractive index optical glue to remove the residual cladding modes. The SC spectrum between 500 nm and 1750 nm is measured by an optical spectral analyzer, while the spectral information ranging from 1750 nm to 4500 nm is acquired using a Czerny-Turner monochromator and a liquid nitrogen cooled InSb detector..

3. 10.5 W SC generation in ZBLAN fibers

Mid-IR SC with a time-averaged power of 10.5 W and a continuous spectrum of ~0.8 to more than 4 μm is generated by pumping a ~2 m length of SMF fiber followed by ~7 m length of ZBLAN fluoride fiber (FL#1) with the amplified nanosecond pulses as illustrated in Fig. 5.2. The generated SC is smooth and relatively flat across the majority of the spectrum with a spectral power density >0 dBm/nm (1 mW/nm). The measured SC spectrum is corrected for the spectral responsivity of the InSb detector. The spectral power density is then calculated by using the total SC output power measured by the thermal power meter. The pump to SC conversion efficiency in the ZBLAN fiber is >50%, i.e. 10.5 W of SC output / 20.2 W out of the SMF fiber. The SC average power beyond 1600 nm, 2500 nm, and 3000 nm is measured to be ~7.3 W, ~3.0 W and ~1.1 W, respectively, by using long pass filters with the corresponding cut-off wavelengths. The residual power in the 1550 nm pump wavelength is less than 0.1 W. The average power of the SC is currently limited by the

available pump power from the fiber amplifiers. The long wavelength edge of the SC is primarily limited by the length of the ZBLAN fiber in conjunction with other optical effects, including the fiber bend-induced loss and ZBLAN material absorption [19,20]. Detailed discussion and analysis on the limitation of SC spectral bandwidth is carried out in Section 6.

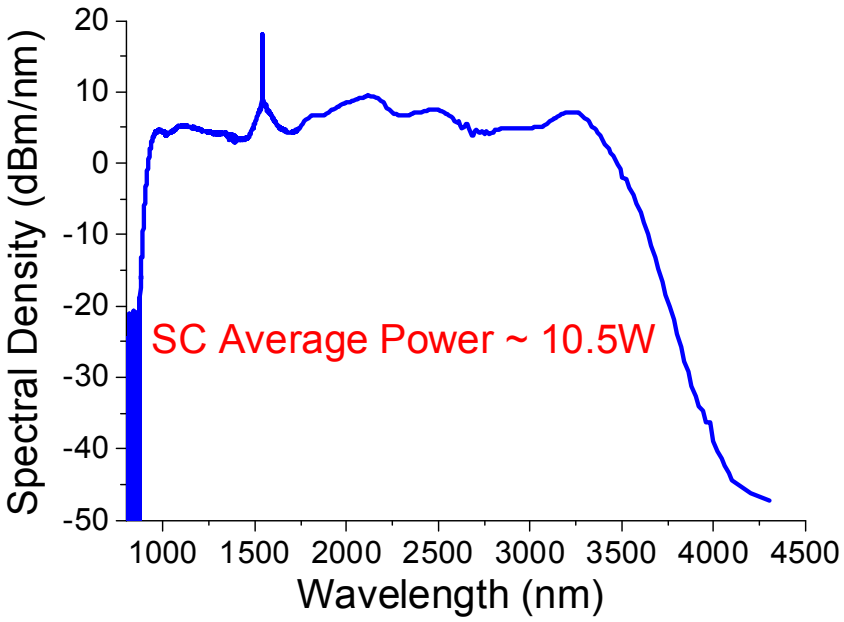

Fig. 5.2 SC Spectrum for 2 m SMF followed by ~7 m ZBLAN fiber (FL#1).

For a given fiber, there are three adjustable parameters in our SC light source, which are pulse width, repetition rate and pump power. To obtain the maximum SC power in the mid-infrared and generate the broadest spectrum, all three parameters should be optimized. The laser pulse width is set based on the following two criteria. First, the pulse width shall be short enough to mitigate any transient thermal effects in the optical fiber. On the other hand, a nanosecond pulse scale is also preferable for the intra-pulse nonlinear interaction and spectrum broadening. Therefore, we drive our DFB laser diode with the pulse width in the range of 0.4-2 ns. Furthermore, the pulse repetition rate couples with the pulse width to determine the duty cycle of the laser system. Since the DFB laser diode pulses remove the

energy provided by the EYFA pump lasers of the power amplifier of the SC system in the time between DFB pulses, the peak output power varies inversely with the pulse duty cycle with a fixed pump power supply. In other words, the peak output power increases with the reduction of the pulse repetition rate, i.e. pulse duty cycle, and vice versa.

Figure 5.3 shows the average power of SC spectral components beyond 3000 nm for varying pulse repetition rate with four 976 nm pump diodes. As can be seen, the total SC spectral power beyond 3000 nm increases from ~0.19 W to ~0.48 W by reducing the pulse repetition rate from 1.33 MHz to 0.67 MHz. We attribute the increase of spectral power to the boost of the peak power coupled into the SMF and ZBLAN fibers to enhance the nonlinear SC generation process [5,20]. However, the SC power beyond 3000 nm drops down to ~0.26 W when we further decrease the repetition rate 0.25 MHz. The drop of the SC spectral power can be caused by the increased power loss in the SC long wavelength edge and reduced amplifier conversion efficiency in the low duty cycle operational condition. Since the SC long wavelength edge is limited by the loss of the fiber, including both bend-induced loss and fluoride material loss, the additional spectrum generated in the vicinity of the SC edge by the additional peak power is heavily attenuated, which in turn reduces the total SC power in the mid-IR regime. In other words, despite of the fact that higher peak power could lead to more spectral broadening, such spectral components vanish during their propagation in the ZBLAN fiber and are not observed at the output end. Therefore, the SC light source should be operated at the repetition rate of 0.67 MHz in this particular case to achieve the maximum spectral output in the mid-IR.

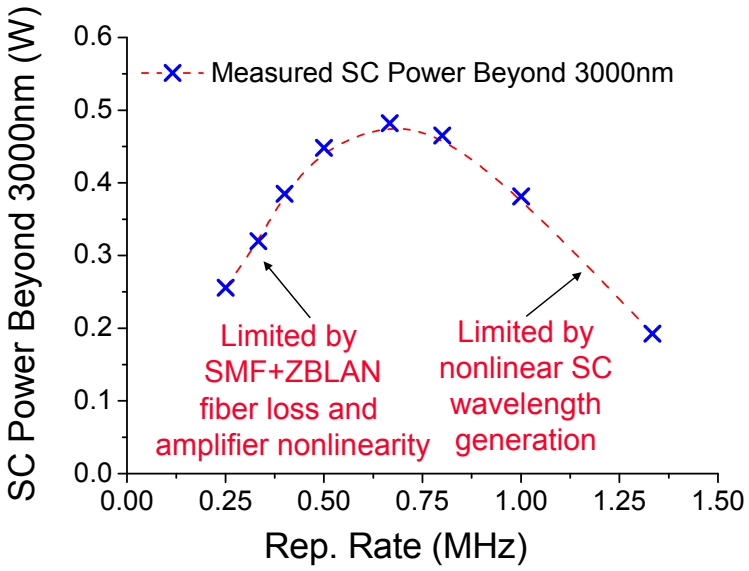

Fig. 5.3 Average power of SC spectral power beyond 3000 nm by varying pulse repetition rate with four 976 nm pump diodes.

The time-averaged power of SC is linearly scalable with respect to the input pump power without changing the spectral shape. Since the entire SC spectrum is generated in each amplified nanosecond laser pulse, which does not interact with adjacent optical pulses, the SC average power can be boosted by simply increasing the total number of the optical pulses in the given time period. To ensure the SC spectral shape is maintained, the peak power of the amplified pulses are kept the same by adjusting the pulse repetition rate and total pump power for the fiber amplifiers. As illustrated in Fig. 5.4a, we scale the SC average power from 1.4 W to 10.5 W by varying the pulse repetition rate proportionally from 0.42 MHz to 3.33 MHz and increasing the pump power accordingly. The change of the SC average power is linearly proportionally to the change of the pulse duty cycle, which agrees well with our hypothesis. To further confirm that the same SC spectrum shape has been generated under during the change of the SC average power, the ratio of the SC spectral power beyond 2500 nm over the total SC power is measured and shown in Fig. 5.4b. We observe that the ratio stays approximately constant across the entire power range, which indicates that the power

generated in the mid-IR scales up proportionally to the increasing total SC power. Therefore, the output power of our SC light source can be linearly and continuously varied with respect to the input pump power while keeping the same spectral shape.

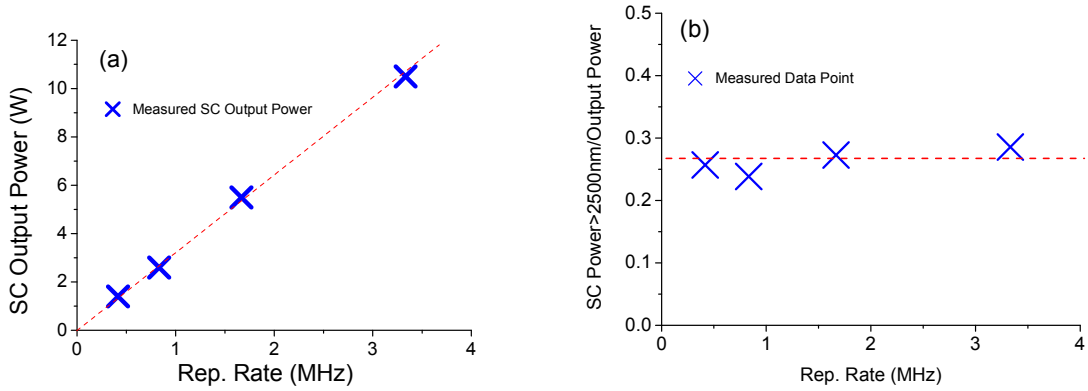

Fig. 5.4 SC average power scaling. (a)Average SC output power scaling by varying pulse repetition rate and pump power, and (b) ratio of the SC power of the spectral components beyond 2500 nm with respect to total SC power under different operating repetition rates.

4. Pulse pattern modulation of the SC light source

We demonstrate pulse pattern modulation of our SC source by directly modulating the seed laser diode and controlling the signal gain of the power amplifier. To modulate the SC output, the optical pump pulses amplified by the multi-stage fiber amplifiers need to be temporally encoded with the desirable pulse pattern. However, constant input power level is required to saturate the amplifier during the time period of the SC-off coding pattern to prevent storage of excess energy in the EYFA that would otherwise damage the amplifier [21].

We modulate the SC output, i.e. turn the SC output on/off, by feeding pump pulses that are temporally patterned with high/low peak power to the ZBLAN fiber. SC generation is a nonlinear optical process, thus the broadband SC spectrum can only be generated by amplified laser diode pulses with sufficient peak power, which typically needs to be in the kilowatt range. Figure 5.5 illustrates an exemplary pump pulse pattern, where a “1” code

represents the one SC-on pulse and a “0” code represents a series of SC-off mini-pulses. To enable the SC output, a high peak power bearing pump pulse can be coupled into the ZBLAN fiber to generate the broadband spectrum. On the other hand, a series of mini-pulses with low peak power, which undergo minimal nonlinear broadening in the ZBLAN fiber, are used to nullify the SC output. Therefore, the SC output can be directly modulated by temporally encoding the pulse pattern onto the driving currents for gain-switching DFB seed laser diodes.

We use mini-pulses during the SC off time period to saturate the power amplifier and maintain the same signal gain level for the succeeding SC-on pump pulses. In order to keep the gain of the power amplifier the same for both SC-on pump pulses and SC-off mini-pulses, the average output power of the pre-amplifier needs to stay unchanged. We use a feedback loop technique to continuously sample the output power of the pre-amplifier and then adjust the DFB seed laser power level accordingly to maintain constant output power. The 1% optical tap for signal strength monitoring is placed after the pre-amplifier and the bandpass filter, but before any of the middle stage amplifier components. This allows the signal to be strong enough that a 1% coupling still has a high signal-to-noise ratio (SNR) but avoids any significant nonlinear effects in the fiber and keeps detector saturation to a minimum. Placing the 1% tap after the 100 GHz bandpass filter assures that the signal seen by the feedback loop and the middle stage amplifier are nearly identical, since the seed laser diode puts out a much higher percentage of power into wavelengths other than 1542 nm for the mini-pulses that are barely above threshold than it does for the main pump pulses. In particular, the pulse repetition rate is set to 1.54 MHz for the SC-on pump pulses and is switched to 50 MHz for the SC-off mini-pulses. Since the average power of the amplifier system remains unchanged,

the peak power for the mini-pulse is reduced to <1/30 that of the normal pump pulse.

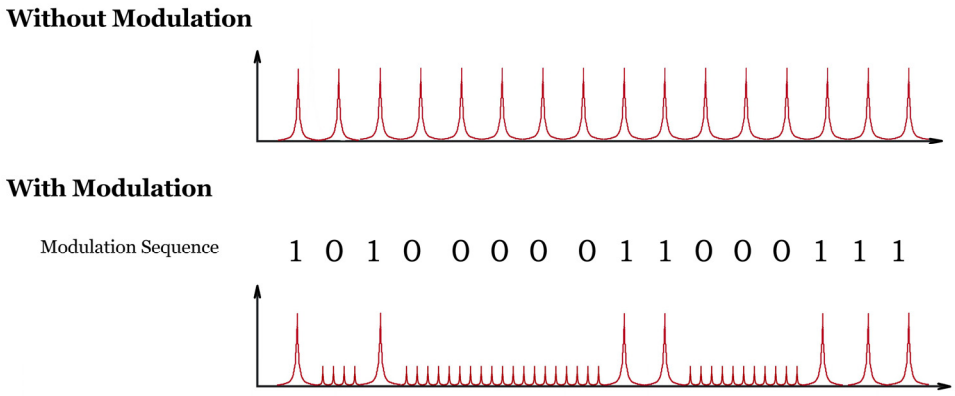

Fig. 5.5 Pump pulse modulation pattern (not drawn to scale). "0"/"1" represents SC off/on code.

Figure 5.6a shows a sample modulation pattern output of our SC source. The SC laser is operated at a base repetition rate of 1.54 MHz with pump pulse duration of 400 ps. The output power of the SC is measured to be ~2.4 W un-modulated. Two pulse envelops are encoded into the SC output—one has a width of 130 μs repeating at 1.5 kHz and the other has a width of 650 μs repeating at 7.7 kHz. Therefore, the modulation pattern consists of a 200 pulse burst with a temporal duration of 130 μs, followed by a SC-off time of 130 μs, plus another 1000 pulse burst with a temporal duration of 650 μs, followed by a SC-off time of 650 μs. The resulting duty cycle is 50% of the nominal SC output with the 1.54 MHz continuous repetitive pulses. One thing to notice is that the pulse trace displayed in Fig. 5.6a shows a ~25% peak to peak variation. We attribute such amplitude variation to the limited bandwidth and memory depth of the oscilloscope used in the experiments, which leads to under-sampling of each pulse in the train and uncertainties in the pulse to pulse variation measurement. We have also used a fast oscilloscope (500 MHz bandwidth) to measure the peak-to-peak energy variation on a single pulse in the fix repetition rate mode at 1550 nm and 2555 nm. The peak-to-peak power variation is estimated to be approximately 3%.

The modulated SC spectrum is plotted in Fig. 5.6b overlapping with the un-modulated spectrum. The SC spectrum shown in Fig. 5.6 is generated in FL#2 and has similar spectral bandwidth as that generated in FL#1. The amplitude of the SC spectrum in the modulation mode in Fig. 5.6 is vertically displaced to match the SC spectrum in the un-modulated mode. We observe no discernible changes in the SC spectrum in both the long and short wavelength side. The spectral power remaining in the vicinity of the pump wavelength in the modulation mode is ~10 dB higher than that of un-modulated mode, which could be attributed to the optical power of the SC-off mini-pulses. The modulated SC outputs 3.45 W in total, within which ~1.2 W is estimated to be in the continuum. The measured modulated SC output correlates to the powers in the un-modulated mode with the 50% duty cycle. The residual power, i.e. 3.45 W-1.2 W, is composed of ~1 W remaining in the pump and the rest of the power representing spectral components with small wavelength shifting in the vicinity of pump wavelength. Future work will be conducted to increase the SC-off pulse repetition rate beyond 100 MHz to further reduce the peak power of the mini-pulses and the corresponding nonlinear wavelength shifting.

The modulation duty cycle of our SC laser can be adjusted from nominally 0% to 100%. We estimate the saturation time of the power amplifier is ~10 μs. As previously mentioned, a series of mini-pulse are injected into the power amplifier at the SC-off period to maintain the constant average output power of the amplifier. The switching time between regular pump pulse and mini-pulse is ~100-150 ns in our driving circuits for the seed laser diode. We also observe a slight “ramp up” region at the start of each pulse envelop in Fig. 5.6a which is due to the transient laser diode driver circuit response.

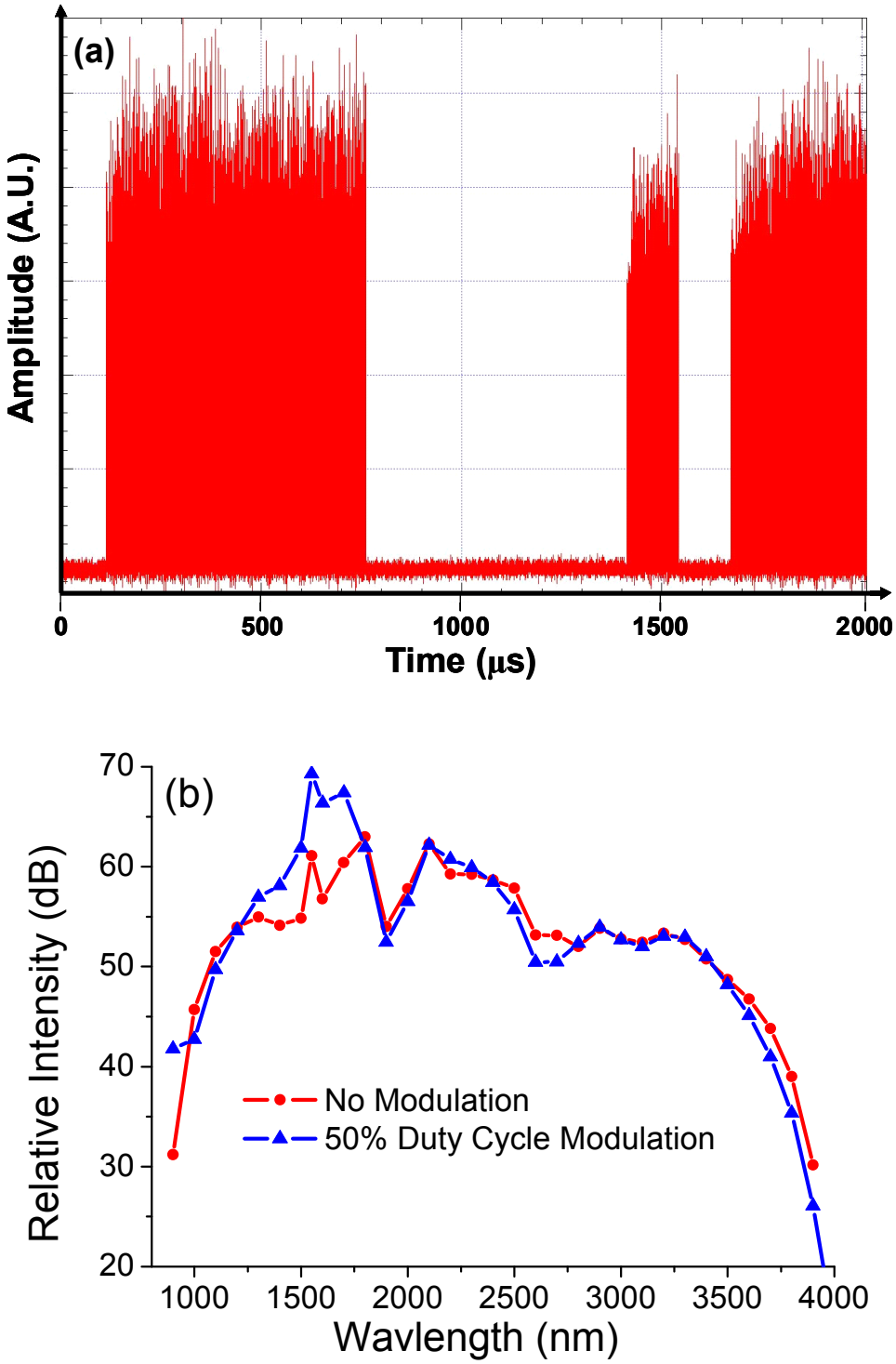

Fig. 5.6 SC modulation experiments. (a) Output pulse modulation pattern. The modulation pattern consists of a 200 pulse burst with a temporal duration of 130 μs, followed by a SC-off time of 130 μs, plus another 1000 pulse burst with a temporal duration of 650 μs, followed by a SC-off time of 650 μs. (b) SC spectral output in modulated and un-modulated modes.

Our SC light source outputs near diffraction-limited beam quality over the entire spectrum. To measure the beam quality of the SC spectrum, the output of the SC is first collimated by a gold-coated parabolic reflective mirror and passes through optical bandpass filters in different bands. The filtered SC light is then focused by a CaF_2 lens and the intensity profile of the laser beam is mapped at difference axial locations around the focal spot by using a knife edge cutting across the beam. We estimate the M^2 value by fitting the beam shape to the Gaussian beam propagation profile. Figure 5.7 demonstrates the M^2 measurement of the SC output beam centered at (a) 1550 nm (~10 nm bandwidth), (b) 2555 nm (~50 nm bandwidth), and (c) 3275 nm (~50 nm bandwidth), all in FL#2. The generated SC spectrum is similar to that of FL#1 with the detailed spectrum analyzed in the following section. As can been seen, all of the wavelengths exhibit near diffraction limited performance with M^2 approaching 1 moving towards the long wavelength region. Such behavior could be attributed to the step-index geometry of the ZBLAN fiber, which is not strictly single spatial mode at wavelengths below the cut-off wavelength (e.g. ~2.7 μm for FL#2). The M^2 value at 3275 nm is ~0.1 higher than that at 2555 nm, which might be due to the uncertainty of the measurement or the different filter bandwidth at these two wavelengths. It should also be noted that the output of the ZBLAN fiber is end-capped with a thin ZBLAN glass slide to prevent the surface damage, which might also reduce the output beam quality of the SC at various wavelengths.

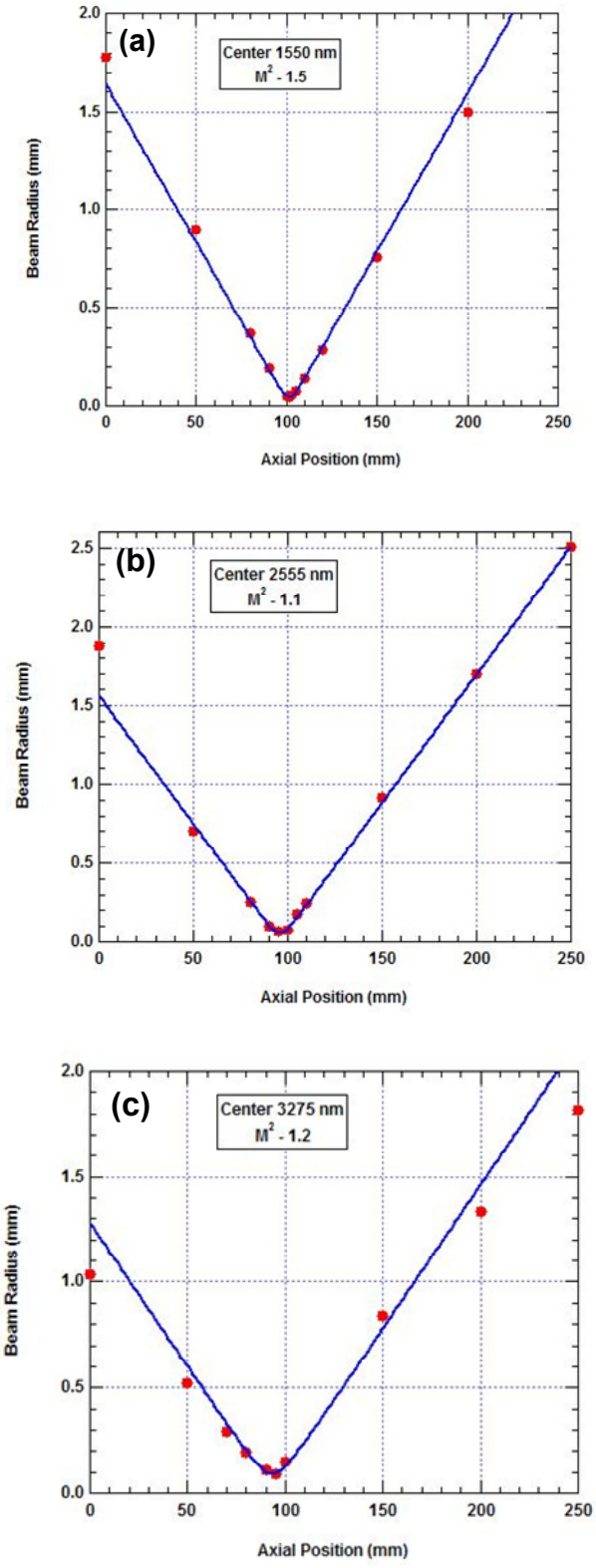

Fig. 5.7 Beam quality M^2 measurement at (a) 1550 nm (b) 2555 nm, and (c) 3275 nm.

5. Power handling limit of the SC generation in ZBLAN fiber

During the experiment, the time-averaged power is limited by the available pump power from the fiber amplifier, and the SC spectral width is limited by the fiber length in combination with fiber bend-induced loss and material loss. We further model the SC generation process to explore the limits of the time-averaged power and spectral bandwidth of the SC in different optical fibers.

The maximum power handling of the optical fiber is limited by the optical material damage. For optical pulses shorter than ~10 ps, the optical damage can be attributed to the multi-photon initiated avalanche ionization of the target glass material as reported in [22]. For optical pulses from ~50 ps to over 100 ns, joule heating of the glass material needs to be taken into consideration [23]. Furthermore, the time-averaged power handling of optical fiber is primarily limited by the heating and melting of the dielectric material, such as catastrophic destruction and fiber fuse damage, which is associated with the fiber glass melting temperature, absorption and heat conductivity [22-25]. Therefore, such damage mechanism puts an upper limit to both the peak power or optical intensity of the laser pulse and the time-averaged power that the optical fiber can handle without incurring any material damage.

We assess the laser-induced optical damage in our SC system in two sub-categories, peak power induced and average power induced optical damage. For the peak power induced optical surface damage, the damage threshold scales inversely proportional to the square root of the pulse width, i.e. $\propto \tau^{-1/2}$, for the pulses with pulse width larger than a few tens of picosecond. For example, the damage threshold has been measured in the fused silica to be ~400 GW/cm^2 with a 10 ps pulse, and 40 GW/cm^2 with a 1 ns pulse at 1053 nm [22]. However, the $\propto \tau^{-1/2}$ dependence does not hold any more for the shorter pulses. Optical

damage of the fiber occurs in a small region around the center of Gaussian distributed incident pulse due to the avalanche ionization. For the fused silica, optical damage at ~11 TW/cm^2 has been observed with a pulse of 140 fs pulse width at 825 nm, i.e. ~1.6 J/cm^2 per pulse. For the fluoride fibers, similar behaviors have been observed. The damage threshold for calcium fluoride is measured to be ~20 GW/cm^2 with a 1 ns pulse (corresponding to 20 J/cm^2 per pulse), and increases to ~5 TW/cm^2 for a 0.4 ps pulse (corresponding to ~2 J/cm^2 per pulse) [22].

Using the reported optical damage threshold for both silica and fluoride materials [22,23], we calculate that the ZBLAN fluoride fiber with an 8.9 μm core diameter can handle >10 kW peak power with 1 ns pulse duration, while the single mode silica fiber can handle >20 kW peak power with the same pulse width. In our experiments, the peak power used in the SC generation is <10 kW for both SMF and ZBLAN fiber, therefore has not yet reached the above limits. In particular, the peak output power is ~6-8 kW in the SMF fiber and 3-5 kW in the ZBLAN fiber, both of which are lower than the projected optical breakdown limit. Although the MI-breakup pulses may possess higher peak power, the shortened pulse width, e.g. ~100-200 fs, increases the optical damage threshold of the fibers. During the operation of our SC laser, we have not observed any peak power induced optical damage at the mechanical splicing point, which includes the output facet of SMF fiber and the input facet of the ZBLAN fiber. Because the optical peak power will be kept at the same level for SC generation with different time-averaged output power, it shall not limit the development of a SC laser source with average output power higher than 10 W.

The average power handling of the optical fiber, on the other hand, is limited by the heat absorption that results in the melting of the fiber glass. The absorption coefficient of the

dielectric glass increases drastically when the glass temperature rises close to the glass transition temperature. The bulk glass material will then heat up, which further increases the material absorption and leads to the melting of the fiber glass and catastrophic fuse damage. Therefore, the maximum average power handling of the fiber under a given experimental condition is limited to the situation when the temperature of the fiber core rises close to its melting point.

Since the fiber cross section is structured as Fig. 5.8, the fiber core temperature can be calculated by the following formula [26],

$$T_{core} = \frac{Q}{2\pi}\left[\frac{\ln\frac{r_{cladding}}{r_{core}}}{k_{cladding}} + \frac{\ln\frac{r_{thermalpad}}{r_{cladding}}}{k_{thermalpad}} + \frac{1}{h_{air} r_{thermalpad}}\right] + T_{air},$$

where r is the radius of the respective subscript, k the thermal conductivity, h the thermal convection coefficient. In addition, Q represents the power dissipation in the SC generation process in the unit fiber length and T the temperature of the respective subscript. The melting temperature of silica glass is 1448 K with a thermal conductivity of 1.38 W/(m·K) [27]. For the fluoride glass, the melting temperature is 528 K with a thermal conductivity of 0.628 W/(m·K) [27,28]. Because the input side of the fiber possesses the highest optical power and bears the most heat dissipation, we estimate the maximum power handling of the optical fiber by calculating the temperature rise of the fiber in the vicinity of the input end for both the SMF and ZBLAN fibers. In particular, ~10% of the power coupled into the ZBLAN fiber is estimated to be dissipated in the first meter length of the fiber, which is confirmed by the numerical simulation of the SC generation [20].

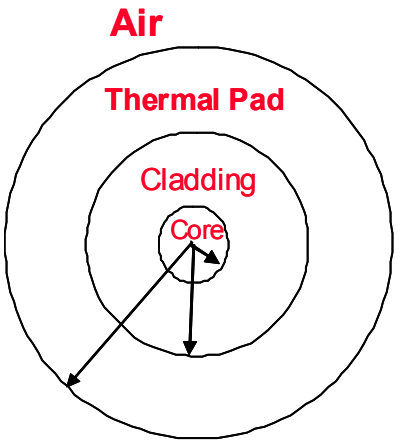

Fig. 5.8 Fiber cross section structure.

To further confirm the validity of our power handling model, we raise the core temperature to the fiber fuse temperature during the SC generation in the silica fiber. The experiments are carried out in the highly-nonlinear (HiNL) silica fibers with an effective mode area of ~10 μm^2 [5]. We couple light of up to ~17 W average power (~6.3 kW peak power and pulse width ~2 ns) with a continuous spectrum from ~1.5-2 μm into a 40 cm length of HiNL fibers. By varying the input pump power and adjusting the corresponding pulse duty cycle, we vary the time-averaged power of the generated SC in the HiNL fiber from ~2.4 W to 15.2 W. We show that the SC average power increases linearly proportionally to the input pump power below the optical damage point as illustrated in Fig. 5.9. When the SC average power is increased to 15.2 W SC average power, we observe a catastrophic backward propagating fiber fuse event starting from the HiNL fiber section after a short period of time. By using the above formula with a unit power dissipation of 10 W/m (i.e. 1 W power dissipated in the first 10 cm length of fiber as estimated by the simulation [5]) due to the high fiber nonlinearity, our model estimates the core temperature close to the input end of the HiNL fiber to be ~1300-1400 K, which is close to the melting temperature of the silica

glass of 1448 K and predicts a fiber fuse event. Hence, the theoretical result is consistent with the experimental observation and our thermal model is able to project the limit of the average power handling of the fiber in SC generation. It should be noted that in the case of SC generation extending close to the intrinsic material absorption edge, the total thermal load in the fiber will be further increased, which will restrain the maximum power handling of the fiber.

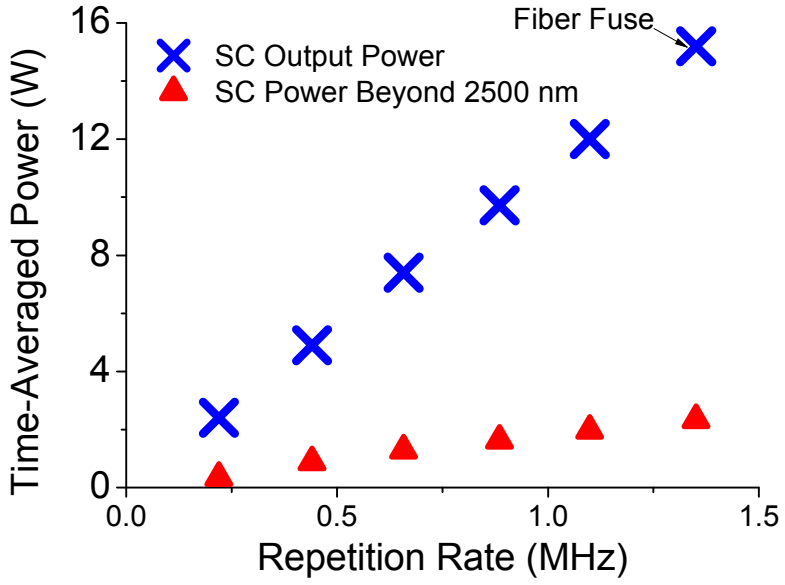

Fig. 5.9 Average SC output power scaling by varying pulse repetition rate and pump power in HiNL fiber. (a) Total SC output power, and (b) SC power beyond 2500 nm. A catastrophic fiber fuse event is observed when SC average power is measured to be 15.2 W.

For the SC generation in the standard ZBLAN fibers without extra thermal management, the maximum average power limit is simulated to be ~15 W with the assumption of 10% power dissipation in the first meter of the fiber as discussed earlier and an air convection coefficient of ~10 W/(m^2·K). In order to further scale up the SC power, better thermal management and heat dissipation techniques need to be implemented to reduce the core temperature of the fiber. One means is to wrap the optical fiber with a thermal pad with high thermal conductivity. As reported by [29], 42.8 W of pump power at 975 nm has been

coupled into an erbium-doped ZBLAN fiber, which is held by an actively water cooled fiber chuck as the heat dissipation means. We propose that by implementing the ZBLAN fiber with a 0.5 mm thick thermal pad of a modest thermal conductivity, e.g. 1 W/(m·K), the maximum power handling can be increased to ~40 W. Therefore, increasing the average power of the SC generation in ZBLAN fibers beyond 10 W is feasible and achievable with sufficient thermal management.

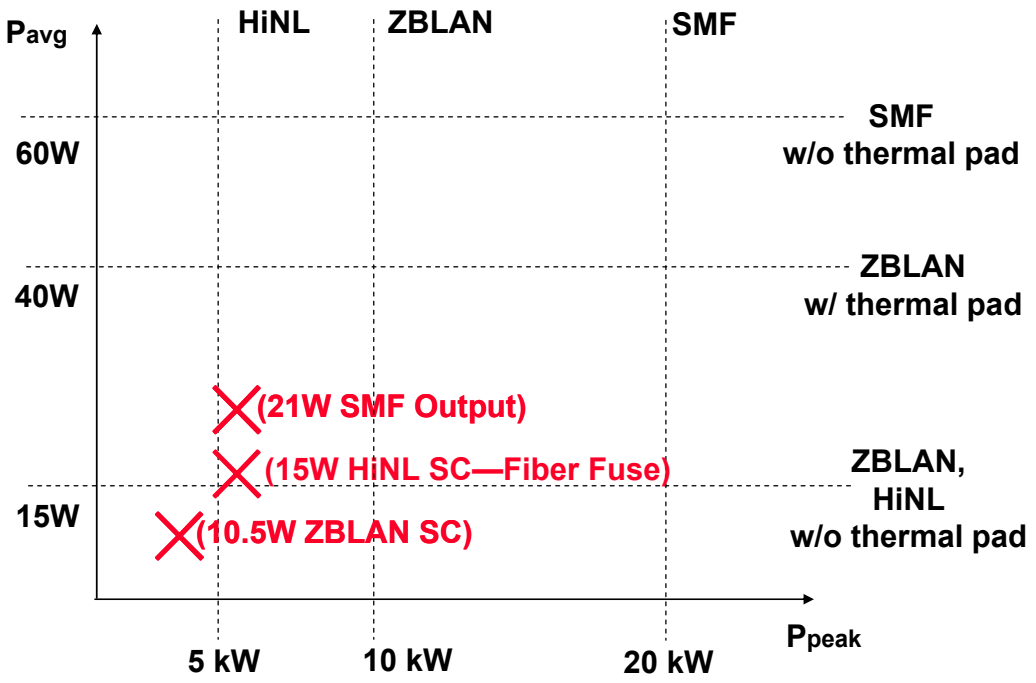

Fig. 5.10 Power handling limits for various fibers. Crossed data points represent the observed experimental data. The respective horizontal and vertical dashed lines of the specified fiber mark the operational boundary of the average and peak optical power.

To summarize the limitations of the power handling of different optical fibers, we plot the boundaries of the optical damage threshold as a function of both the peak power and average power in Fig. 5.10. As can be seen, both the SMF and ZBLAN SC cases reside within the boundaries of their respective peak and average power operating limits and we have not observed any optical damage of the fibers during our experiments. On the other hand, the

HiNL SC operates at a point which exceeds its calculated peak power and average power limits and, therefore, optical damage is expected.

6. Spectral bandwidth limit of the SC generation in ZBLAN fiber

We calculate the long wavelength edges of the SC spectrum in different ZBLAN fibers and match the theoretical results with experiments. Our calculations focus on the determining factors and system parameters that limit the long wavelength edge of SC generation. Therefore, it can provide both an insight to the SC generation process and be used as a design tool for optimizing the SC generation.

Fundamentally, the SC generation is a nonlinear gain/loss process [1]. For the optical gain, there are a number of nonlinear optical interactions, including self-phase modulation (SPM), stimulated Raman scattering (SRS) and parametric four-wave mixing (FWM), present in the SC generation process [30]. Particularly, SPM of the MI-breakup short pulses is responsible for the initial spectral broadening in the SMF and ZBLAN fibers [5]. On the other hand, the Raman scattering assisted soliton self-phase shifting is one of the dominant mechanisms to red shift the SC spectrum and determine the long wavelength edge in the ZBLAN fiber [5,19,20]. Despite the fact that SPM and SRS are different nonlinear processes, both of them are strongly affected by the effective mode area of the fiber, A_{eff} and fiber length [30]. Since nonlinear effects become weaker when the effective mode area increases, the long wavelength edge of the SC is impacted by the change of the A_{eff}. We do not take the pump power into account because we generate our SC in different ZBLAN fibers under similar pump power.

The fiber loss, on the other hand, consists of the intrinsic absorption loss of the fiber material and the bend-induced loss determined by the fiber geometry, both of which are

functions of wavelength. To take the fiber loss into consideration of the nonlinear generation process, we replace the fiber length by the effective interaction length, defined as L_{eff}=[1-exp(-αL)]/α, where α is the fiber loss [30]. For a step-index profile ZBLAN fiber, the effective mode area A_{eff} increases and effective fiber length L_{eff} decreases significantly when the wavelength shifts towards the long wavelength, which reduces the nonlinear effects and will eventually stop the further wavelength shifting in the SC generation. Therefore, we hypothesize that the value of L_{eff}/A_{eff} can be used to project the SC long wavelength edge.

The effect mode area, A_{eff}, is calculated using the common definition of near-field mode effective area, which is [30]

$$A_{\text{eff}} = \frac{\left(\iint |\Psi(x,y)|^2 \, dxdy\right)^2}{\iint |\Psi(x,y)|^4 \, dxdy}.$$

For the fundamental mode LP_{01}, of which the mode distribution is independent of azimuthal angle θ, the formula can be simplified in the cylindrical coordinates, which becomes

$$A_{\text{eff}} = 2\pi \frac{\left(\iint |\Psi(r)|^2 \, rdr\right)^2}{\iint |\Psi(r)|^4 \, rdr},$$

where ψ is the transverse mode function, and the integration is conducted over all space.

We incorporate both the intrinsic material loss and fiber bend-induced loss into the calculation of the effective length, L_{eff}. Material absorption loss is provided by the manufacturer of the ZBLAN fiber [31], which increases significantly towards the long wavelength side. Bend-induced loss is the loss arising from the leakage of the laser transverse mode into the surrounding environment due to the curvature of the fiber. It has

been studied analytically using the Maxwell's Equations [32,33] and can be calculated using the fiber parameters as,

$$2\alpha = \frac{\sqrt{\pi}}{2s} \frac{\left(\frac{u}{V}\right)^2}{\frac{a^2}{2} K_{l-1}(w) K_{l+1}(w)} \frac{a \exp(-\frac{4\Delta w^3}{3aV^2} R)}{w\sqrt{\frac{wR}{a} + \frac{V^2}{2\Delta w}}}.$$

The descriptions of the fiber parameters are listed in Table 5.1.

Parameters	**Description**
α	amplitude loss factor
a	fiber core radius
$\Delta = \frac{n_{core} - n_{clad}}{n_{clad}}$	relative difference of refractive indices of the fiber core and cladding
R	radius curvature of the bended fiber
$V = k_0 a \sqrt{n_{core}^2 - n_{clad}^2}$	normalized frequency
u	$u = a\sqrt{n_{core}^2 k_0^2 - \beta^2}$
w	$w = a\sqrt{\beta^2 - n_{clad}^2 k_0^2}$
l	transverse mode index
$K_{l-1}(w)$, $K_{l+1}(w)$	second kind of Bessel functions of the order $l-1$ and $l+1$ respectively
s	degeneracy factor

Table 5.1 Fiber parameters for bend-induced loss calculation.

The radius curvature of the bended fiber is set to 40 cm in the simulation to match the experimental condition. Since we only consider fundamental mode LP_{11} in the fiber, both $K_{l-1}(w)$ and $K_{l+1}(w)$ degenerates to $K_1(w)$. The degeneracy factor is set to be 2 for the LP_{11} mode. The theoretical results of the bend-induced loss and material loss are then used to calculate the effective length.

We calculate the values of the effective mode area and effective fiber length in five

ZBLAN fibers with different fiber design. The fiber characteristics of the ZBLAN fibers and the experimental SC long wavelength edge defined as the 30 dB intensity drop from the flat part of the continuum are listed in Table 5.2. All five fibers are made of the same materials and, thus, possess the same material loss properties and fiber nonlinearities n_2. The wavelength dependence of the effective mode area and bend-induced loss of each fiber varies dramatically due to the difference in the fiber designs, as analyzed in the following paragraphs.

Fiber #	Core Diameter	Cladding Diameter	Numerical Aperture	Length	SC Long Wavelength Edge
FL#1	8.9μm	125μm	0.21	7m	3.9μm
FL#2	10.6μm	125μm	0.20	15m	4.1μm
FL#3	5.7μm	125μm	0.16	15m	3.0μm
FL#4	8.6μm	125μm	0.17	8m	3.5μm
FL#5	7.0μm	125μm	0.30	8m	4.3μm

Table 5.2 ZBLAN fiber characteristics.

The calculated effective mode area A_{eff}, bend-induced loss, and effective length L_{eff} are illustrated in Fig. 5.11. As can be seen, the wavelength evolution of the calculated parameters has shown great disparities between different ZBLAN fibers due to their fiber designs. The mode field diameter and bend-induced loss increases most significantly in FL#3, which has the smallest core size and NA in all fibers. More specifically, the mode field area increases from ~37 μm^2 at 1.5 μm to over 1000 μm^2 at 4.5 μm, which leads to the dramatic increase of the bend-induced loss and plummeting of the effective length in the long wavelength regime (Fig. 5.11). Hence, the SC generation in the mid-IR regime is turned off. On the other hand, FL#5 has the tightest optical mode confinement that is manifested in the minimal change of the effective areas as the wavelength shifts towards the mid-IR. As a result, FL#5 demonstrates negligible bend-induced loss and has an effective length that is closer to its

actual fiber length over a wide wavelength range. It should be noted that the bend-induced loss formula assumes infinite cladding size and does not take micro-bending of the optical fiber into account. Therefore, the actual fiber bend-induced loss is affected by the fiber fabrication process and may be higher than the theoretical value. FL#1 and FL#2, which are tested in the previous sections, have modest mode confinement, which is capable of guiding the mid-IR wavelength and supporting nonlinear wavelength generation to ~4 μm.

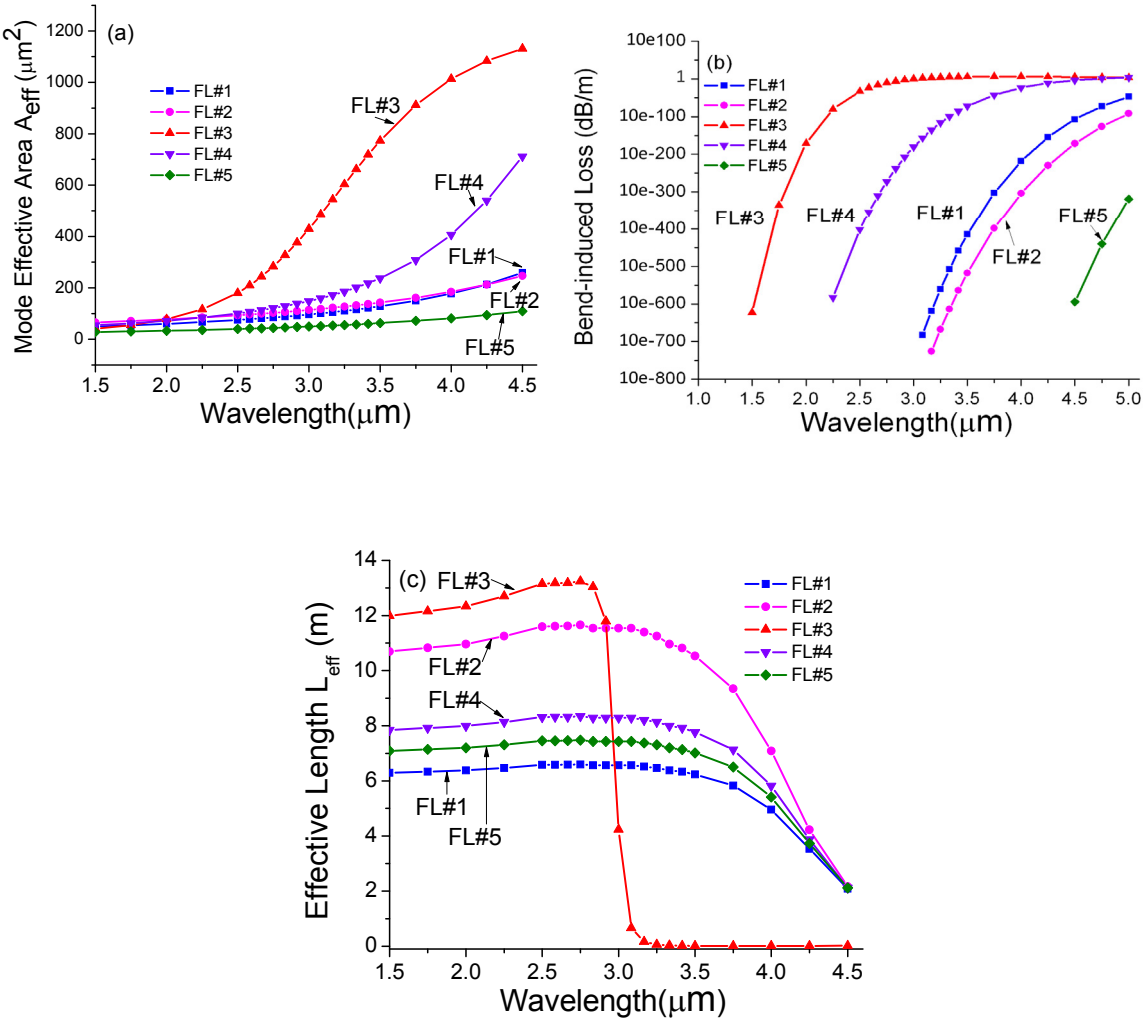

Fig. 5.11 Theoretical calculation. (a) Effective mode area A_{eff}, (b) bend-induced loss, and (c) effective length L_{eff} in five ZBLAN fibers (FL#1-FL#5) with different fiber designs.

The theoretical values of L_{eff}/A_{eff} are plotted in comparison with the experimental SC spectrum long wavelength edges in Fig. 5.12. The SC long wavelength edge is defined as the 30 dB amplitude drop from the flat part of the continuum. Therefore, the experimental SC long wavelength edge is ~3.9 μm, ~4.1 μm, ~3.0 μm, ~3.5 μm, and ~4.3 μm for FL#1-FL#5 respectively as illustrated in Fig. 5.12a. It should be noted that the SC average power generated in different ZBLAN fibers in Fig. 5.12a varies from ~20 mW to over ~10.5 W due to the different pump laser systems. We have achieved >60% coupling efficiency from SMF to FL#1 and FL#2 and ~50% coupling efficiency for FL#5 due to the large mode mismatch. The calculated L_{eff}/A_{eff} demonstrates the same wavelength evolution trend as the experiments. In particular, FL#3 has an L_{eff}/A_{eff} value drop below 0.03 m/μm^2 around ~2.9-3 μm, while L_{eff}/A_{eff} of FL#5 reaches the same value in the 4.3-4.4 μm region. Therefore, we fit the theoretical data with the experimental results and find out that the SC generation cuts off when the value of L_{eff}/A_{eff} reduces to ~0.03 m/μm^2. The Raman amplification factor can be approximated by $G_A=g_R P L_{eff}/A_{eff}$, where g_R is the Raman gain coefficient and P is the pump peak power. We calculate G_A to be ~10 assuming P=5 kW, g_R=6.4×10^{-14}m/W [20], and L_{eff}/A_{eff} = 0.03 m/μm^2, which is close to the Raman threshold [30]. Therefore, the value of L_{eff}/A_{eff} can be used as a figure of merit to predict the SC long wavelength edge. Figure 5.12c illustrates the theoretical SC edge set by the L_{eff}/A_{eff} fitting value versus the experimental results. We notice that, for each pair of theoretical prediction and experimental observation, the SC long wavelength edge disparity is within 50 nm, which confirms the validity of our hypothesis and theoretical model.

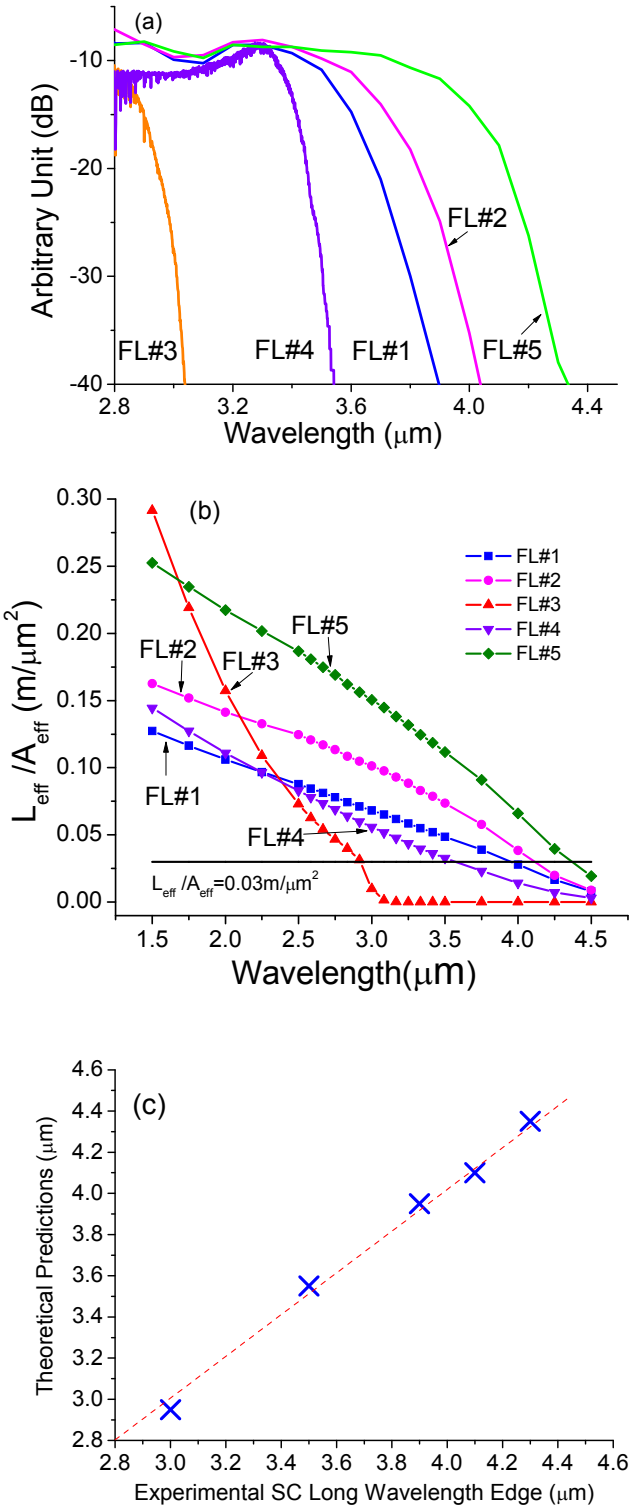

Fig. 5.12 Experimental and theoretical results in FL#1-FL#5. (a) Generated SC spectrum in the long wavelength side, (b) theoretical calculation of L_{eff}/A_{eff}, and (c) theoretical prediction of SC long wavelength edge versus experimental data (dashed line represents the 45-degree angle fitting line).

The most significant factor that limits the long wavelength side growth of the SC spectrum varies between different fiber designs. We observe that the bend-induced loss in conjunction with the diminished nonlinear gain associated with the enlargement of the effective area limits the SC spectrum in FL#3 and FL#4. For the fibers we used in the previous section, FL#1 and FL#2, nonlinear optical gain and fiber material loss play important roles to determine the SC long wavelength edge. In particular, FL#1 has a shorter SC cut-off wavelength than that of FL#2 primarily due to the short fiber length even though these two fibers have similar mode effective area and bend-induced loss. On the other hand, for the SC generation in FL#5, the intrinsic material absorption of the fluoride glass clamps the SC generation to ~4.5 μm.

Our calculation can be used to predict an optimal ZBLAN fiber design to extend the SC long wavelength edge as far as possible. As demonstrated in our calculation, one of the most effective approaches is to employ a ZBLAN fiber with a large NA as well as a reasonably small core size, which can lead to a tighter confinement of the optical mode in the core region. Hence, not only the nonlinear wavelength generation process can be enhanced due to a smaller effective mode area, but the bend-induced loss will also be mitigated thanks to the reduced leakage of the more tightly confined optical mode. Therefore, we propose to generate the SC in a ZBLAN fiber with an NA of 0.30 and core diameter of 7 μm to extend the SC long wavelength edge to ~4.5 μm.

7. Discussion and conclusion

The all-fiber-integrated configuration improves the mechanical stability and the power efficiency of our SC light source. In the previous high power SC experiments [20], we have used an erbium/ytterbium co-doped cladding-pumped fiber laser with bulk optical coupling

between different stages of the amplifier. The power efficiency from the pump diodes to the output in the SMF is ~14%. In comparison, by splicing the amplifier stage together and removing the bulk optics, the pump-to-output efficiency is more than doubled to ~30%. Under normal operation, the pump diode wall-plug electrical-to-optical efficiency is about 50% and the pump-to-SC conversion efficiency is ~50% as discussed earlier. Therefore, the wall-plug electricity-to-SC power efficiency, defined as the ratio of the generated SC average power out of the total electrical power consumption is improved to >7% for our SC light source from <3% for the table-top system. To further improve the overall power efficiency of the system, the coupling efficiency of the mechanical splice needs to be increased, e.g. adding an intermediate fiber to better match the mode profile of the SMF and ZBLAN fibers. Moreover, the pump diodes of the last stage power amplifiers can be turned off during the long SC-off period in the modulated scenario to save the wall-plug electricity consumption.

Our SC light source is scalable in the time-averaged power up to 10.5 W by changing the pulse repetition rate. We show in Fig. 5.4 that the SC average power can be continuously varied by a factor of 7.5, i.e. from 1.4 W to 10.5 W, by increasing the pulse repetition rate by the same scale from 0.42 MHz to 3.33 MHz and increasing the pump power supply correspondingly. The power scalability is enabled by using the amplified laser diode pulses as the pump source for the SC generation. Compared to the conventional mode-locked lasers, our SC laser has a greater flexibility in the system configuration from the mature telecommunication technology and has potential scalability in the output power by adding more pump laser diodes.

In our experiments, the output time-averaged power is currently limited by the available pump power diodes coupled to the fiber amplifier. As a rule-of-thumb, one 8 W pump diode

contributes ~1 W average power to the SC generation. Therefore, we use twelve 8 W pump diodes in our pump system to generate the SC with ~10.5 W output power. To further scale up the SC average power, more pump diodes need to be used to feed the fiber amplifier to generate a higher pump power. On the other hand, the SC long wavelength edge is limited by the fiber nonlinearities, bend-induced loss and fluoride material absorption. By using a ZBLAN fiber with step-index geometric design and fiber length, the SC spectral bandwidth can be pushed to the limit set by the ZBLAN material loss at ~4.5 μm. Novel fiber geometry, e.g. photonic crystal fiber structure, could be used to better confine the optical mode area in the mid-IR in the future. To further extend the SC long wavelength edge, new infrared optical fiber, such as tellurite fiber, needs to be used. For example, SC generation extending to ~5 μm is demonstrated in a tellurite fiber with photonic crystal structure [16].

In summary, mid-IR SC with 10.5 W time-averaged power and a continuous spectrum of ~0.8-4 μm is generated in ZBLAN fibers by amplified nanosecond diode pulses. The average output power of the SC is linearly scalable from 1.4 W to 10.5 W while maintaining the similar spectra by varying input pump power and the corresponding pulse duty cycle. We demonstrate modulation of the SC output pulse at 50% duty cycle with 1.5 kHz and 7.7 kHz modulation speed by directly modulating the seed laser diode and controlling the amplifier gain. For the 10.5 W SC system, the long wavelength edge at 4 μm is limited by the fiber length in combination with material absorption loss and bend-induced loss. By using a ZBLAN fiber with 0.3 NA and a core size of 7 μm, the SC long wavelength edge can be further extended to ~4.5 μm due to the minimized bend-induced loss and better confined effective mode area. We also simulate that time-averaged power of ~15 W can be withheld in the standard ZBLAN fiber, and up to ~40 W can be supported in the ZBLAN fiber with

appropriate thermal management.

Substantial contents in this chapter are to be published as: C. Xia, Z. Xu, M. N. Islam, F. L. Terry, Jr., M. J. Freeman, A. Zakel, and J. Mauricio, “10.5 W time-averaged power mid-IR supercontinuum generation extending beyond 4 μm with direct pulse pattern modulation,” IEEE J. Sel. Top. Quantum Electron. (2009).

References

[1] R. R. Alfano, The supercontinuum laser source: fundamentals with updated references, 2nd ed. (Springer, New York, 2006).

[2] T. Morioka, K. Mori, S. Kawanishi, and M. Saruwatari, “Multi-WDM-channel, GBit/s pulse generation from a single laser source utilizing LD-pumped supercontinuum in optical fibers,” IEEE Photon. Technol. Lett. **6**, 365-368 (1994).

[3] H. Takara, “Multiple optical carrier generation from a supercontinuum source,” Opt. Photon. News **13**, No. 3 48-51 (2002).

[4] F. G. Omenetto, N. A. Wolchover, M. R. Wehner, M. Ross, A. Efimov, A. J. Taylor, V. V. R .K. Kumar, A. K. George, J .C. Knight, N. Y. Joly, and P. St. J. Russell, “Spectrally smooth supercontinuum from 350 nm to 3 μm in sub-centimeter lengths of soft-glass photonic crystal fibers,” Opt. Express **14**, 4928-4934 (2006).

[5] C. Xia, M. Kumar, M. Y. Cheng, O.P. Kulkarni, M. N. Islam, A. Galvanauskas, F. L. Terry, M. J. Freeman, D. A. Nolan, and W. A. Wood, "Supercontinuum Generation in Silica Fibers by Amplified Nanosecond Laser Diode Pulses," IEEE J. Sel. Top. Quantum Electron. **13**, 789-797 (2007).

[6] T. Izawa, N. Shibata, and A. Takeda, “Optical attenuation in pure and doped fused silica in their wavelength region,” Appl. Phys. Lett. **31**, 33-35 (1977).

[7] J. C. Travers, A. B. Rulkov, B. A. Cumberland, S. V. Popov, and J. R. Taylor, "Visible supercontinuum generation in photonic crystal fibers with a 400W continuous wave fiber laser," Opt. Express **16**, 14435-14447 (2008).

[8] I. T. Sorokina and K. L. Vodopyanov, eds., *Solid-State Mid-Infrared Laser Sources*, (Springer-Verlag, Berlin Heidelberg, 2003).

[9] M. Razeghi, S. Slivken, Y. Bai, and S. R. Darvish, “The quantum cascade laser: a versatile and powerful tool,” Opt. Photon. News **19**, No. 7 42-47 (2008).

[10] K. Wille, “Synchrotron radiation sources,” Rep. Prog. Phys. **54**, 1005-1067 (1991).

[11] G. S. Edwards, R. H. Austin, F. E. Carroll, M. L. Copeland, M. E. Couprie, W. E. Gabella, R. F. Haglund, B. A. Hooper, M. S. Hutson, E. D. Jansen, K. M. Joos, D. P. Kiehart, I. Lindau, J. Miao, H. S. Pratisto, J. H. Shen, Y. Tokutake, A. F. G. van der Meer, and A. Xie, “Free-electron-laser-based biophysical and biomedical instrumentation,” Rev. Sci. Instrum. **74**, 3207-3245 (2003).

[12] R. R. Anderson, W. Farinelli, H. Laubach, D. Manstein, A. N. Yaroslavsky, J. Gubeli, K. Jordan, G. R. Neil, M. Shinn, W. Chandler, G. P. Williams, S. V. Benson, D. R. Douglas, H. F. Dylla, “Selective photothermolysis of lipid-rich tissues: A free electron laser study,” Lasers Surg. Med. **38**, 913-919 (2006).

[13] J. Mandon, E. Sorokin, I. T. Sorokina, G. Guelachvili, and N. Picqué, "Supercontinua for high-resolution absorption multiplex infrared spectroscopy," Opt. Lett. **33**, 285-287 (2008).

[14] S. A. Diddams, D. J. Jones, J. Ye, S. T. Cundiff, J. L. Hall, J. K. Ranka, R. S.Windeler, R. Holzwarth, T. Udem, and T.W. Hänsch, “Direct link between microwave and optical frequencies with a 300 THz femtosecond laser comb,” Phys. Rev. Lett. **84**, 5102–5104 (2000).

[15] C. L. Hagen, J. W. Walewski, and S. T. Sanders, “Generation of a continuum extending to the midinfrared by pumping ZBLAN fiber with an ultrafast 1550-nm source,” IEEE Photon. Technol. Lett. **18**, 91-93 (2006).

[16] P. Domachuk, N. A. Wolchover, M. Cronin-Golomb, A. Wang, A. K. George, C. M. B. Cordeiro, J. C. Knight, and F. G. Omenetto, "Over 4000 nm bandwidth of mid-IR supercontinuum generation in sub-centimeter segments of highly nonlinear tellurite PCFs," Opt. Express **16**, 7161-7168 (2008).
[17] O. P. Kulkarni, C. Xia, D. J. Lee, M. Kumar, A. Kuditcher, M. N. Islam, F. L. Terry, M. J. Freeman, B. G. Aitken, S. C. Currie, J. E. McCarthy, M. L. Powley, and D. A. Nolan, "Third order cascaded Raman wavelength shifting in chalcogenide fibers and determination of Raman gain coefficient," Opt. Express **14**, 7924-7930 (2006).
[18] J. S. Sanghera, L. B. Shaw, C. M. Florea, P. Pureza, V. Q. Nguyen, D. Gibson, F. Kung, and I. D. Aggarwal, "Non-linearity in chalcogenide glasses and fibers, and their applications," presented at Quantum Electronics and Laser Science Conference QELS 2008, San Jose, Calif., May 4-9, 2008, QTuL5.
[19] C. Xia, M. Kumar, O. P. Kulkarni, M. N. Islam, F. L. Terry, Jr., M. J. Freeman, M. Poulain, and G. Mazé, "Mid-infrared supercontinuum generation to 4.5 μm in ZBLAN fluoride fibers by nanosecond diode pumping," Opt. Lett. **31**, 2553-2555 (2006).
[20] C. Xia, M. Kumar, M. -Y. Cheng, R. S. Hegde, M. N. Islam, A. Galvanauskas, H. G. Winful, F. L. Terry, Jr., M. J. Freeman, M. Poulain, and G. Mazé, "Power scalable mid-infrared supercontinuum generation in ZBLAN fluoride fibers with up to 1.3 watts time-averaged power," Opt. Express **15**, 865-871 (2007).
[21] G. Canat, J. Mollier, J. Bouzinac, G. M. Williams, B. Cole, L. Goldberg, Y. Jaouën, and G. Kulcsar, "Dynamics of high-power erbium–ytterbium fiber amplifiers," J. Opt. Soc. Am. B **22**, 2308-2318 (2005).
[22] B. C. Stuart, M. D. Feit, S. Herman, A. M. Rubenchik, B. W. Shore, and M. D. Perry, "Optical ablation by high-power short-pulse lasers," J. Opt. Soc. Am. B **13**, 459-468 (1996).
[23] B. C. Stuart, M. D. Feit, S. Herman, A. M. Rubenchik, B. W. Shore, and M. D. Perry, "Nanosecond-to-femtosecond laser-induced breakdown in dielectrics," Phys. Rev. B **53**, 1749-1761 (1996).
[24] S. I. Yakovlenko, "Physical Processes upon the Optical Discharge Propagation in Optical Fiber," Laser Phys. **16**, 1273-1290 (2006).
[25] E. M. Dianov, I. A. Bufetov, A. A. Frolov, V. M. Mashinsky, V. G. Plotnichenko, M. F. Churbanov, and G. E. Snopatin, "Catastrophic destruction of fluoride and chalcogenide optical fibres," Electron. Lett. **38**, 783-784 (2002).
[26] E. Sonntag, C. Borgnakke, and G. J. Van Wylen, *Fundamentals of Thermodynamics*, (John Wiley Publishers, 1998).
[27] J. M. Parker, "Fluoride glasses," Annu. Rev. Mater. Sci. **19**, 21-41 (1989).
[28] J. A. Harrington, "Infrared Fibers," in *Handbook of Optics Vol. 3, Classical, Vision & X-ray Optics*, M. Bass, J. M. Enoch, E. W. Van Striland, and W. L. Wolfe, eds.(Optical Society of America, Washington DC, 2002), pp. 14.1 - 14.16.
[29] X. Zhu and R. Jain, "10-W-level diode-pumped compact 2.78 μm ZBLAN fiber laser," Opt. Lett. **32**, 26-28 (2007).
[30] G. P. Agrawal, *Nonlinear Fiber Optics,* 3rd edition, (Academic, San Diego, 2001).
[31] "Fluoride fiber SMFF," http://www.fiberlabs.co.jp/fiber_smff(E).htm.
[32] J. -I. Sakai, T. Kimura, "Bending loss of propagation modes in arbitrary index profile optical fibers," Appl. Opt. **17**, 1499-1506 (1978).

[33] D. Marcuse, “Curvature loss formula for optical fibers,” J. Opt. Soc. Am. **66**, 216-220 (1976).

Chapter VI

Mid-Infrared Absorption Spectroscopy and Selective Ablation *in vitro* between Lipids and Proteins by Using a Supercontinuum Laser

1. Introduction

In the mid-infrared (mid-IR) region between 2.6-3.8 μm, lipids and proteins have fundamental absorptions that lie at different wavelengths. For the first time to our knowledge, using an all-fiber-integrated supercontinuum (SC) laser, we measure the mid-IR spectral characteristics of biological samples. We acquire the absorption spectra of biological samples, including the constituents of the normal artery and atherosclerotic plaque (AP), in the 2.6-3.8 μm wavelength window. We observe distinct spectral signatures in 2.8-3.2 μm corresponding to protein and water absorption and in 3.2-3.6 μm that are associated with fatty acids and cholesterol esters. We perform selective ablation of lipid-rich tissues by targeting light in the C-H absorption band. Selective ablation is possible because proteins show primary light absorption at 2.8-3.2 μm due to N-H and O-H bonds, while lipids exhibit absorptions in 3.2-3.6 μm associated with C-H stretching vibrations. Based on the spectral differentiation, we demonstrate that lipid-rich samples, e.g. adipose tissue, can be selectively ablated without causing damage to normal artery by using a light radiance as low as ~15 mJ/mm^2 in the 3.2-3.6 μm band. Our experiments employ a novel SC laser that provides a continuous spectrum coverage ranging from ~0.8 to 4.2 μm with time-averaged power scalable up to

10.5 W.

The fiber based SC laser source provides a new platform for absorption spectroscopy and tissue ablation in the mid-IR. Optical absorption spectroscopy has been widely used to provide the chemical information of biological samples since every molecular vibrational bond resonates at a unique optical frequency [1,2]. Conventionally, thermal lamps, optical parametric amplifiers [3], broadband femtosecond lasers [4], quantum cascaded lasers [5] and synchrotron lasers [2] are used as the light sources for mid-IR spectroscopic applications. Recently, optical absorption spectroscopy has been reported using SC laser systems in the visible and near infrared (near-IR) wavelength regime. For example, C_2H_2 and NH_3 overtone spectra in the 1.5-1.7 μm region are measured using SC generated in a soft-glass photonic crystal fiber [6]. In addition, various spectral acquisition techniques, including FTIR [6], cavity enhanced absorption spectroscopy [7], and time domain dispersive frequency mapping [8], have been demonstrated to improve the spectral resolution, measurement speed, and signal sensitivity. However, SC based absorption spectroscopy experiments in the mid-IR where the fundamental molecular vibrational modes reside have not yet been reported. In this paper, we demonstrate mid-IR absorption spectroscopy measurements using an all-fiber-integrated SC laser, which has no moving parts, generates the entire spectrum simultaneously in the single spatial mode and operates under room temperature.

Our SC fiber laser can also selectively ablate lipid-rich samples by targeting the laser light in the 3.2-3.6 μm fatty acids and cholesterol esters absorption band. While precision ablation using nonlinear optical breakdown has been demonstrated using free electron lasers [9] and femtosecond lasers [10], the process is spatially selective but not tissue specific. Single wavelength-dependent selective ablation comparing 2.77 μm to 6.45 μm has been

performed in collagen for mid-IR laser ablation of cornea [11] and 5.75 μm to 6.1 μm for ablation of cholesterol esters using free-electron laser [12]. Selective ablation of lipid-rich tissue has been also reported by preferentially heating the target fatty tissues above the physiological temperature using lipid absorption bands at 1.21 and 1.72 μm [13]. We show here ablations of lipid-rich adipose tissues under conditions that do not damage the normal artery wall in blood vessels. Hence, our SC laser, packaged into a 2U rack unit (19 inches in width/21 inches in depth/4 inches in height), could potentially be deployed in the clinical environment for practical medical use.

2. Experimental setup and sample preparation

The experimental setup comprises three parts—the SC laser, mid-IR spectroscopy, and laser ablation. The SC laser consists of a 1542 nm distributed feedback (DFB) laser diode, multi-stage fiber amplifiers, and SC generation fibers as illustrated in Fig. 6.1. The DFB laser outputs seed light with ~0.5 ns pulse width at variable pulse repetition rate. The light is amplified by three stages of fiber amplifiers, in which the first stage is a single mode erbium-doped fiber amplifier and second and third stages are cladding-pumped erbium/ytterbium co-doped fiber amplifiers. Narrow bandpass filters and optical isolators are used in between each amplifier stage to filter out the out-of-band amplified spontaneous emission and minimize back-reflection. The amplified diode pulses are then coupled into a combination of ~2 m length of standard single mode fiber (SMF) followed by ~7 m length of ZBLAN (ZrF_4-BaF_2-LaF_3-AlF_3-NaF) fluoride fiber to generate the SC. The ZBLAN fiber has a core diameter of 8.9 μm, a cladding diameter of 125 μm, and a numerical aperture of 0.20. The output light from the SMF fiber is coupled into the ZBLAN fiber through a mechanical splice.

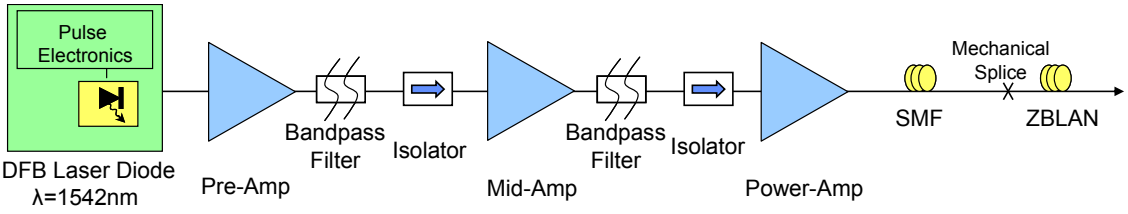

Fig. 6.1 SC laser setup comprising a DFB laser diode followed by three stages of fiber amplifiers plus SC generation fibers.

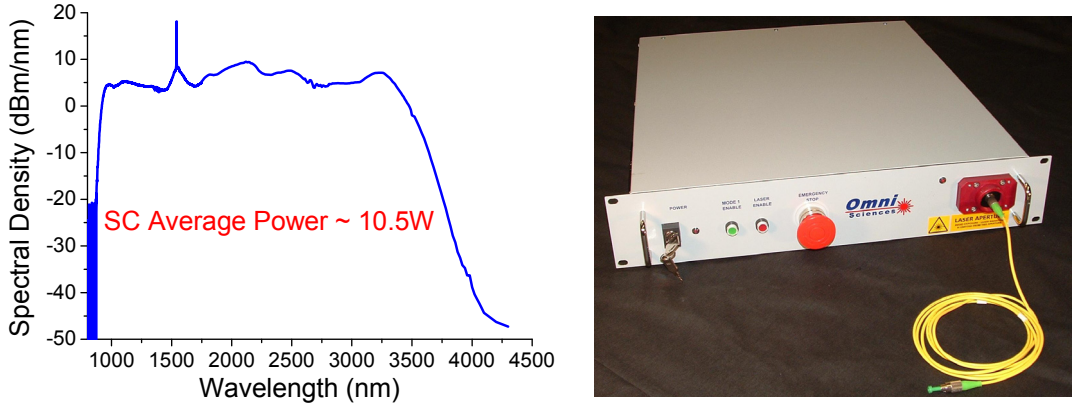

Fig. 6.2 (a) SC spectrum generated in 2 m length of single mode fibers plus 7 m length of ZBLAN fibers (left), and (b) illustration of 2.5 W mid-IR SC laser prototype (inside follows the block diagram of Fig. 6.1) (right).

As illustrated in Fig. 6.2a, the SC laser provides a spectrum coverage extending from ~0.8 μm to 4 μm with a time-averaged output power scalable up to 10.5 W. All of the spectral components of the SC output are generated simultaneously and in single spatial mode. It should be noted that although the SC laser has been demonstrated with up to 10.5 W average output power, the spectroscopy measurements and laser ablation are conducted with only a few of the pump laser diodes on and ~1.5 W SC output power. Further details of the SC laser are described in [14]. Also, to illustrate that our SC laser can be made compact for potential clinical applications, Fig. 6.2b shows a picture of a 2.5 W output power prototype laser corresponding to the optical block diagram of Fig. 6.1. This is a 2U rack unit (19 inches in width/21 inches in depth/4 inches in height) that plugs into the wall and has a serial port for computer controlled laser pulse pattern modulation.

For absorption spectrum measurements, the output of the SC laser is coupled to the mid-IR spectroscopy setup shown in Fig. 6.3a. We use a parabolic off-axis mirror to collimate the SC light and to minimize the chromatic aberration. To improve the signal-to-noise ratio of the measurements, a 50/50 CaF_2 based beam splitter splits the collimated SC output into two beams, i.e. one signal arm and one reference arm, which are modulated by optical choppers at different frequencies. The light of the signal arm is focused by a 25.4 mm focal length CaF_2 lens onto the sample placed on a mid-IR reflective substrate, e.g. gold coated slide or MirrIR microscope slide (Kevley Technologies, Chesterland, OH). The reflected light is then re-collimated by the same lens and recombined with the reference arm by another 50/50 beam splitter. The recombined SC light is coupled into a grating-based spectrometer with signal collected by a liquid-nitrogen cooled InSb detector. A 2500 nm long pass filter is placed in the optical path to remove the higher-order diffractions of the SC spectrum in the spectrometer, and optical apertures are used to obtain the optimal signal strength for both arms. The signal from the detector is acquired by two lock-in amplifiers with each synchronized to its respective optical chopper. The amplitude fluctuation of the SC laser is compensated for by taking the ratio of the two arms. Therefore, the mid-IR spectroscopy system is able to detect a change of the SC spectral amplitude within less than 1%.

For the selective ablation experiment, the SC laser is used in conjunction with the ablation set-up of Fig. 6.3b. The SC light residing in the lipids vibrational bands is selected out by a ~3200 nm long pass filter. For the ablation experiments, the laser pulse width is set to 1 ns and the shape of the SC spectrum is maintained for different power levels. The collimated SC beam diameter is estimated to be ~9 mm. The filtered light is then focused by

a 25.4 mm CaF_2 lens to a spot size of ~3 mm onto the sample. Substrates holding thin samples are made of mid-IR transparent materials, e.g. CaF_2 or KCl window (International Crystal Laboratories, Garfield, NJ), to reduce the substrate-absorption induced heating effects.

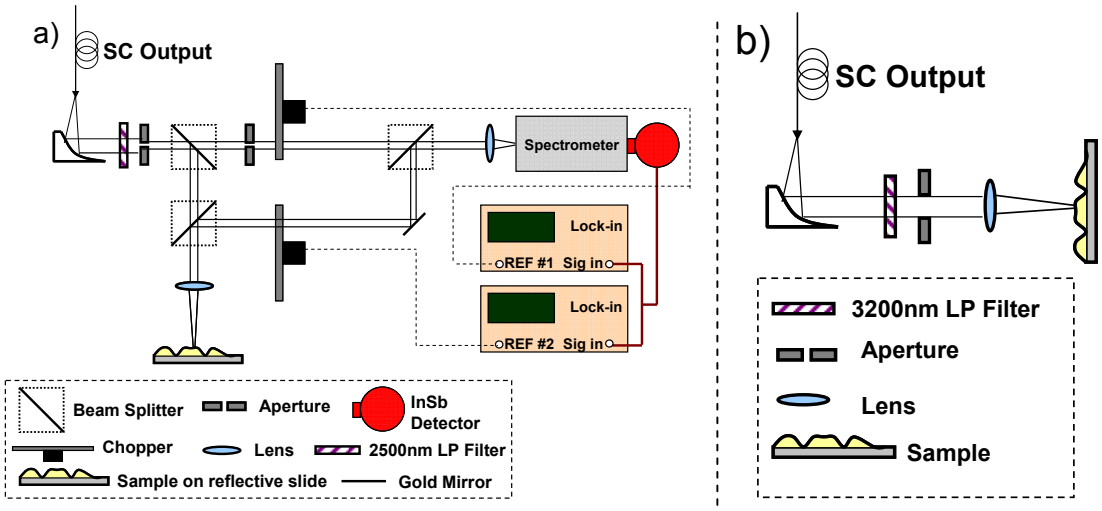

Fig. 6.3 Experimental setup. (a) Reflection-absorption spectra measurement, and (b) selective laser ablation.

SC based spectroscopy experiments were performed *in vitro* on cultured cells and dried egg yolk powder (Sigma-Aldrich, Milwaukee, WI). Cells were grown using the following methodology. Endothelial cells and smooth muscle cells were cultured for 24 hours in RPMI medium containing antibiotics (streptomycin and pencillin, Gibco) and 10% fetal bovine serum. Murine macrophages (cell line J774A.1) were plated onto 2.5 cm square pieces of MirrIR microscope slides (Kevley Technologies). To improve adherence of the cells to the glass slide substrate, the glass had been previously incubated for 20 minutes in a 100µg/ml solution of poly-L-lysine (Sigma Chem., #P-1399) in sterile water. The poly-L-lysine solution was removed and the glass was air dried for 2 hours. Sterility of the glass substrates was achieved by exposing each side of the glass to a germicidal UV lamp for 20 minutes. Macrophages were then plated onto the glass substrates at high cell density to achieve total

coverage of the substrate by the cells. Macrophages were cultured for 24 hours in RPMI medium containing antibiotics (streptomycin and pencillin, Gibco) and 10% fetal bovine serum. Macrophages were then activated by treatment with 1 μg/ml lipopolysaccharide (LPS from *Salmonella minnesota* R595, Axxora, San Diego, CA) for 24 hours. At this point, macrophages were treated with the cholesterol/PC liposomes for 48 hours, and then the cells were used for experiments.

Liposomes were made as described in the following paragraph. 25 mg each of cholesterol (Sigma-Aldrich, Milwaukee, WI) and egg phosphatidylcholine (PC, Sigma-Aldrich) were dissolved in 1 ml of chloroform in a 15 x 125 mm glass tube. The chloroform was evaporated leaving the cholesterol/PC as a residue on the surface of the glass tube. 7 ml of RPMI 1640 culture medium (Invitrogen/Gibco, Carlsbad, CA) containing 10 % fetal calf serum (Invitrogen/Gibco) was added to the tube and liposomes were made by sonicating the cholesterol/PC mixture in the culture medium using a Tekmar TM40 sonic disruptor set to maximum output for one minute. This suspension was then passed through a 0.45 micrometer pore size sterile filter.

To observe lipids within foam cells, cells were prepared in a manner similar to that described by Kinkel et al [15]. Cells were fixed with 4% formaldehyde solution for 1 hour, rinsed in phosphate buffered saline and then rinsed with 2 changes of ethylene glycol for 2 minutes each. Cells were then incubated in a solution of oil red O in ethylene glycol for 20 minutes, rinsed twice for 5 minutes each in ethylene glycol and then rinsed in water. Macrophages exhibited no oil red O staining droplets while LPS activated/liposome fed macrophages (foam cells) exhibited numerous lipid droplets (Fig. 6.4).

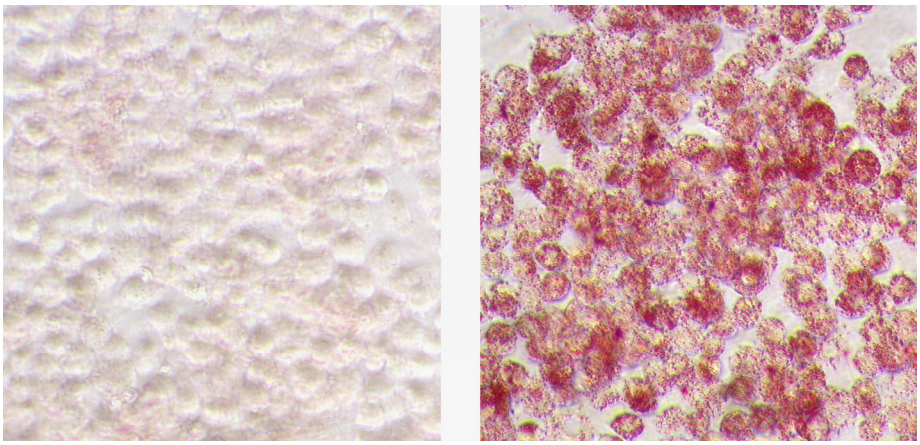

Fig. 6.4 Microscope images of macrophages (left) and foam cells (right). Both cell preparations are stained with oil red O. Macrophages contain essentially no lipid droplets while macrophages differentiated into foam cells (right) exhibit numerous lipid droplets.

We also use Perkin-Elmer Spectrum BX FTIR to measure the relative absorption strengths of different biological tissues. Bovine tissue samples of adipose, aorta, coronary artery, and heart muscle were obtained immediately after the animals were butchered. The animals were healthy and the artery tissues did not contain signs of athermanous lesion. Tissues were cut to 1 cm by 1 cm squares, 2 to 3 mm in thickness, and flash frozen with liquid nitrogen to prevent water crystal formation. The tissues were then embedded with OCT embedding compound and the temperature were allowed to rise to about -25 degree Celsius inside aLeica CM1850 Cyrostat. Upon reaching this temperature, the tissues were cryotome sectioned to 7 micrometer in thickness and laid flat against and covering most of the 15mm aperture of KCl IR card (International Crystal Laboratories, Garfield, NJ). These prepared optical specimens were kept on ice to prevent dehydration when transporting to the FTIR facility. FTIR spectroscopy was performed using a Perkin-Elmer Spectrum BX at 1nm resolution and averaged across 8 scans. During FTIR spectroscopy, no provision was made to prevent tissue from dehydrating. As a result each subsequent scan showed decreased water absorption. However, all samples should have experience roughly similar dehydration.

In laser ablation experiments, tissue samples were cut to about 1.5 cm by 1.5 cm squares, 2 to 3 mm in thickness and flattened with the back of the tissue piece against a piece of glass slide. Laser focus on the surface of the sample was determined by measuring the spot size and adjusted to lower the laser intensity if required by moving past the laser focus. However, to ease data interpretation, all ablations in the same experiment are performed at the same distance from the laser focus. For the experiments comparing the ablation threshold of adipose and artery tissue, the samples did not undergo a drying process. These experiments typically took less than 1 hour and the tissue samples are placed in 3.5% formaldehyde in PBS, pH 7.4, immediately afterward for preservation and further histological examination. After dehydration with a series of increased concentration of alcohol and then xylene, the specimens were embedded in paraffin and sectioned to 7 μm. Tissue sections were affixed to glass microscope slides and stained with hematoxylin and eosin.

3. Mid-infrared spectroscopy of biological samples

Mid-IR absorption spectra of the components of normal artery, which includes endothelial cells and smooth muscle cells, are illustrated in Fig. 6.5a and 6.5b. As the compositional elements of the normal artery, endothelial cells and smooth muscle cells exhibit similar absorption features in the 2.6-3.8 μm wavelength range. A broad absorption feature ranging from 2.8-3.2 μm and peaking at ~3050 nm is observed, and can be attributed to the vibrational bands of O-H stretching in the hydroxyl group and N-H stretching present in the protein amino acids [1,2].

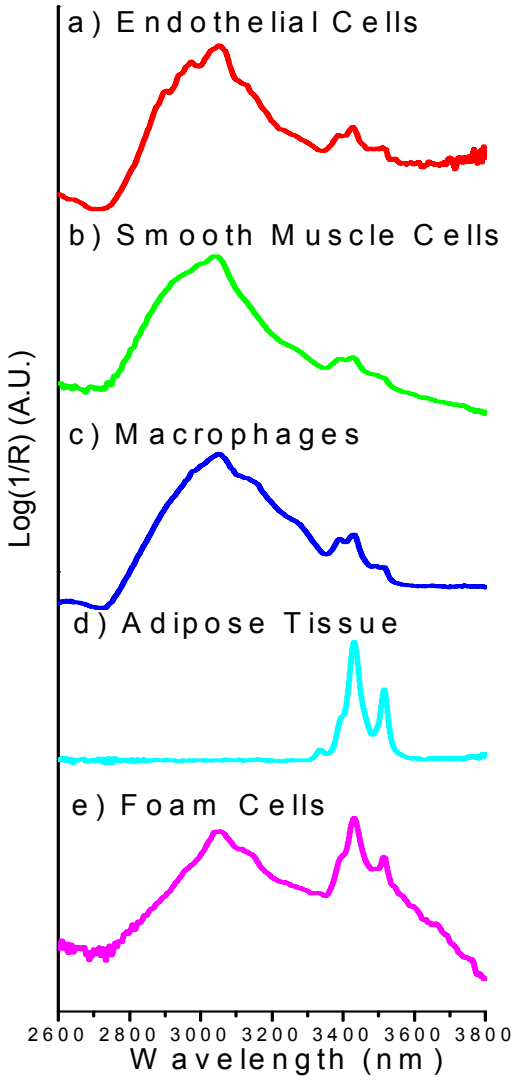

Fig. 6.5 Mid-IR reflection-absorption spectra of normal artery and atherosclerotic plaque constituents. (a) Endothelial cells, (b) smooth muscle cells, (c) macrophages, (d) adipose tissue, and (e) foam cells.

The absorption spectra for the constituents of AP, including macrophages, adipose tissue, and foam cells are illustrated in Fig. 6.5c, 6.5d and 6.5e. In the lipid-rich samples, including adipose tissue and foam cells, we are able to distinguish the individual absorption lines in the 3.2-3.6 μm windows, e.g. =CH stretching vibration at ~3330 nm, CH_3 stretching vibration at ~3390 nm, and CH_2 stretching vibration at ~3420 nm and ~3510 nm [1]. In addition, while the macrophages exhibit a similar absorption spectrum as compared to the normal artery cells,

prominent spectral characters between ~3.2 to 3.6 μm with two absorption peaks at ~3420 nm and ~3510 nm are observed in the macrophages-transformed foam cells and adipose tissue absorption spectra. Such spectral pattern arises from the absorptions of hydrocarbon chains, e.g. CH_2 and CH_3 bonds, present in both the fatty acids and cholesterol esters [2]. Therefore, the spectral difference between the macrophages and foam cells is consistent with the pathological relationship between these two cell types, i.e. macrophages engulf lipid-rich substances to become foam cells.

To further investigate the composition properties of the constituents of AP, we measure the absorption spectrum of egg yolk, which is considered to be a conventional composite model of atherogenic lipoprotein [16]. The spectral character of egg yolk (Fig. 6.6), shares many similarities with that of foam cells (see Fig 6.5e). Compared to endothelial cells and smooth muscle cells, which form the normal artery, egg yolk shows clear lipid-rich absorption features in 3.2-3.6 μm wavelength range while having comparable absorptions in the 2.8-3.2 μm O-H and N-H vibrational bands. More detailed physical modeling and spectroscopic study of the atherosclerotic tissues have also been conducted by other groups Ref [2,9,17].

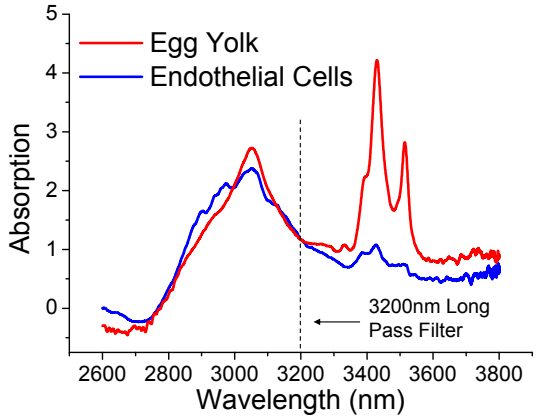

Fig. 6.6 Mid-IR reflection-absorption spectra of (a) egg yolk, and (b) endothelial cells. The two absorption spectra are plotted in logarithm scale and vertically displaced to match the absorption feature ~3 μm.

4. Selective ablation of lipid-rich tissues

Selective ablation takes advantage of the differential absorption of different tissues. In other words, the targeted tissue is preferentially heated to a temperature lethal to cells by laser radiation within the corresponding signature absorption band. Figure 6.7 illustrates the relative absorption spectra of adipose tissue in comparison with arteries and heart muscle. All the samples are prepared by microtome techniques to have a uniform thickness of ~7 μm as explained earlier. We observe that the adipose tissue demonstrates dominant absorption peaks associated with the fatty acids in the 3.2-3.6 μm window compared to artery and muscle components. The measurements confirm that the lipid-rich tissues are prone to absorbing more light in the 3.2-3.6 μm spectral region. It should be noted that the variation of the sample thicknesses is estimated to be ~2 μm, which may contribute to the difference of the baseline absorbance around 2.5 μm. Therefore, we hypothesize, by blocking the common absorption band with a 3.2 μm long wavelength pass filter, that adipose tissue could be preferentially heated by the SC laser pulse through the tissue specific absorption band in 3.2-3.6 μm.

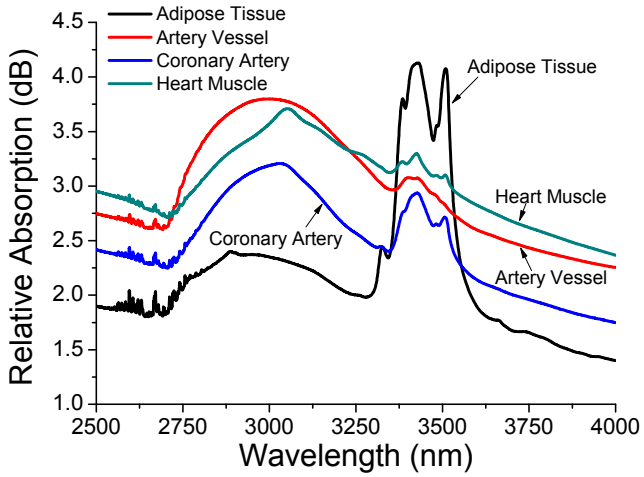

Fig. 6.7 FTIR absorption spectra of (a) adipose tissue, (b) artery vessel, (c) coronary artery, and (d) heart muscle. The thickness of the samples is 7 μm +/- 2 μm. The spectra are plotted in logarithm scale.

We perform selective ablation of adipose tissue in comparison to artery wall (Fig. 6.8) using the SC laser. Each spot of the sample is exposed under the filtered SC light (3.2-3.6 μm) for 5 s with an estimated beam focal spot size of ~3 mm. Selective ablation, i.e. preferentially heating of adipose tissue without damaging artery tissue, is observed under light microscopy with a SC laser fluence starting as low as ~15 mJ/mm^2. On the other hand, we can not identify any surface damage or colorization in the artery sample over the entire range of ~10-100 mJ/mm^2. For example, a laser fluence of ~33 mJ/mm^2 is calculated by using an incident laser power of ~47 mW, an exposure time of 5 s and a beam diameter of ~3 mm. Figure 6.8b shows the surface morphological difference between adipose tissue and bovine artery at power levels around ~40 mJ/mm^2 using light microscope images, which exhibit thermal damage in adipose tissue but no visible surface damage in bovine artery.

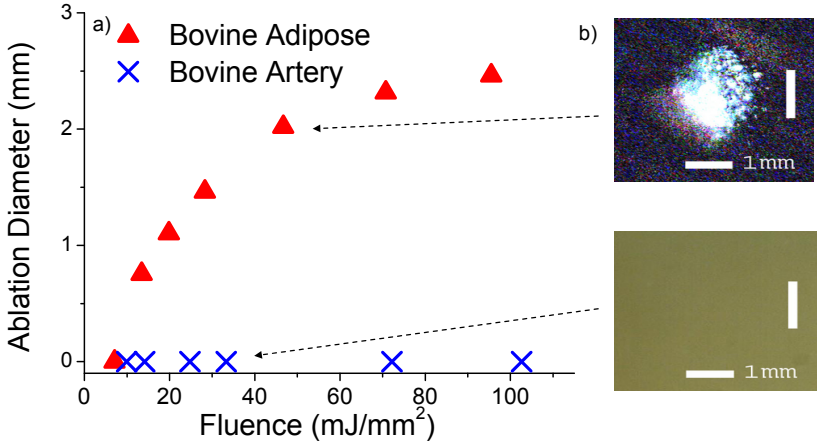

Fig. 6.8 Selective ablation of adipose tissue. (a) Power dependence of the ablation diameter in adipose tissue and bovine artery, and (b) tissue image after ablation at different laser fluence levels. Laser pulse duration is 1 ns, and exposure time is 5 s. The adipose tissue image is processed to better contrast the ablated region (bright color) with unaffected region (dark color).

To further confirm our hypothesis, we conduct cross section histology to study the biological integrity and possible subsurface damage to bovine artery. Histological sections were prepared according to the procedures presented in Section 2. Figure 6.9a shows the

H&E stained cross section histology of the artery tissue at different laser power levels. While laser induced damage can be observed at a laser fluence of ~102 mJ/mm^2, very subtle effects exist at ~72 mJ/mm^2, and no effect was seen at ~33 mJ/mm^2 We also observe the same slides under polarized light to detect birefringence of collagen. We observe some loss of birefringence, which corresponds to the denaturing of the collagen, at ~102 mJ/mm^2, but no changes in birefringence could be detected at laser fluence of ~72 mJ/mm^2 and ~33 mJ/mm^2 (Fig 6.9b). The H&E and birefringence results are consistent because collagen typically has a higher thermal tolerance than other artery tissue components, e.g. endothelium and smooth muscle cells.

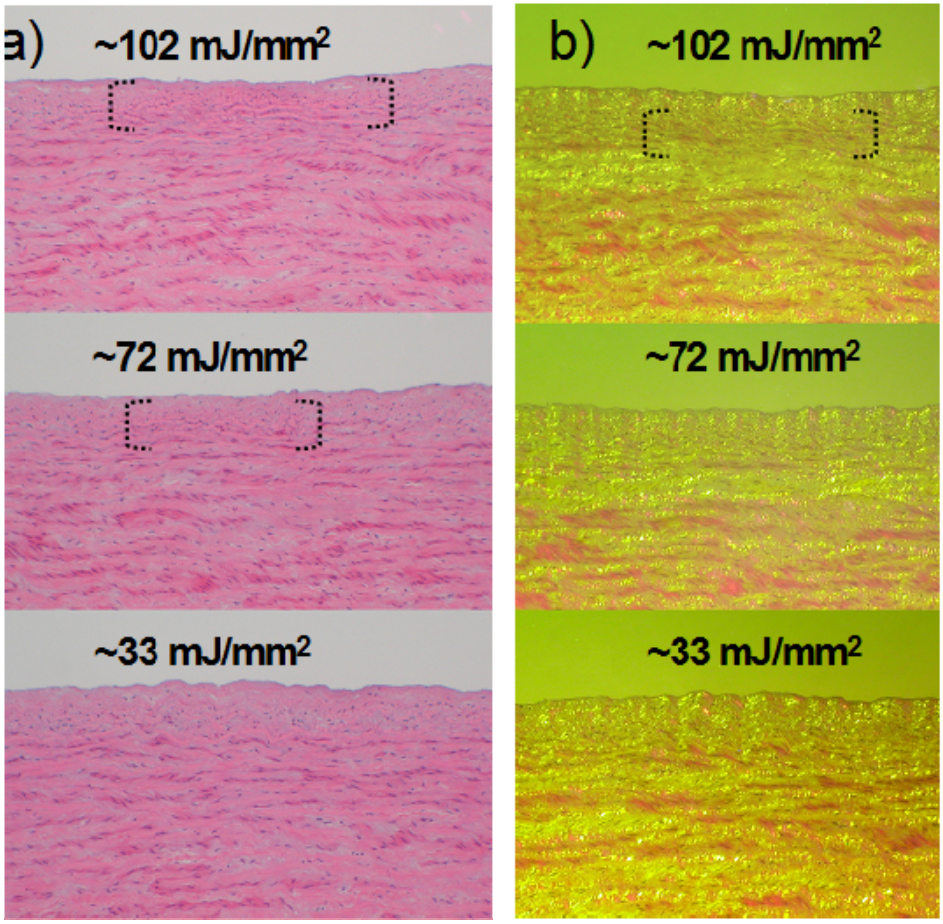

Fig. 6.9 Histology of adipose tissue at different laser fluence levels. (a) H&E stained, and (b) birefringence imaging. Areas of laser effect are indicated by dotted line brackets.

5. Discussion

Our SC laser can serve as the light source for mid-IR spectroscopy measurements. Using the mid-IR SC laser, we show that the spectral fingerprinting and absorption spectroscopy data is consistent with previously reported data in the 2.5-4 μm wavelength range that is obtained using either a traditional lamp based or a synchrotron laser based FTIR measurement system [2,9,18]. Compared to the low signal power available in the lamp based system and the complex setup of the synchrotron laser, the all-fiber-integrated light source has no moving parts, operates at room temperature, and can be scaled up in time-averaged power to exceed 10 W [14]. Our SC laser based spectroscopy system is able to reveal the subtle spectral difference between different biological samples with adequate signal-to-noise ratio. The results are consistent with the chemical composition of the biological samples, where the C-H stretching bonds present in the lipid-rich tissues give rise to the absorption band in 3.2-3.6 μm, while N-H and O-H bonds dominant in the normal artery tissue absorb light in the 2.8-3.2 μm region [2]. We measure the absorption spectra by using a SC average power of <1 mW and scale up the power to the range of 20-200 mW (~10-100 mJ/mm^2) for ablation experiments. In addition, while optical microscopy is sufficient to track damage to adipose tissue, histological staining is required to reveal the very subtle damage in artery tissue. We observe subtle changes in H&E staining at lower laser fluence than we could find any decreases in the collagen birefringence, which indicates that loss of birefringence is not the most sensitive simple method for detecting tissue damage.

Our spectroscopic results indicate that fat tissue would absorb more energy in the 3.2-3.6 μm window. This was confirmed by irradiating adipose and artery tissues, where greater effect was seen in adipose tissue at laser fluences that caused no visible effect in artery.

Changes in collagen birefringence were previously used as a marker for free electron laser-induced damage to tissues [13]. Our results of mid-IR irradiation of artery wall suggest that careful examination of H&E-stained tissue sections may be a slightly more sensitive approach to detection of effects on tissues as compared to loss of collagen birefringence in tissue sections. For example, slight increases in staining intensity and slight decreases in thickness of the superficial layer of the artery wall were seen at a fluence of ~72 mJ/mm^2 while in the same tissue no difference in birefringence could be detected with confidence. It is likely, that future studies of mid-IR effects on tissues *in vivo* will require evaluation of effect by even more sensitive measures such as detection of caspase-3 activity, an indicator of apoptosis [19]. We speculate that fluences that cause the changes seen here in adipose or artery tissues may be greater than would be needed to cause cell death within tissues of a living organism.

Heart attack is caused by the clot formation in coronary arteries due to the rupture of vulnerable atherosclerotic plaque (AP) [20]. In the AP of an affected artery, smooth muscle cells migrate to form a fibrous cap that overlays atherogenic matter including lipids, macrophages and foam cells [20]. We observe distinct spectral signatures of the constituents of AP in the 3.2-3.6 μm wavelength window. The mid-IR SC laser based spectroscopy could potentially be used to diagnose atherosclerosis diseases.

Studies of AP with infrared spectroscopy have been reported using Fourier transform infrared spectroscopy (FTIR) based spectroscopy [9,17,18], near-IR reflectance spectroscopy [21], Raman spectroscopy [22], and mid-IR reflection spectroscopy with a synchrotron laser [2]. Compared to the spectroscopic studies of the first overtone features in the near-IR wavelength range, the mid-IR spectral characters of AP compositions not only possess a

~100x enhancement of signal absorbance but also exhibit clear absorption peaks, e.g. ~3420 nm and 3510 nm, which are attributed to the fundamental vibrational modes of the lipid-rich materials contained in AP [23]. Furthermore, advanced mathematical algorithm, e.g. multivariate data analysis [24], can also be employed to process the mid-IR AP spectral signatures to enhance the diagnosis sensitivity and selectivity. Future study needs to be carried out to evaluate the significance of water and blood absorption in the mid-IR region and their impact on the absorption spectroscopy measurements of the biological targets of interest, e.g. AP compositions [2].

The demonstrated selective ablation of adipose tissue versus healthy artery also suggests a potential therapeutic method using the mid-IR SC laser. The laser damage threshold of adipose tissue, which is ~15 mJ/mm^2, is about half of the power required to ablate the normal artery, that is ~40 J/mm^2. As pointed out in the previous analysis, the absorbance of laser energy in the mid-IR is considerably higher than that in the near-IR, which results in a reduction of the ablation power threshold. While watts of laser power in near-IR (~1-2 μm) can only heat fatty samples above physiological temperature [13], only tens of milliwatts of laser power are required to ablate tissue in the 3.2-3.6 μm regime, which is consistent with the results achieved by free electron lasers at 5.75-6.1 μm [12]. Therefore, with the potential dual capability of locating AP and selective ablation, treatment might be accomplished in a catheter-based, minimally invasive procedure that might be an add-on to the angiogram (i.e., use the guide wire already in place to insert the mid-IR catheter). The efficacy of the selective ablation approach needs to be further studied. The open questions include whether laser ablation will cause any significant adverse responses, e.g. inflammation or thrombosis caused by the plaque rupture due to the weakening of the fibrous cap [20]. Further studies

must also be conducted to find the optimal laser operation conditions, such as pulse width, energy per pulse, and wavelength band, for both spectroscopic detection and selective ablation.

The techniques described for absorption spectroscopy and selective ablation could be extended to *in vivo* arterial operation by coupling the SC light into an appropriate catheter. Existing mid-IR catheters, e.g. hollow glass waveguide catheter [9] and germanium oxide fiber catheter [25], either require direct contact with the sample under test or employ large core multimode fibers. We propose a single-mode ZBLAN fiber based endoscopic catheter that uses achromatic reflective optics and allows noncontact measurement. As illustrated in Fig. 6.10, the proposed catheter is composed of three main components, i.e. a single mode ZBLAN fiber, a 90 degree off-axis micro concave mirror, and a rotational micro-motor. The mid-IR light emitting from the angle-cleaved ZBLAN fiber tip is first re-directed by 90 degrees and collimated by the concave mirror. To confine the collimated beam diameter to the order of ~100-200 μm, the radius curvature of the micro concave mirror would be ~250 μm. The micro-mirrors could be fabricated and implemented by MEMS techniques on silicon substrate with gold coating [26,27]. The concave mirror could be mounted onto a 1 mm diameter rotational micro-motor to enable the 360-degree peripheral optical scan [28,29]. In addition, a radio opaque tip could be installed in the front end of the catheter for the position guidance. Furthermore, as reported in Ref [2], reflective mid-IR light can be collected from the atherosclerotic aorta due to the refractive index mismatch between the calcium deposits and normal artery constituents. Hence, the reflection-absorption technique we demonstrate could be applied to measure spectral features of the calcium-rich tissue, e.g. atherosclerotic artery, in the live biological environment without inserting any external optical reflectors.

The miniature disposable catheter with an outer diameter of ~1 mm could be mechanically coupled to the output pigtail of a SC laser to construct an integrated, minimally invasive *in vivo* reflective absorption spectroscopy and laser ablation system.

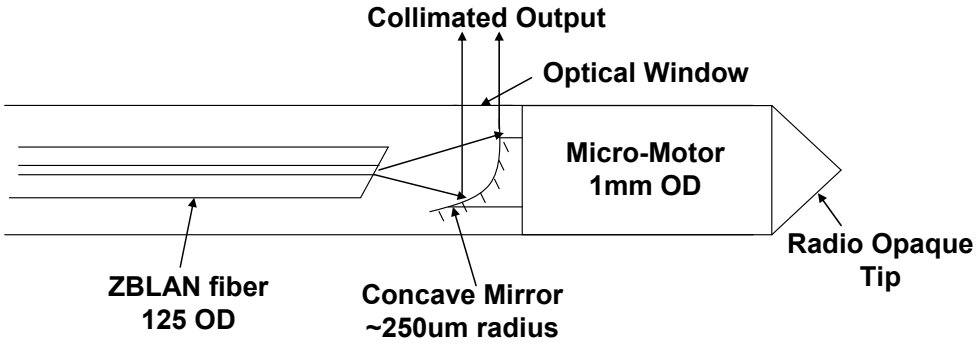

Fig. 6.10 Proposed mid-IR catheter design for reflection-absorption spectroscopy and laser ablation.

In summary, mid-IR absorption spectra of the structural components of normal artery and AP have been measured by using an all-fiber-integrated SC laser source. Distinctive spectral signatures in 3.2-3.6 μm range that are associated with fatty acids and cholesterol esters absorption are present in the components of AP including foam cells and adipose tissues. On the other hand, endothelial cells, smooth muscle cells and macrophages have a more dominant feature at 2.8-3.2 μm, corresponding to protein and water absorption. Selective ablation of the lipid-rich material has been demonstrated by using the SC laser to target the 3.2-3.6 μm fatty acids and cholesterol esters absorption band under laser fluence ranges of ~15-40 mJ/mm^2 for adipose tissue.

Substantial contents in this chapter are contained in a manuscript as: C. Xia, K. Ke, M. N. Islam, M. J. Welsh, and M. J. Freeman, "Mid-infrared absorption spectroscopy and selective ablation *in vitro* between lipids and proteins by an all-fiber-integrated supercontinuum laser."

References

[1] C. Paluszkiewicz, W. M. Kwiatek, A. Banas, A. Kisiel, A. Marcelli, and A. Piccinini, "SR-FTIR spectroscopic preliminary findings of non-cancerous, cancerous, and hyperplastic human prostate tissues," Vib. Spectrosc. **43**, 237-242 (2007).

[2] H. –Y. N. Holman, K. A. Bjornstad, M. C. Martin, W. R. Mckinney, E. A. Blakely, and F. G. Blankenberg, "Mid-infrared reflectivity of experimental atheromas," J. Biomed. Opt. **13**, 030503 (2008).

[3] K. A. Tillman, R. R. J. Maier, D. T. Reid, and E. D. McNaghten, "Mid-infrared absorption spectroscopy across a 14.4 THz spectral range using a broadband femtosecond optical parametric oscillator," Appl. Phys. Lett. **85**, 3366-3368 (2004).

[4] E. Sorokin, I. T. Sorokina, J. Mandon, G. Guelachvili, and N. Picqué, "Sensitive multiplex spectroscopy in the molecular fingerprint 2.4 μm region with a Cr2+:ZnSe femtosecond laser," Opt. Express **15**, 16540-16545 (2007).

[5] M. Razeghi, S. Slivken, Y. Bai, and S. R. Darvish, "The quantum cascade laser: a versatile and powerful tool," Opt. Photon. News **19**, No. 7 42-47 (2008).

[6] J. Mandon, E. Sorokin, I. T. Sorokina, G. Guelachvili, and N. Picqué, "Supercontinua for high-resolution absorption multiplex infrared spectroscopy," Opt. Lett. **33**, 285-287 (2008).

[7] J. M. Langridge, T. Laurila, R. S. Watt, R. L. Jones, C. F. Kaminski, J. Hult, "Cavity enhanced absorption spectroscopy of multiple trace gas species using a supercontinuum radiation source," Opt. Express **16**, 10178-10188 (2008).

[8] C. F. Kaminski, R. S. Watt, A. D. Elder, J. H. Frank, and J. Hult, "Supercontinuum radiation for applications in chemical sensing and microscopy," Appl. Phys. B **92**, 367–378 (2008).

[9] B. A. Hooper, A. Maheshwari, A. C. Curry, and T. M. Alter, "Catheter for diagnosis and therapy with infrared evanescent waves," Appl. Opt. **42**, 3205-3214 (2003).

[10] A. P. Joglekar, H. Liu, G. J. Spooner, E. Meyhofer, G. Mourou, and A. J. Hunt, "A study of the deterministic character of optical damage by femtosecond laser pulses and applications to nanomachining," Appl. Phys. B **77**, 25-30 (2003).

[11] Y. Xiao, M. Guo, P. Zhang, G. Shanmugam, P. L. Polavarapu, and M. S. Hutson, "Wavelength-dependent conformational changes in collagen after mid-infrared laser ablation of cornea," Biophys. J. **94**, 1359-1366 (2008).

[12] K. Awazu, A. Nagai, and K. Aizawa, "Selective removal of cholesterol esters in an arteriosclerotic region of blood vessels with a free-electron laser," Lasers Surg. Med. **23**, 233-237 (1998).

[13] R. R. Anderson, W. Farinelli, H. Laubach, D. Manstein, A. N. Yaroslavsky, J. Gubeli, K. Jordan, G. R. Neil, M. Shinn, W. Chandler, G. P. Williams, S. V. Benson, D. R. Douglas, and H. F. Dylla, "Selective photothermolysis of lipid-rich tissues: A free electron laser study," Lasers Surg. Med. **38**, 913-919 (2006).

[14] C. Xia, Z. Xu, M. N. Islam, F. L. Terry, Jr., M. J. Freeman, A. Zakel, and J. Mauricio, "10.5 watts time-averaged power mid-infrared supercontinuum generation extending beyond 4 μm with direct pulse pattern modulation", IEEE J. Sel. Top. Quantum Electron., (to be published).

[15] A. D. Kinkel, M. E. Fernyhough, D. L. Helterline, J. L. Vierck, K. S. Oberg, T. J. Vance, G. J. Hausman, R. A. Hill, and M. V. Dodson, "Oil red-O stains non-adipogenic cells: a precautionary note", Cytotechnology **46**, 49-56 (2004).
[16] D. Kritchevsky, "Dietary-protein, cholesterol and atherosclerosis-a review of the early history," J. Nutr. **125**, S589-S593 (1995).
[17] T. Arai, K. Mizuno, A. Fujikawa, M. Nakagawa, and M. Kikuchi, "Infrared absorption spectra ranging from 2.5 to 10 μm at various layers of human normal abdominal aorta and fibrofatty atheroma in vitro," Lasers Surg. Med. **10**, 357-362 (1990).
[18] J. M. Gentner, E. Wentrup-Byrne, P. J. Walker, and M. D. Walsh, "Comparison of fresh and post-mortem human arterial tissue: An analysis using FT-IR microspectroscopy and chemometrics," Cell. Mol. Biol. **44**, 251-259 (1998).
[19] T. Fernandes-Alnemri, G. Litwack, and E. S. Alnemri, "CPP32, a novel human apoptotic protein with homology to *Caenorhabditis elegans* cell death protein Ced-3 and mammalian interleukin-lβ-converting enzyme," J. Biol. Chem. **269**, 30761-30764 (1994).
[20] P. Libby, "Atherosclerosis: The new view," Sci. Am. **286**, 47-55 (2002).
[21] J. D. Caplan, S. Waxman, R. W. Nesto, and J. E. Muller, "Near-infrared spectroscopy for the detection of vulnerable coronary artery plaques," J. Am. Coll. Cardiol. **47**, C92-C96 (2006).
[22] T. J. Römer, J. F. Brennan, III, M. Fitzmaurice, M. L. Feldstein, G. Deinum, J. L. Myles, J. R. Kramer, R. S. Lees, and M. S. Feld, "Histopathology of human coronary atherosclerosis by quantifying its chemical composition with Raman spectroscopy," Circulation **97**, 878-885 (1998).
[23] P. R. Moreno, B. J. Marshik, and J. E. Muller, "Diffuse reflectance near-infrared spectroscopy as a clinical technique to detect high-risk atherosclerotic plaques," in Handbook of the Vulnerable Plaque, R. Waksman and P. W. Serruys, eds. (Taylor & Francis, 2004), pp. 205-218.
[24] L. Wang, J. Chapman, R. A. Palmer, O. van Ramm, and B. Mizaikoff, "Classification of atherosclerotic rabbit aorta samples by mid-infrared spectroscopy using multivariate data analysis," J. Biomed. Opt. **12**, 024006-1-11 (2007).
[25] N. J. Scott, R. A. Barton, A. L. Casperson, A. Tchapyjnikov, K. Levin, D. Tran, and N. M. Fried, "Mid-IR germanium oxide fibers for contact erbium laser tissue ablation in endoscopic surgery," IEEE J. Sel. Top. Quantum Electron. **13**, 1709-1714 (2007).
[26] S. -Y. Hsiao, C. –C. Lee, and W. Fang, "The implementation of concave micro optical devices using a polymer dispensing technique," J. Micromech. Microeng. **18**, 085009 (2008).
[27] N. Kanbara, S. -I. Tezuka, and T. Watanabe, "MEMS tunable VCSEL with concave mirror using the selective polishing method," Proc. IEEE Optical MEMS, 9–10 (2006).
[28] H. Zhang, S. –X. Dong, S. –Y. Zhang, T. -H. Wang, Z. -N. Zhang, and L. Fan, "Ultrasonic micro-motor using miniature piezoelectric tube with diameter of 1.0 mm," Ultrasonics **44**, e603–e606 (2006).
[29] A. Geisberger, D. Kadylak, and M. Ellis, "A silicon electrothermal rotational micro motor measuring one cubic millimeter," J. Micromech. Microeng. **16,** 1943–1950 (2006).

Chapter VII

Summary and Future Work

1. Summary

To summarize, the SC laser system reported in this thesis has made significant improvements as illustrated in Fig. 7.1.

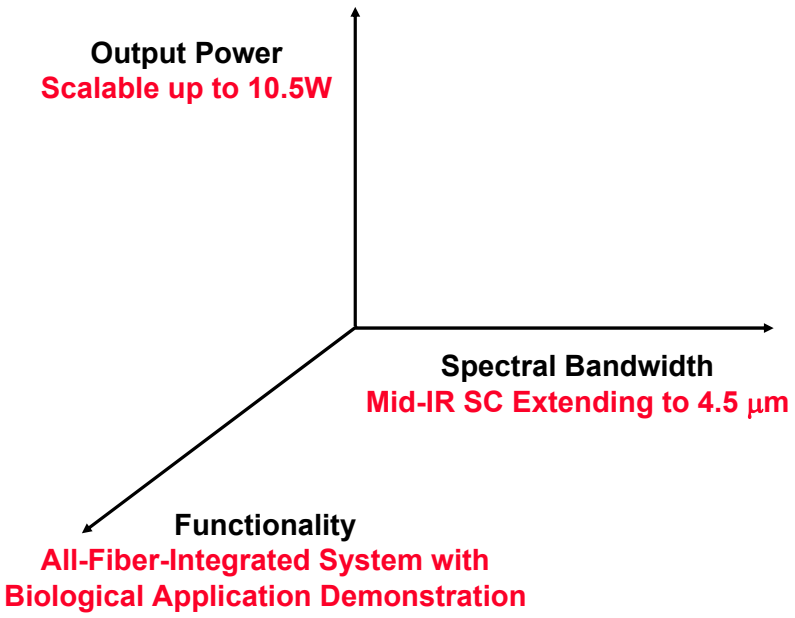

Fig. 7.1 Challenges and achievements of the mid-IR SC laser system.

More specifically, a novel all-fiber-integrated mid-IR SC laser system is developed and demonstrated. The SC laser is composed of an all-fiber-spliced high power pump laser system followed by nonlinear generation fibers, including ZBLAN fibers and silica fibers. The pump laser system for the SC generation consists of a seed LD followed by multiple

stages of erbium-doped and erbium/ytterbium co-doped fiber amplifiers. The seed LD emits optical pulses with pulse duration from 0.5-2 ns at 1.55 μm telecommunication window. The SC light source has no moving parts, eliminates the need of mode-locked lasers, and operates under room temperature.

SC generation is demonstrated in ZBLAN fibers with a continuous spectrum ranging from ~0.8 to ~4.5 μm. The time-averaged power has also been scaled up to 10.5 W. SC is also generated in silica fibers with the long wavelength spectral edge extended to ~3 μm and the time-averaged power scaled up to 5.3 W. Theoretical simulations and modeling have been carried out to study the SC generation mechanism and investigate the limits of the power handling and SC long wavelength edge in the ZBLAN fibers. The SC long wavelength edge is limited by the material absorption loss and the maximum power handling of the optical fiber is thermally limited when the fiber core temperature approaches the material melting temperature.

SC is generated in the optical fiber primarily through the interaction of SPM, FWM, and SRS. A two-stage approach is used to optimize the SC generation. The first stage comprises a 1~2 m length of SMF fiber, which is spliced to the output of the optical fiber amplifier. By pumping the SMF fiber in the anomalous dispersion region, MI can be phase matched to break up the nanosecond pulses into femtosecond soliton pulse trains, which eliminates the need for mode-locked lasers. The second stage consists of a piece of infrared fiber, i.e. ZBLAN and silica fibers, in which the SC is broadened by fiber nonlinearities including SPM and SRS. By choosing an optical fiber with a zero dispersion wavelength close to the pump wavelength, the SC generation also benefits from the FWM effect due to the reduced dispersion of the nonlinear fiber. The ensemble average of these solitons, which spread over

the entire nanosecond wide pulse, gives rise to the broad, smooth SC spectrum.

The output average power of the SC laser is scalable by varying the pulse repetition rate and adjusting the corresponding pump power of the fiber amplifier. The nanosecond LD based pump system can accommodate different fiber amplifier systems and drastically simplifies the scaling of the time-averaged power. Since the nonlinear phenomena responsible for SC generation are determined the peak power of the pump pulses, the average power in the continuum can be increased simply by increasing the pulse duty cycle while keeping the peak power approximately constant. As shown in Fig. 7.2, we have successfully increased the time-averaged output power of the SC by ~500x, i.e. from ~23 mW to ~10.5 W, over the course of two-and-half-year development period. Our SC laser benefits greatly from the advancement of the high power LDs and fiber amplifier systems. In addition, due to the modular design of the SC laser system, we can replace the older generation power amplifiers with newer version high power amplifiers by merely splicing a few joint points. Such design also simplifies the trouble-shooting process by isolating functional units into different devices.

We also solve the generalized non-linear Schrödinger equation to confirm our hypothesis on SC generation. Theoretical simulation results agree well with the experimental results for both ZBLAN and silica fiber cases. Similar SC spectra can also be obtained by using both femtosecond and nanosecond pump pulses, which shows that our LD-based SC laser system can achieve the same nonlinear performance as the mode-lock lasers. Furthermore, we also predict and propose a few SC generation scenarios by using the developed simulation tools. For example, by tailoring the input pulse shape, we simulate the generation of the entire SC spectrum in one single soliton under quasi-CW pulse pumping scheme.

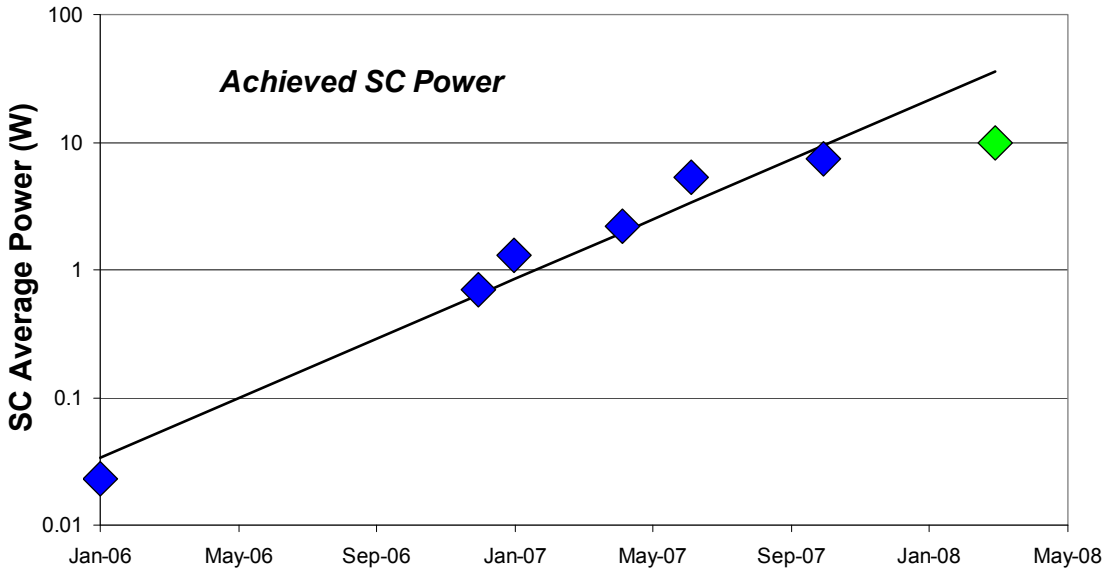

Fig. 7.2 Power scaling roadmap of the mid-IR SC laser.

We further demonstrate mid-IR absorption spectroscopy and selective laser ablation of biological samples using the SC laser. The spectroscopy measurement system incorporates a dual channel signal-reference detection scheme to remove the amplitude fluctuations of the SC spectrum and improve the signal-to-noise ratio of the measurement. We have measured the mid-IR spectral characteristics of the constituents of the normal artery and atherosclerotic plaques. Selective ablation has also been successfully demonstrated by preferentially melting adipose tissue without causing any damages to normal artery by targeting the SC light in the lipid absorption band.

2. Future work

Future research could be conducted in the following aspects to further improve both the performance and practicality of the SC laser system. More specifically, research efforts can be performed to:

1. Improve the strength of the SMF-to-ZBLAN mechanical splice joint;
2. Further extend the long wavelength edge of the SC into mid-IR;

3. Explore the possibility of tailoring the generated SC spectrum;
4. Understand the influence of atmosphere, water and blood absorption exerted on the SC laser based absorption spectroscopy measurement; and
5. Continue to investigate potential applications of the SC laser system.

SMF-to-ZBLAN splice: In our SC laser, we use mechanical splice to butt-couple the optical light from the SMF to ZBLAN fiber. Compared to fusion splicing technique, which essentially melts two individual fibers into one integral piece of glass, mechanical splicing does not physically join the fibers together. Therefore, mechanical splice joints are more susceptible to vibration, tend to be less robust for power handling, and have higher insertion/coupling loss. We intend to further improve the SMF-to-ZBLAN joint by using following approaches.

We can design and employ a more robust and rigid optical coupling fixture for the mechanical splice. Currently, we use off-the-shelf precision stages and stainless steel v-grooves to hold the fibers and couple the light. Customized stages with better mechanical stability and v-grooves made from materials with high thermal conductivity and low thermal expansion coefficient would significantly improve the long-term reliability of the mechanical splice joint. In addition, efforts can also be made to locate a type of optical glue that has both high mechanical strength and excellent thermal conductivity to clamp the ZBLAN fiber more tightly onto the fiber-holding v-groove. It should be noted that the refractive index of the optical glue should be higher than that of ZBLAN material so that the uncoupled light remained in the cladding of the ZBLAN fiber can be efficiently stripped out and dissipated.

In addition, the ends of the corresponding SMF and ZBLAN fibers could be placed into fiber connectors and mechanically mated to achieve reliable optical coupling. Fiber

connectors in various formats are commercially available for silica glass based fibers. Similarly, fiber connectors can also be made onto the end of the ZBLAN fibers. For example, Capey Optronique, a France-based optical equipment company, produces a "diamond alignment" tool kit to construct ZBLAN fiber based connectors. The fiber connector uses copper nickel alloy, which also serves the purpose of heat dissipation, to clamp and hold the ZBLAN fiber. The end of the ZBLAN fiber can be either straight or angle polished to reduce the back-reflection. Adjustments can also be made to position the ZBLAN fiber core at the center of the connector to improve the coupling efficiency. The connector can then be mechanically engaged with another similar SMF fiber based connector to form the light-coupling joint. The SMF-to-ZBLAN insertion/coupling loss of such configuration is estimated to be less than 0.5 dB with a return loss larger than 60 dB. However, we shall conduct a thorough analysis of the thermal performance and power handling of such type of connectors before adopting this technique in any high power applications.

Moreover, fusion splicing ZBLAN to SMF fiber remains as another possibility. Due to its low melting temperature and narrow solid-to-liquid phase transition temperature range [1], it is extremely difficult to achieve high quality fusion splice to connect ZBLAN fibers to another glass fiber. For the SMF-to-ZBLAN splicing, one possible solution is to introduce another material, e.g. tellurite or borosilicate glass, to thermally and mechanically bridge these two fibers, and use a more sophisticated filament splicer. Yet, we are not aware of any existing SMF-to-ZBLAN splice technique that can sustain high time-averaged power operation.

Wavelength extension: Currently, the long wavelength edge of the SC is limited by the material absorption of the ZBLAN fiber, which exhibits a sharp cut-off around ~4-4.5 μm. As

we discussed in previous chapters, SC spectral broadening results from the interaction of nonlinear wavelength generation and optical loss present in the fiber. Hence, to extend the SC spectrum into deep mid-IR wavelength range, there are two conceivable paths—using optical fibers with low loss in the mid-IR or increasing the nonlinearity of the wavelength generation process in the fiber. In the existing system, optical nonlinearity can be enhanced by careful design of the optical fiber. For example, we proposed using a ZBLAN fiber with 0.3 NA and 7 μm core diameter to better confine the optical mode propagating in the fiber. Depending on the development and evolvement of the fiber fabrication techniques, it may be possible that highly nonlinear ZBLAN fibers, which features a small core size, e.g. ~1-2 μm with good optical confinement, can potentially be made. Therefore, SC generation extending beyond 4.5 μm is achievable by using a very short length of ZBLAN fibers, as analogous to that of SC generation in highly nonlinear fused silica fibers.

On the other hand, there are quite a few mid-IR optical fibers developed by different research groups, e.g. chalcogenide fibers, hollow glass fibers, and tellurite fibers. As illustrated in Fig. 7.3, ZLBLAN fluoride glass possesses the lowest loss in the 1-5 μm wavelength regime [1,2]. Recently, modified fluoride glass fiber, which removes the zirconium composition from the glass, has been developed. Such fiber has an optical transmission window ranging from ~1 μm to ~5.5 μm. Therefore, it could be an ideal candidate for extending the SC long wavelength edge further into the mid-IR. However, only multimode optical fiber has been successfully fabricated from the modified fluoride glass due to its peculiar glass properties. The future prospect of SC generation using the new type of fluoride fibers hinges on whether sufficient length of single mode fiber can be reliably made.

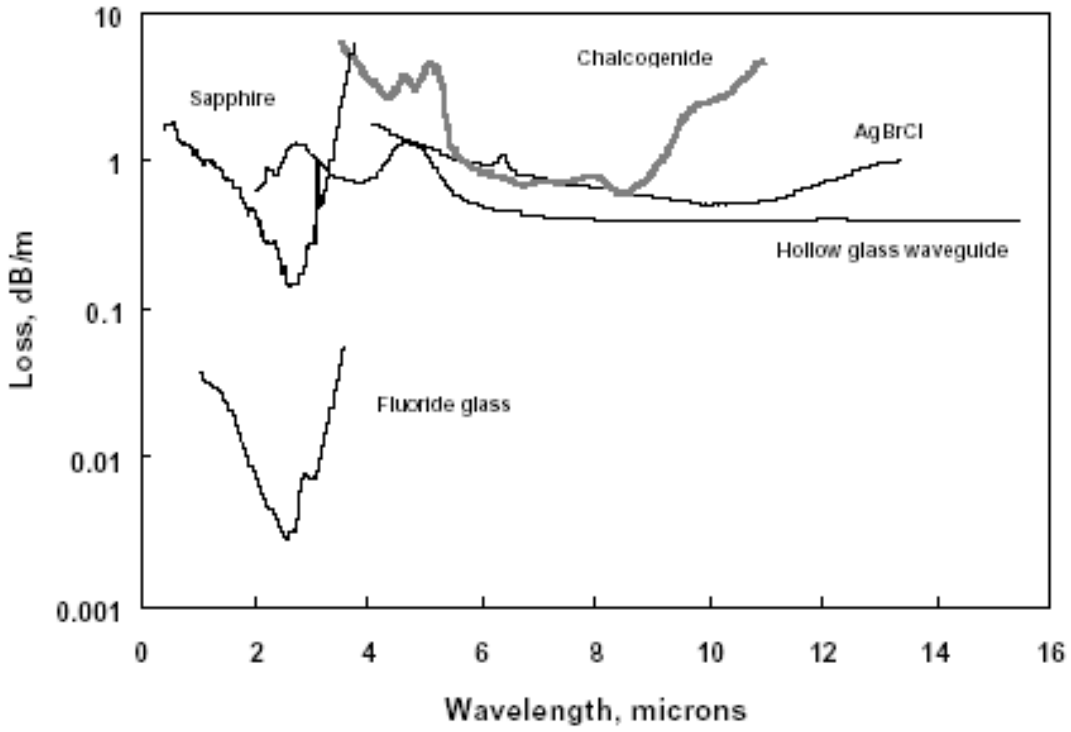

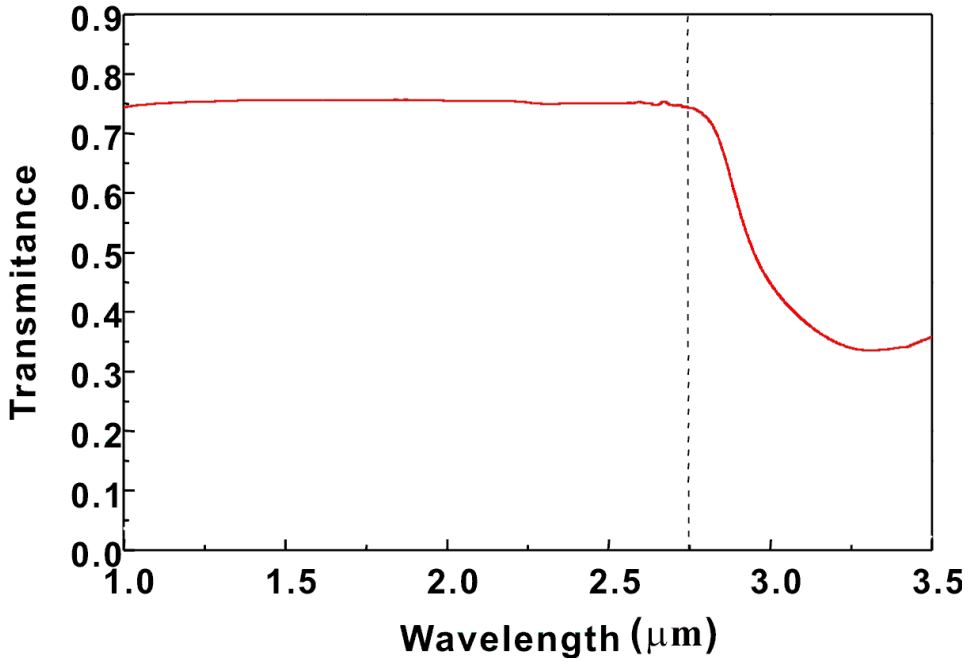

Fig. 7.3 Infrared transmission of various glass materials. (Top) Fluoride, Chalcogenide, Sapphire, AgBrCl, and Hollow glass waveguide. This figure and its description are excerpted from Ref [1]. (Bottom) Tellurite TeO_2 glass. This figure and its description are excerpted from Ref [2].

Chalcogenide fiber is another candidate for SC wavelength extension. For chalcogenide, tremendous amounts of efforts have been made to perfect the glass purification and fiber drawing techniques. Compared to ZBLAN fibers, chalcogenide fibers have lower transmission loss extending to ~8-10 μm and higher nonlinear coefficient. However, there are also several challenges that need to be addressed. First, the damage threshold of chalcogenide glass fiber is ~ 1 GW/cm^2 for nanosecond laser pulse [3], which limits the maximum peak/average power to be coupled into the fiber and restrains the nonlinear effects. Secondly, the bulk material zero dispersion wavelengths of the chalcogenide fibers are typically >3 μm, which is far from the conventional 1.5 μm telecommunication band [3]. Although SC generation ranging from 2-3 μm has also been demonstrated in sulfide and selenide fibers by a 2.5 μm OPA pump laser [4], we are unsure if any high power broadband SC generation can be realized by using a pump system emitting at 1.5 μm. Finally, chalcogenide fibers are susceptible to the photodarkening effect and the concentricity of the fabricated fibers is not well controlled, especially if the fiber is drawn by the double-crucible technique.

Recently, SC generation in tellurite photonic crystal fibers with a long wavelength edge extending close to 5 μm has also been demonstrated [2]. The particular tellurite fiber used in the experiments has an enhanced nonlinearity of ~500x compared to SMF fibers due to the high nonlinearity of the tellurite glass and tight confinement of the photonic crystal structure. Therefore, only 8 mm length of fiber is used to generate a very broad SC spectrum. In our group, we have also tested several tellurite fibers supplied by Prof. Ohishi at Toyota Technological Institute in Japan and Prof. Jha at University of Leeds in UK. However, the particular fibers we received are plagued by issues including glass re-crystallization and weak mechanical strength.

In order to achieve high power SC generation in tellurite glass based fibers, there are still several issues need to be resolved. First of all, the mechanical reliability of the tellurite glass fiber shall be future improved. High power operation usually involves rigid thermal management and heat dissipation requirements. Without a mechanically robust fiber, it would be difficult to implement these cooling techniques, which would significantly limit the optical power that can be handled by the fiber.

Furthermore, step index single mode tellurite fiber might be a better choice for high power mid-IR SC generation. Since the nonlinear coefficient of tellurite glass is one order of magnitude higher than that of ZBLAN fiber, relatively short length of fiber, e.g. 0.5-1 m, will be sufficient for broadband SC generation. The benefits accompanied by the step index single mode fibers are certainly not negligible. In contrast with photonics crystal fibers, step index fibers generally are more robust, easier to handle, and have better thermal tolerance due to its large core size. What is more, the intrinsic zero dispersion wavelength of different tellurite glasses is around 1.8-2 μm. So the red-shifted solitons generated from the 1.5 μm pump wavelength can experience a low, anomalous dispersion when propagating in the tellurite fiber, which facilitates efficient SC generation. Although ZBLAN fibers are still technologically more mature, by using new mid-IR fibers with improved thermal/power handling and optical quality, high power SC generation extending beyond 5 μm could be potentially achieved.

Spectrum tailoring: SC spectrum tailoring has also attracted a great amount of research efforts in the recent years. Although SC generation can be initiated by an optical seed at a particular wavelength, it is very difficult to selectively enhance or confine majority of the SC generation in a certain optical band, e.g. 2-2.5 μm. Optical gratings and dispersion

engineering have been applied onto optical fibers to help shape the SC spectrum.

Another promising technique is to rely on the parametric phasing matching of the pump and signal wavelengths in the optical fiber. FWM is a parametric amplification in a fiber where phase matching condition needs to be satisfied between the pump waves and signal waves (Stokes and Anti-Stokes waves). In the four photon process, two pump photons are translated into a Stokes (smaller frequency or longer wavelength) photon and an anti-Stokes (larger frequency or shorter wavelength) photon (Fig. 7.4). Energy conservation requires that $\omega_{p1} + \omega_{p2} = \omega_S + \omega_A$. The two pump photons can in general be at different frequencies, but in the following we will consider first the degenerate case of two pump photons at the same frequency. Conservation of momentum requires that the wave vectors also match, $k_{p1} + k_{p2} = k_S + k_A$, which translates into a phase matching requirement. More explicitly, the phase matching condition can be re-written into $\frac{n_{p1}\omega_{p1}}{c} + \frac{n_{p2}\omega_{p2}}{c} = \frac{n_s\omega_s}{c} + \frac{n_A\omega_A}{c}$, where ω is the angular frequency of the photons, n the refractive index and c the speed of the light. Contrary to MI as mentioned above, the phase matching condition can only be satisfied when the optical fiber is pumped in the normal dispersion regime, i.e. pump wavelength < zero dispersion wavelength.

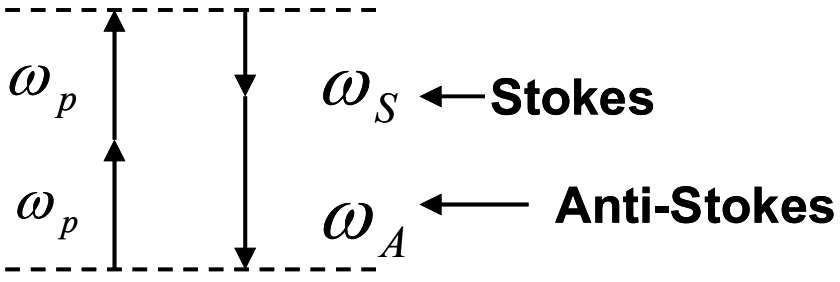

Fig. 7.4 Parametric four-wave mixing process.

The experimental setup for demonstrating FWM is the same as the SC generation setup. The pump laser is first coupled into ~0.5 m SMF fiber followed by a dispersion shifted fiber (FWM fiber) with a zero dispersion wavelength >1.55 μm. During the test, three silica fibers, which are available in the laboratory, with zero dispersion wavelengths at 1560 nm, 1570 nm, and 1610 nm respectively have been tested. The zero dispersion wavelength of the ZBLAN fiber under test is estimated to be ~1700 nm. In contrast with SC generation experiment, the pump peak power is generally lower, which is in the range of ~100-1000 W. Such a low peak power ensures that majority of the pump power remains in the vicinity of the 1.55 μm. Therefore, the amplified LD pulses will experience a normal dispersion environment in the optical fiber, which is required by the FWM phase matching condition.

The spectral output from silica fibers with a zero dispersion wavelength at 1560 nm under different peak pump input powers is illustrated in Fig. 7.5a. Two peaks at 1400 nm (anti-Stokes) and 1750 nm (Stokes), respectively can be observed when the input power reaches 255 W. The spectral power of the two peaks grows by ~20 dB (100x) when the pump power is increased to 635 W. The spectrum of the two peaks is broadened due to the SPM and SRS when the input pump power is further increased. Similar behaviors are also obtained in silica fibers with zero dispersion wavelengths at 1570 nm and 1610 nm as shown in Fig. 7.5b and 7.5c, respectively. Finally, we observed two peaks, one at 1020 nm and the other at 3250 nm for ZBLAN fiber (Fig. 7.5d). It should be noted that these two peaks are masked by continuum generation due to the high peak pump power.

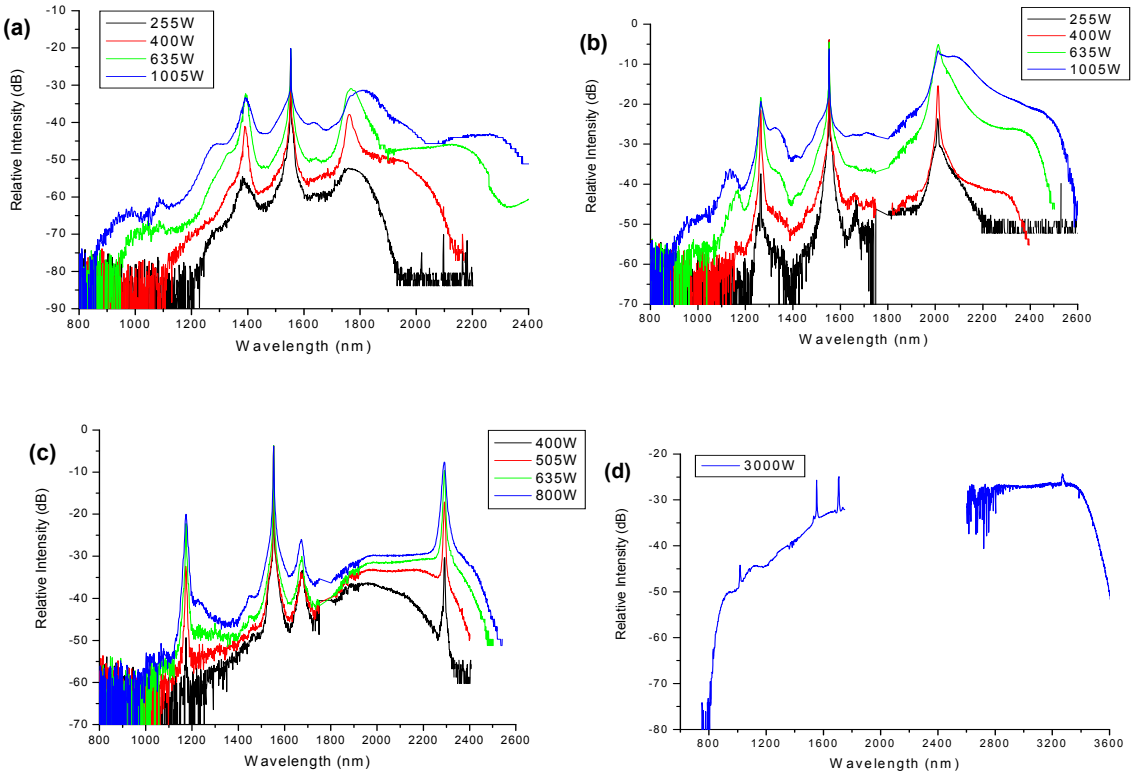

Fig. 7.5 Experimental results of FWM generation. Spectrum after 5 m (a) 1560 nm, (b) 1570 nm, and (c) 1610 nm zero dispersion wavelength highly nonlinear silica fiber; and after 5 m (d) 1700 nm zero dispersion wavelength ZBLAN fluoride fiber.

Theoretical calculations have also been carried out to predict the Stokes and anti-Stokes peaks based on the phase matching conditions of different fibers. Table 7.1 lists the corresponding anti-Stokes and Stokes wavelengths which can be generated in the fibers with different dispersion profiles under 1553 nm pump. The experimental results agree very well with the theoretical calculations, with the slight offset due to the estimate of the fiber dispersion profiles. Therefore, generating Stokes wavelengths in the range of 2000 to 5000 nm requires anti-Stokes seed between 1269nm and 904nm. These anti-Stokes photons fall in the wavelength range that standard LDs exist, so commercially available LDs can be used as the seeding signal.

Zero Dispersion Wavelength (nm)	Theoretical Peak (nm) Stokes->Anti-Stokes	Experimental Peak (nm) Stokes->Anti-Stokes
1560	1370→1790	1400→1750
1570	1250→2050	1230→2110
1610	1120→2570	1170→2310
1700	1010→3360	1020→3250

Table 7.1 Theoretical and experimental peaks of Stokes and anti-Stokes waves.

Further investigation of the wavelength conversion into the mid-IR wavelength region could be conducted by testing ZBLAN fibers with different dispersion profiles, optical nonlinearities, and pump powers. Furthermore, the pump wavelength can be tuned within the telecom amplifier band to obtain certain targeted wavelength, and a seed LD can also be used at the Stokes wavelength to further facilitate the wavelength conversion process.

Spectrum distortion and absorption spectroscopy: For the absorption spectroscopy, any distortion of the output spectrum from the SC light source may affect the accuracy of the measurements. So it is very important to continue studying the impact of atmospheric absorption on the measured SC spectrum and the influence of water and blood absorption on the spectroscopic measurement of biological samples.

As illustrated in Fig. 7.6, the transmission window of atmosphere can be divided into several windows [5], where the air transparency reaches its peak level in the 3-4 μm regime. Optical light in the near- and mid-IR wavelength range is mostly affected by the presence of H_2O and CO_2, where water absorbs at ~1.4, ~1.8 and ~3 μm and carbon dioxide absorbs at ~2.2 and ~4.2 μm. So, if we want to construct any remote spectroscopic measurement system, the distortion of the SC spectrum exerted by the airborne molecules in the atmosphere should not be neglected. On the other hand, the SC laser can also be used to monitor the density

change of these airborne molecules. Although single- or multiple-wavelength based absorption measurement systems have been widely used for environment monitoring, SC laser still has its unique advantages for being able to monitor and measure multiple absorption lines or patterns of different chemical species simultaneously, which could considerably increase both the detection sensitivity and selectivity.

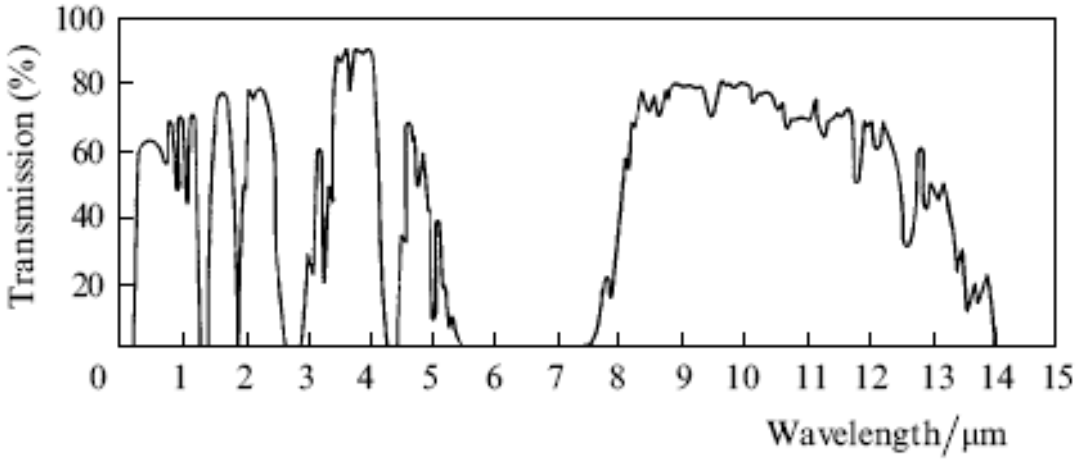

Fig. 7.6 Atmospheric transmission at sea level of a horizontal path length of 1882 m. This figure and its description are excerpted from Ref [5].

For experiments involving biological samples, the signal attenuation of water and blood absorption on the SC light source should also be considered. Water and blood have known absorption bands existing in the 2-4 μm wavelength regime. The optical signal will be attenuated and/or distorted through excitation of certain absorption bands. If the signal is heavily attenuated, the collected optical data may not have sufficient signal-to-noise ratio to reveal the spectral information of the biological sample. On the other hand, spectral absorption features of the water/blood may also interfere with that of the biological samples. As shown in Fig. 7.7, the absorption coefficient of water in the wavelength range of 3-4 μm is about ~200-400 cm^{-1} with a peak topping ~10000 cm^{-1} at 3 μm [6]. Therefore, the optical signal will be attenuated by at least a factor of ~10 after pass through a 100 μm thick water

layer, while completely dying out if the signal wavelength coincides with the absorption peak. In our experiments, we typically start to observe severe signal attenuation when the optical wavelength is longer than ~2-2.5 μm. However, we are still able to perform absorption spectroscopy measurement with a water layer thickness of ~50 μm.

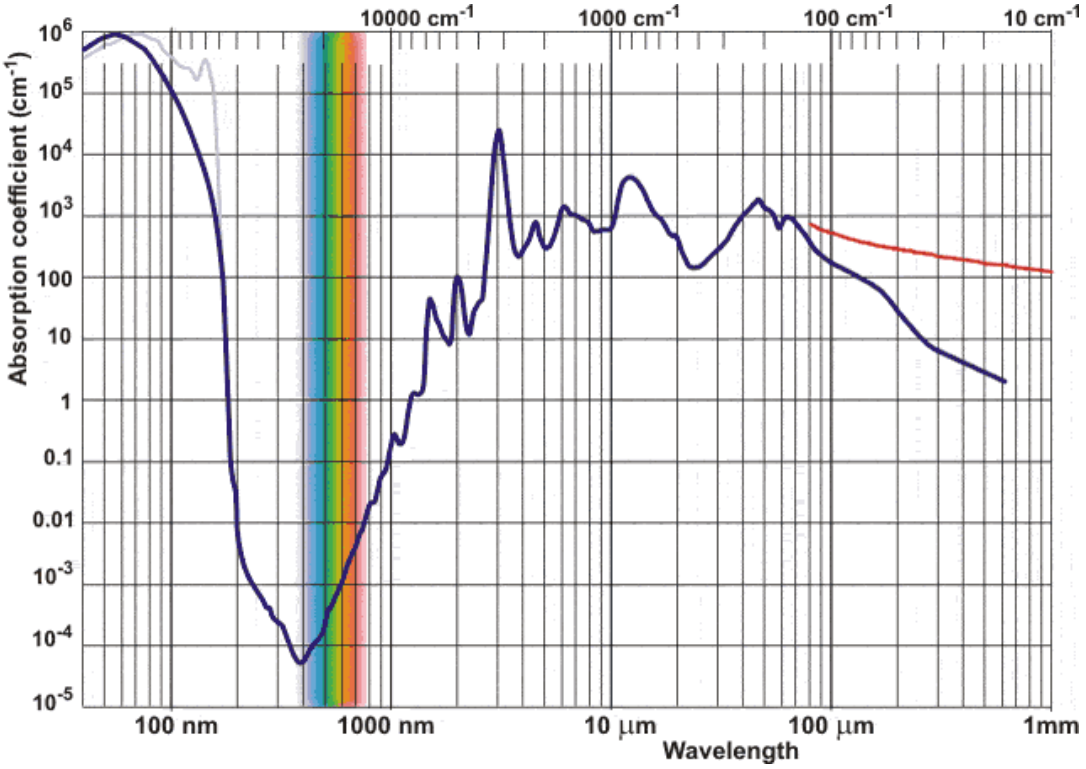

Fig. 7.7 Water absorption spectrum. This figure and its description are excerpted from Ref [6].

Figure 7.8 shows the absorption spectrum of egg yolk powder sample overlaid by a water layer of 50 μm path length. Although we cannot collect any meaningful signals at ~3 μm, which is the center of the water absorption peak, absorption features of egg yolk powder can still be identified in the 3.4-3.6 μm window. To apply the mid-IR spectroscopy measurement in the live biological body, the water or blood absorption issues need to be addressed. Various techniques have been developed to reduce the water absorption interference in the mid-IR. One method is to actively substitute low IR absorbing liquid for

water contents in the target of interest. Such technique has been adopted in OCT research to perform *in vivo* cross section tomography of biological samples. We can certainly leverage the advancement in that field to explore the potentials of *in vivo* mid-IR absorption spectroscopy using our SC laser.

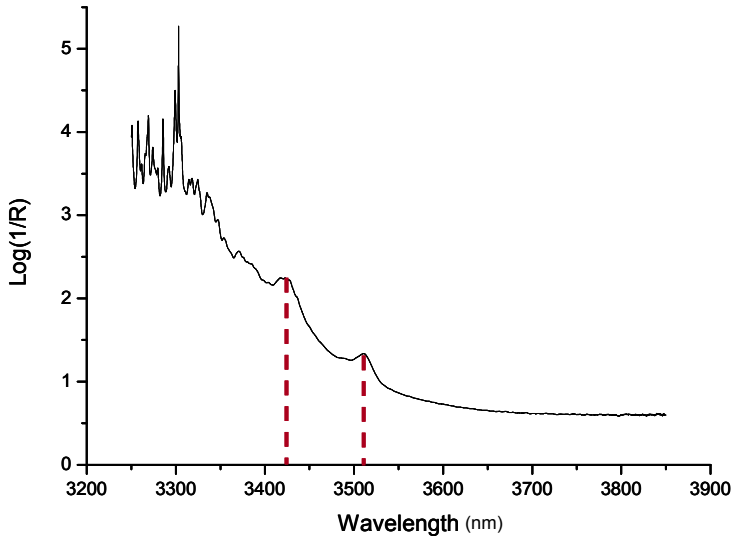

Fig. 7.8 Mid-IR absorption spectra of egg yolk powder overlaid with a 50 μm thick water layer.

Potential SC laser spectroscopy applications: Our SC laser source is a platform technology. Future work shall be devoted to explore various applications enabled by this unique laser, which is scalable in power to over 10 W and outputs single spatial mode over the entire spectrum.

One promising spectroscopy application of our SC laser is remote chemical sensing and explosive detection. As we mentioned earlier, many chemicals have their vibrational or rotational absorption signatures in this wavelength range. For example, many of the ingredients in gun powder, explosives and drugs have clear absorption lines in the mid-IR (Table 7.2). Although many of these ingredients have many lines in the long wavelength IR regime, i.e. ~8-15 μm, almost every chemical listed has at least one fingerprinting absorption

line in the 2-4 μm regime. So we hypothesize that our SC laser based absorption spectroscopy technique can be used for standoff detection and remote sensing of some of these chemicals

	Chemical Name	**Description**	**Mid-IR Absorption Lines (μm)**
Gun powder			
	Nitro-cellulose	chief ingredient	2.86, 3.45
	Diphenyl amine	Stabilizer	2.94, 3.33, 3.85
	Dibutyl phthalate	Plasticizer	3.4-3.55
	Lead azide	Primer	4.8
	Tetracene	Primer	2.8-4
	Barium nitrate	Primer	2.94, 4.2
	Strontium nitrate	Primer	2.94, 4.15
Explosives			
	Pentaerythritol tetranitrate	High explosive	2.67, 3.57, 4.25
	RDX (cyclotrimethylenetrinitramine)	Common explosive	2.6, 3.23, 3.4
	TNT	Common explosive	2.55, 3.23, 3.45
	Tetryl (2,4,6-trinitrophenymethylnitroamine)	Explosive	2.6, 3.23, 3.5
	HMX	Explosive	2.6, 3.3
	Ammonium nitrate	Widely used as oxidizer	3.23, 4.1
Drug detection			
	Cocaine	Common illicit drug	3, 3.4-4.1
	Methamphetamine	Common illicit drug	3.4, 4, 4.15
	MDMA (ecstasy)	Common illicit drug	3.4, 3.9, 4.2
	Heroin	Common illicit drug	2.9, 3.4, 4
Chemical warfare agents			
	Sarin (GB)	Nerve and blister agent	3.3, 3.4
	Cyclosarin (GF)	Nerve and blister agent	3.4, 3.5
	Soman (GD)	Nerve and blister agent	3.3, 3.6
	Tabun (GA)	Nerve and blister agent	3.4-3.6
	Sulfur mustard (HD)	Nerve and blister agent	3.3-3.4
	Nitrogen mustard (HN3)	Nerve and blister agent	3.3, 3.4, 4
	VX	Nerve and blister agent	3.4-3.6
	Lewisite (L)	Nerve and blister agent	3.1, 3.4

Table 7.2 Mid-IR spectral lines for different chemicals in weapons, drugs, or chemical warfare agents.

Particularly, preliminary experiments have been carried out to measure the absorption spectra of various components of gun powder. As shown in Table 7.3, we pick four representative functional components of the smokeless gun powder—i.e nitrocellulose as the

major explosion composition, dibutyl phthalate as the plasticizer, diphenylamine as the stabilizer, and nitroglycerin as the propellant, and compare their absorption spectra to that of gun powder mixture. The experimental setup of the absorption spectroscopy measurement is the same as discussed in the previous chapter.

Component	Function	Typical chemicals
Explosion Composition	Consists of the major ingredients of smokeless gun powder	Nitrocellulose
Plasticizer	Organic materials added to aid fabrication of propellants and explosive mixtures	Dibutyl Phthalate
Stabilizers	Organic materials that retard decomposition of other constituents during storage	Diphenylamine
Propellant	Organic materials that undergo rapid combustion	Nitroglycerin

Table 7.3 Smokeless gun powder composition.

The absorption spectra of different gun powder compositions are illustrated in Fig. 7.9. Two absorption features centered around 3.0 and 3.4 μm can be observed in the smokeless gun powder sample. We attribute these two features to the absorption signatures of nitrocellulose, which is further confirmed in Fig. 7.9b. It should be noted that the absorption peaks around 2.9 μm in Fig. 7.9b is attributed to the peripheral chemicals used in manufacturing nitrocellulose sample. This confirms our hypothesis that by measuring the absorption spectrum of smokeless gun powder mixture, we can identify at least one of its major components, i.e. nitrocellulose. Additional spectral signatures have also been observed in the 2-4 μm for the other gun powder components including dibutyl phthalate,

diphenylamine, and nitroglycerin. Therefore, SC light source and absorption spectroscopy measurement could be potentially used to remotely detect chemical species of interest.

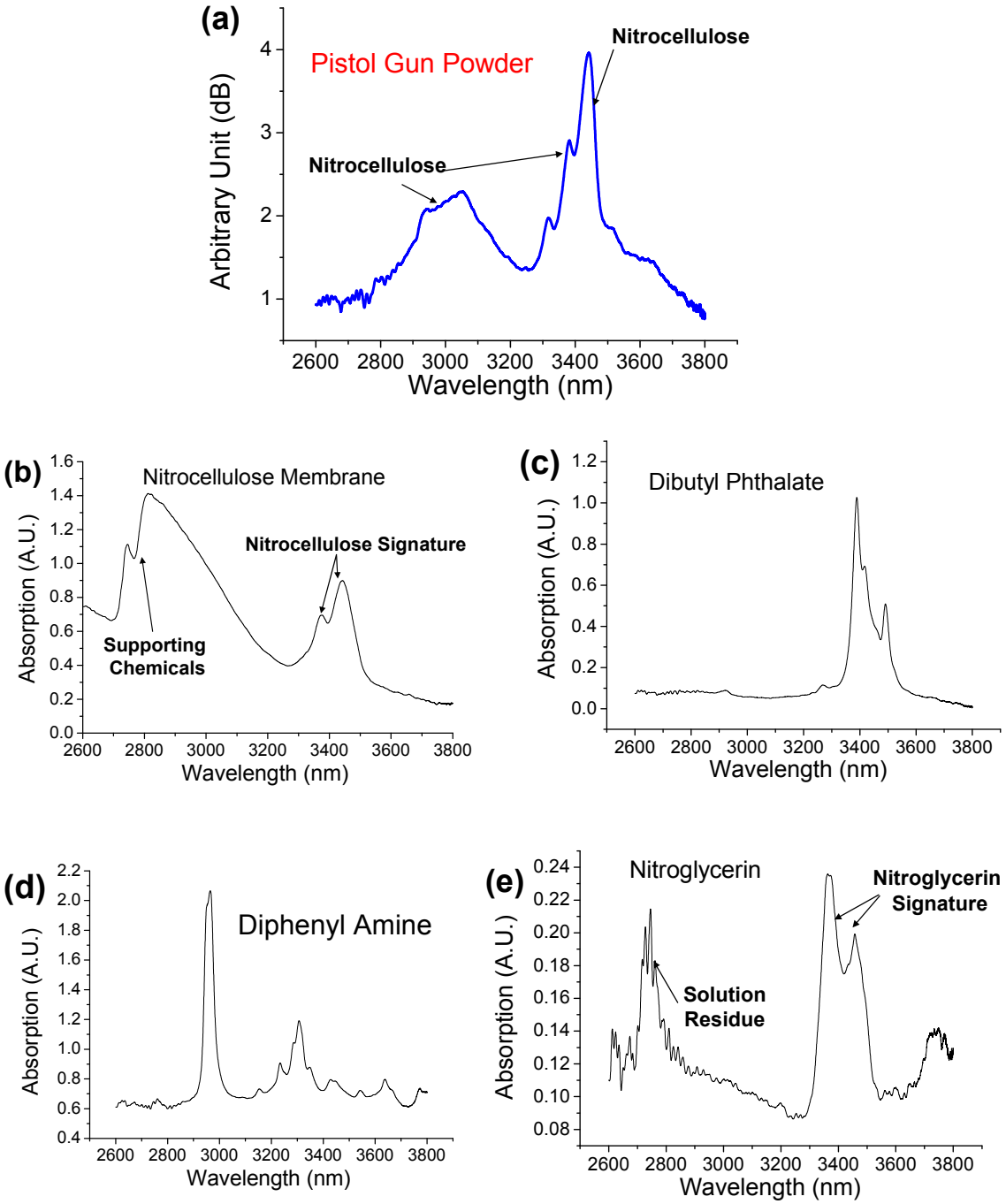

Fig. 7.9 Absorption spectra of various smokeless gun power compositions. (a) Smokeless gun powder, (b) nitrocellulose, (c) dibutyl phthalate, (d) diphenylamine, and (e) nitroglycerin.

To implement the SC laser based remote sensing system, several issues need to be further considered. First, experiments need to be conducted to determine the minimal detectable limits of various explosive compositions. For any given system detection limit and chemical absorption coefficient, it should be possible to calculate the minimal detectable level. Many explosive chemicals are in solid state format under room temperature, the corresponding saturated vapor pressure could be extremely low, down to sub-ppm or ppb level. Therefore, careful system design and parameter consideration need to be taken before any implementation of the actual field experimentation.

Furthermore, in the practical field environment, targeting the collimated SC light onto minute explosive trace might impose another limitation on the system efficacy. In certain scenarios, actual explosives are concealed in the well-sealed package, which makes direct contact between the SC light and targeted matter extremely challenging. In addition, because a mirror reflector, such as metal blocks on the road and building bricks, is required to re-direct the outgoing SC beam back onto the detector, which is typically located in the sample place as the SC laser, the collected signal may be severely distorted. So post-collection signal processing will be indispensible to extract the useful information.

Potential SC laser ablation applications: As for the biomedical experiments we demonstrated, the efficacy of the laser ablation can be further studied. Further studies can be conducted to find the optimal laser operation conditions for different applications, such as pulse width, energy per pulse, and wavelength band, for both spectroscopic detection and selective ablation.

As a potential candidate for the treatment of atherosclerotic vulnerable plaque (VP), the efficacy of the selective ablation approach needs to be further studied. Lasers, such as

excimer lasers, have been used in angioplasty to break apart thrombus that has already occluded the blood vessel (e.g., see [7-9]). The open questions include whether VP can be distinguished from stable plaque and if laser ablation will cause any significant adverse responses, e.g. inflammation or thrombosis caused by the VP rupture due to the weakening of the fibrous cap [10]. Further studies must also be conducted to find the optimal laser operation conditions, such as pulse width, energy per pulse, and wavelength band, for both spectroscopic detection and selective ablation.

The lipid absorption based selective ablation technique also opens up new windows for other potential applications, such as laser liposuction, subcutaneous fat and sebaceous gland treatments [11]. Preliminary ablation experiments on fat tissue have shown that fats become fluidic upon ablation and remain so with no visible solidification at room temperature. Such fats might be then absorbed or removed by appropriate methods, e.g. using a suction canula. On the other hand, egg yolk ablation experiments have shown reduction in overall volume with no visible debris surrounding the ablated hole. We intend to further investigate whether the debris resulting from ablative therapy might be absorbed by the body after wounds healed, as is in the case of other laser-based surgeries such as corneal reshaping and percutaneous laser disc decompression.

To conclude, our SC light source opens up new venues for a lot of potential applications. With thorough analysis and deep understanding of both the physics of the SC light source and related field of the intended experiments, I believe the mid-IR SC light source could be a vital part of many disruptive applications.

References

[1] J. A. Harrington, “Infrared Fibers,” in *Handbook of Optics Vol. 3, Classical, Vision & X-ray Optics*, M. Bass, J. M. Enoch, E. W. Van Striland, and W. L. Wolfe, eds.(Optical Society of America, Washington DC, 2002), pp. 14.1 - 14.16.

[2] P. Domachuk, N. A. Wolchover, M. Cronin-Golomb, A. Wang, A. K. George, C. M. B. Cordeiro, J. C. Knight, and F. G. Omenetto, “Over 4000 nm bandwidth of mid-IR supercontinuum generation in sub-centimeter segments of highly nonlinear tellurite PCFs,” Opt. Express **16**, 7161-7168 (2008).

[3] O. P. Kulkarni, C. Xia, D. J. Lee, M. Kumar, A. Kuditcher, M. N. Islam, F. L. Terry, M. J. Freeman, B. G. Aitken, S. C. Currie, J. E. McCarthy, M. L. Powley, and D. A. Nolan, “Third order cascaded Raman wavelength shifting in chalcogenide fibers and determination of Raman gain coefficient,” Opt. Express **14**, 7924-7930 (2006).

[4] J. S. Sanghera, L. B. Shaw, C. M. Florea, P. Pureza, V. Q. Nguyen, D. Gibson, F. Kung, and I. D. Aggarwal, “Non-linearity in chalcogenide glasses and fibers, and their applications,” presented at Quantum Electronics and Laser Science Conference QELS 2008, San Jose, Calif., May 4-9, 2008, QTuL5.

[5] B. I. Vasil'ev and O. M. Mannoun, “IR differential-absorption lidars for ecological monitoring of the environment,” Quantum Electron. **36**, 801-820 (2006).

[6] “Water absorption spectrum,” http://www.lsbu.ac.uk/water/vibrat.html.

[7] J. B. Dahm, O. Topaz, C. Woenckhaus, A. Staudt, B. Mox, A. Hummel, and S. B. Felix, "Laser-facilitated thrombectomy: A new therapeutic option for treatment of thrombus-laden coronary lesions," Catheter. Cardiovasc. Interv. **56**, 365-372 (2002).

[8] M. Dorr, D. Vogelgesang, A. Hummel, A. Staudt, D. M. Robinson, S. B. Felix, and J. B. Dahm, "Excimer laser thrombus elimination for prevention of distal embolization and no-reflow in patients with acute ST elevation myocardial infafction. Results from the randomized LaserAMI study," Int. J. Cardiol. **116**, 20-26 (2007).

[9] V. Ambrosini, A. Cioppa, L. Salemme, T. Tesorio, G. Sorropago, G. Popusoi, E. Stabile, A. Medolla, F. Cangella, M. Agrusta, E. Picano, and P. Rubino, "Excimer laser in acute myocardial infarction: Single centre experience on 66 patients," Int. J. Cardiol. **127**, 98-102 (2008).

[10] P. Libby, "Atherosclerosis: The new view," Sci. Am. **286**, 47-55 (2002).

[11] R. R. Anderson, W. Farinelli, H. Laubach, D. Manstein, A. N. Yaroslavsky, J. Gubeli, K. Jordan, G. R. Neil, M. Shinn, W. Chandler, G. P. Williams, S. V. Benson, D. R. Douglas, H. F. Dylla, “Selective photothermolysis of lipid-rich tissues: A free electron laser study,” Lasers Surg. Med. **38**, 913-919 (2006).